INAUGURAL – Dissertation

zur Erlangung der Doktorwürde
der Naturwissenschaftlich-Mathematischen Gesamtfakultät
der Ruprecht-Karls-Universität Heidelberg

Vorgelegt von
M.Sc. Sofia Antonova
aus Nowokusnezk, Russland

Tag der mündlichen Prüfung: 25.01.2017

Exploring the potential of high temporal resolution X-band SAR time series for various permafrost applications with ground truth observations in the Lena River Delta, Siberia

Gutachter:

PD Dr. Julia Boike

Prof. Dr. Andreas Kääb

Zusammenfassung

Permafrost, definiert als mehrjährig gefrorener Untergrund, ist mit Fernerkundungsmethoden nicht direkt beobachtbar. Aktuell wird eine Vielzahl von indirekten Messmethoden entwickelt und getestet, welche den Zustand von Permafrost anhand spezifischer Prozesse und Umweltparameter erfassen. Die Ergebnisse dieser Studien dienen der Entwicklung von zukünftigen Satellitenmissionen, die das großräumige Monitoring von Permafrost zum Ziel haben. Die vorliegende Doktorarbeit untersucht in diesem Zusammenhang das Potenzial von TerraSAR-X (TSX) Zeitreihen zur Erfassung und Auswertung von Permafrost relevanten Prozessen der Landoberfläche. Zum ersten Mal wurde eine mehrjährige SAR (Synthetic Aperture Radar)-Zeitreihe mit hoher zeitlicher (11 Tage) und räumlicher (3 m) Auflösung in einem kontinuierlichem Permafrostgebiet in Sibirien ausgewertet. Umfassende Messdaten der Landoberfläche wurden während drei Sommer- und Winterexpeditionen zur Validierung und Interpretation der TSX-Daten gesammelt. Die Doktorarbeit gliedert sich in drei Fallstudien: (i) die Detektion von Veränderungen der Landoberfläche (Frieren und Tauen des Bodens, Änderungen der Oberflächenfeuchte, Schneebeginn und Schneeschmelze), (ii) das Monitoring von Tiefe und Phänologie von Eis auf Seen (Zeitpunkt der Bildung und des Aufbruchs des Eises) und (iii) die Nutzung differentieller SAR-Interferometrie (DInSAR) zur Erfassung der Absenkung der Permafrostoberfläche (Subsidenz). Für die ersten zwei Fallstudien wurden aus den TSX-Daten die Intensität der Rückstreuung sowie die interferometrische Kohärenz (ein Maß der Phasenstabilität zwischen zwei aufeinanderfolgenden Aufnahmen) berechnet und ausgewertet. Änderungen in der Rückstreuung waren nur messbar bei Regen, Schneefall oder Entstehen einer Schneekruste durch Schmelz- und Gefrierwechsel während des Aufnahmezeitpunkts des Radarbildes. Die interferometrische Kohärenz nahm zu Beginn der Schneebedeckung sowie zum Beginn der Schneeschmelze stark ab und

bietet damit eine Möglichkeit zur Erfassung dieser Ereignisse. In der zweiten Fallstudie erwies sich die Rückstreuung als exzellentes Maß für die Unterscheidung, ob die Eisdecke eines Sees bis zum Grund durchgefroren ist oder sich noch Wasser unter der Eisdecke befindet. Außerdem kann durch die hohe zeitliche Auflösung der TSX-Daten der Zeitpunkt des Durchfrierens von Seen genauer als bisher bestimmt werden. Auch die Eisphänologie konnte mit Hilfe der Rückstreuung gut nachvollzogen werden. Die interferometrische Kohärenz erfasste den Zeitpunkt des Durchfrierens flacher Seen sowie den Beginn der Eisschmelze auf diesen Seen. Die Untersuchung der Kohärenz war eine hilfreiche Vorbereitung für die DInSAR-Analysen der dritten Fallstudie. Für den Zeitraum von zwei Jahren, in denen TSX-Daten zur Verfügung standen, konnten kohärente Interferogramme mit 11- oder 22-tägigen Intervall nur für einen Sommer verwendet werden. Im Vergleich zu Feldmessungen zeigen die DInSAR-Berechnungen eine zu geringe Subsidenz. Feldmessungen zeigen eine hohe kleinräumige Heterogenität der Subsidenz. Dies führt vermutlich zu Fehlern in der Phasenintegration (phase unwrapping), die eine falsche Subsidenz ergibt. In dieser Hinsicht ist die konventionelle DInSAR-Prozessierung nicht geeignet, um das Tauen des Permafrostes und die daraus resultierende Subsidenz zu erfassen. Die Ergebnisse der DInSAR-Studie verdeutlichen, wie wichtig Feldmessungen für die Validierung von DInSAR-Subsidenzanalysen sind. Insgesamt zeigt die Doktorarbeit das Potenzial und die Grenzen der Nutzung von TSX-Daten zur räumlichen und zeitlichen Beobachtung des Permafrosts. Sie leistet einen wesentlichen Beitrag zur methodischen Entwicklung von systematischen Langzeitüberwachungen des Permafrosts.

Abstract

Permafrost is a subsurface phenomenon that cannot be directly monitored with satellite remote sensing. A variety of indirect approaches are currently being developed which aim to measure permafrost-related processes and environmental variables. Results of these studies aid the planning of future satellite missions which will allow large-scale permafrost monitoring. This thesis contributes to this ongoing effort by assessing the potential of repeat-pass TerraSAR-X (TSX) time series for permafrost-related applications. For the first time, multi-year Synthetic Aperture Radar (SAR) data with high temporal (11 days) and spatial (3 m) resolution was analysed for a region characterized by continuous permafrost in the Siberian Arctic. Extensive in situ data was collected during three summer and winter expeditions to validate and interpret remote sensing results. Three case studies were carried out: (i) the detection of land surface changes (e.g. ground freezing and thawing, surface wetness variations, snow cover onset and melt); (ii) monitoring bedfast lake ice and ice phenology (freeze-up, melt onset, break-up); and (iii) differential SAR interferometry (DInSAR) for thaw subsidence monitoring. For the first two case studies, time series of both backscatter intensity and 11-day interferometric coherence (i.e. a measure of phase stability between two SAR images) were investigated. Backscatter intensity was generally shown to be insensitive to the land surface changes but responded to events that occurred at the time of TSX acquisition (rain, snow shower, melt/freeze crust on snow). Interferometric coherence decreased dramatically across the entire image upon snow cover onset and melt, permitting the possible use of coherence for the monitoring of these events. Backscatter intensity was found to be an excellent tool for the detection and monitoring of bedfast lake ice due in part to improved temporal resolution compared to previously used SAR systems. Ice phenology was mostly well tracked with backscatter intensity. Interferometric coherence was found to be sensitive to the lake ice grounding and to

the onset of surface melt on the lakes with bedfast ice. The investigation of coherence was a useful preparative step for the following DInSAR analysis. For the third case study, coherent 11-day and 22-day interferograms were available only for one summer of the two-year TSX time series. The cumulative DInSAR displacement strongly underestimated the subsidence observed on the ground. In situ observations revealed high variability of subsidence, which likely caused errors in phase unwrapping. Conventional DInSAR processing might therefore not be suitable for the accurate representation of permafrost thaw subsidence. This study highlights the importance of field measurements for the quantification of thaw subsidence with DInSAR, which were mostly omitted in the previous studies. All in all, this thesis shows the limitations and potential of TSX time series to spatially and temporally monitor permafrost. It thus provides an important contribution to the methodological development of a long-term permafrost monitoring scheme.

Publications

This cumulative thesis is composed of the following publications.

Spatio-temporal variability of X-band radar backscatter and coherence over the Lena River Delta, Siberia.

Authors: Antonova, S., Kääb, A., Heim, B., Langer, M., and Boike, J.

Status of publication: published

Journal: Remote Sensing of Environment, 2016, 182, 169-191, doi: 10.1016/j.rse.2016.05.003.

Author's contributions: The author designed the study with support from the co-authors. The author reviewed the relevant literature, analysed the data, produced the figures, and wrote the manuscript. The co-authors reviewed and discussed the manuscript.

Julia Boike Moritz Langer

Monitoring Bedfast Ice and Ice Phenology in Lakes of the Lena River Delta Using TerraSAR-X Backscatter and Coherence Time Series.

Authors: Antonova, S., Duguay, C. R., Kääb, A., Heim, B., Langer, M., Westermann, S., and Boike, J.

Status of publication: published

Journal: Remote Sensing, 2016, 8(11), 903, doi: 10.3390/rs8110903.

Author's contributions: The author designed the study with support from the co-authors. The author reviewed the relevant literature, analysed the data, produced the figures, and wrote the manuscript. The co-authors reviewed and discussed the manuscript.

Julia Boike Birgit Heim

Permafrost thaw subsidence in the Lena River Delta, Siberia, measured in situ and estimated from TerraSAR-X interferometry.

Authors: Antonova, S., Sudhaus, H., Kääb, A., Heim, B., Langer, M., Strozzi, T., and Boike, J.

Status of publication: draft.

Author's contributions: The author designed the study with support from the co-authors. The data was analysed and interpreted by the author with the support from H. Sudhaus, A. Kääb and T. Strozzi. The author partly conducted the field measurements, reviewed the relevant literature, produced the figures, and wrote the manuscript. The co-authors reviewed and discussed the manuscript.

Birgit Heim Moritz Langer

Contents

List of Tables

List of Figures

Selected Acronyms

ACIA Arctic Climate Impact Assessment
CLIMo Canadian Lake Ice Model
DEM Digital Elevation Model
DGPS Differential Global Positioning System
DInSAR Differential SAR Interferometry
GPS Global Positioning System
HH, HV, VH, VV – polarization modes: H- horizontal, V – vertical
InSAR SAR Interferometry
IPCC Intergovernmental Panel on Climate Change
LOS Line-of-Sight
NDVI Normalized Difference Vegetation Index
NOAA National Oceanic and Atmospheric Administration
PC Principal Component
PCA Principal Component Analysis
ROI Region of Interest
SAR Synthetic Aperture Radar
SLC Single Look Complex
TDD Thawing Degree Days
TSX TerraSAR-X
UTC Coordinated Universal Time
UTM Universal Transverse Mercator
WGS84 World Geodetic System 1984
WMO World Meteorological Organization

Thesis organization

This thesis consists of four chapters. The Background and Outline provides an introduction to the state-of-the-art of remote sensing for permafrost and its current challenges, sets the research goals of the thesis, and describes the study area. It further summarizes the most important results of the study and closes with conclusions and an outlook for the future. The three main chapters consist of original research papers that have been published or prepared for publication in international peer-reviewed journals. Chapter 2 explores the opportunities of monitoring environmental surface changes with time series of TSX backscatter intensity and interferometric coherence. Chapter 3 investigates the prospects of monitoring bedfast ice and ice phenology on shallow thermokarst lakes with time series of TSX backscatter intensity and interferometric coherence. Chapter 4 tests the viability of TSX data for interferometric analysis of vertical thaw displacements of the ground surface.

1

Background and Outline

1.1 Introduction

1.1.1 Importance of permafrost

According to the International Permafrost Association, permafrost is a soil or rock that remains at or below zero degrees Celsius (°C) for at least 2 consecutive years. Permafrost occurs in polar regions as well as in the mid-latitude mountain regions. Usually, permafrost areas are divided into several zones depending on the occurrence and continuity of permafrost: continuous permafrost (underlying 90-100% of the area); discontinuous permafrost (50-90%), sporadic permafrost (10-50%) and isolated patches (< 10%) (Brown et al., 1998) (Fig.1). Approximately 24% of the Northern Hemisphere is occupied by these permafrost zones, while only half of these zones is characterized by continuous permafrost (Zhang et al., 1999).

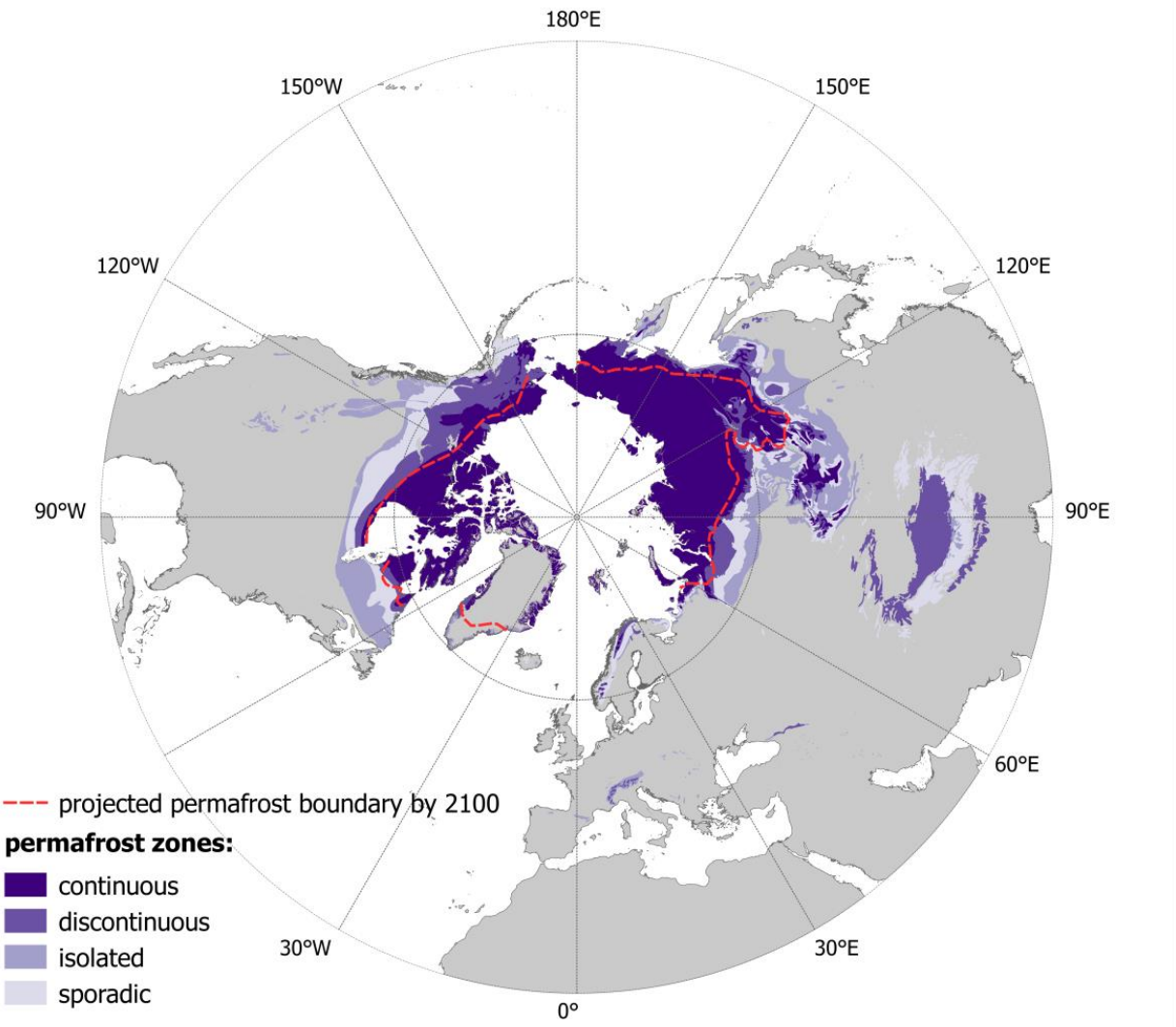

Figure 1. Permafrost zones in the Northern Hemisphere (Brown et al., 1998) and projected southern boundary of permafrost in the year 2100 (ACIA report, 2005).

The thickness of permafrost can reach hundreds of meters. For example, in 1965, frozen ground was observed up to a depth of approximately 1500 m in Yakutia, Russia (Melnikov, 1967). Such thick permafrost developed during the last glacial period when most of Northeast Siberia was unglaciated and exposed to cold surface temperatures. During that time, remnants of plants and animals simultaneously accumulated in the ground with the development of permafrost. Therefore, large quantities of carbon are preserved in the ground, an amount that is likely twice as large as the current quantity of carbon in the atmosphere (Zimov et al., 2006). A recent estimate quantifies the pool of terrestrial permafrost carbon in the Northern

Hemisphere to be 1330-1580 gigatons (Gt) (Schuur et al., 2015). Present-day global climate warming is more intense in high latitudes due to Arctic amplification. Mean surface air temperatures from > 60 °N over the land have increased by 1.36 °C, which is almost two times stronger than the average warming in the Northern Hemisphere from 1875 to 2008 (Bekryaev et al., 2010; IPCC report, 2013). The year 2015 broke all the previous records and was the warmest year since 1880. Global land surface temperatures in 2015 were 1.33 °C higher than the 20th century average (NOAA, 2016).

Increased surface temperatures cause permafrost to warm and thaw. In Russia, for instance, permafrost borehole temperatures, measured at the depth of zero annual amplitude have increased by 0.5 to 2.0 °C since 1970s (Romanovsky et al., 2010). Some studies project the global northward retreat of the continuous permafrost zone and the complete disappearance of the current discontinuous permafrost zone by the next century (ACIA report, 2005) (Fig. 1). Permafrost thaw exposes the previously trapped organic carbon to aerobic decomposition and leads to its emission into the atmosphere in the form of carbon dioxide and methane. Due to the greenhouse effect, the excessive presence of these gases in the atmosphere could potentially amplify global warming. As a result, permafrost was identified as an Essential Climate Variable in the Global Climate Observing System by the World Meteorological Organization (WMO, 2010).

Much effort is put into modeling, which aims to predict how much and how fast the permafrost carbon pool can be released into the atmosphere over the next one hundred years. Large uncertainties in the model projections are related to a poor quantification of the carbon stored in vast and remote Arctic territories, especially at depths greater than one meter. Another reason is the complexity of processes that govern permafrost thaw, as well as biogeochemical processes that control the decomposition of carbon. For example, abrupt permafrost thaw, which occurs due to the melting of ground ice and causes the land surface to collapse, is not included in large scale models, although this process typically results in rapid and significant carbon loss (Schuur et al., 2015).

Besides carbon loss, abrupt permafrost thaw also results in ground settlement, slope failures, and thaw slumps, all of which can damage infrastructure, as well as affect

hydrology, vegetation and energy fluxes of ecosystems (e.g. Nelson et al., 2001; Kääb, 2008; Osterkamp et al., 2009; Jorgenson et al., 2013).
These severe consequences make it particularly important to better understand the current state of permafrost and predict its future dynamics under a changing climate.

1.1.2 Remote sensing for permafrost investigations: state of the art

In situ observations in vast Arctic areas are often restricted to point measurements in accessible areas, but do not represent the strong spatial variability of the processes and landscapes features in permafrost regions. Satellite remote sensing is a viable alternative as it provides both systematic observations and extensive spatial coverage. Remote sensing of many components of the cryosphere, such as glaciers, sea ice and snow cover, is well developed and supplies crucial monitoring information (e.g. Raup et al., 2015; Meier & Markus, 2015; Hall et al., 2015). On the contrary, remote sensing of permafrost is still not well developed. A major challenge is the fact that permafrost is a sub-surface thermal condition rather than a visible ground surface substance. Yet, numerous remote sensing applications were developed recently for indirect investigations of permafrost (National Research Council, 2014; Bartsch, 2014; Westermann et al., 2015a).
Some permafrost properties, such as the active layer thickness, ground ice content, and the presence of taliks are crucial for the permafrost monitoring and can be indirectly retrieved with the help of remote sensing. A talik is a year-round unfrozen zone within permafrost, which often occurs beneath lakes which do not freeze all the way to the bottom in winter. Methods for the retrieval of these properties generally include the use of land cover products, which aid to extrapolate field data (e.g. Nelson et al., 1997; Gangodagamage et al., 2014) and the use of remote sensing products, such as land surface temperature and snow water equivalent for modeling (e.g. Langer et al., 2013; Westermann et al., 2015b). Another new and actively evolving method is the use of the radar interferometry to measure thaw subsidence and consequently estimate near-surface ground ice content or active layer thickness (e.g. Liu et al., 2012). Estimation of taliks distribution can be made based on the

identification of lakes that do not freeze to the bed in winter (e.g. Jeffries et al., 1999).

Other than investigating permafrost properties, remote sensing methods can be used for studying land surface transformations that occur due to permafrost degradation. Among these land transformations are the formation, expansion, and drainage of thermokarst lakes (e.g. Riordan et al., 2006; Arp et al., 2011), thaw slumps (e.g. Lantuit & Pollard, 2005; Fraser et al., 2014) and coastal erosion (e.g. Lantuit & Pollard, 2008; Günther et al., 2013).

Another approach is monitoring environmental variables, such as the freeze/thaw state of the ground, moisture of the upper soil layer, vegetation, and snow cover, which largely define the thermal state of permafrost. Also, these variables are often used as an input for permafrost thermal models. Optical sensors, as well as active and passive microwave sensors are used to monitor these variables (e.g. Naeimi et al., 2012; Muskett et al., 2015; Nitze and Grosse, 2016; Pivot et al., 2012).

Although the described methods and approaches demonstrate progress towards remote permafrost monitoring, there are still limitations. Major challenges include the lack of ground truth validation, as well as insufficient spatial and temporal coverage and resolution of satellite data and products. That is why it is extremely important to assess all the potential use and drawbacks of current satellite observational systems, especially for the design and planning of future missions.

Active microwave remote sensing is advantageous in polar areas because of its ability to penetrate through clouds, which are often present there, and independency from daylight. New generation X-band radar satellite TerraSAR-X (TSX), launched by the German Aerospace Center, started its service in 2008 and continues to run today. It provides SAR data with excellent radiometric and geometric accuracy. Outstanding spatial resolution (up to 1 m) makes TSX data immensely useful for detailed ground surface observations. A revisit cycle of 11 days is also an improvement compared to previous Earth observation SAR systems (e.g. ERS-1/2 and ENVISAT ASAR with 35 days, RADARSAT-1/2 with 24 days and ALOS-PALSAR with 46 days). Previous studies partly assess the potential of TSX data for permafrost investigations. For instance, Sobiech (2012) monitors environmental variables (ground freezing, snow melt, lake and river ice decay) in Siberia with TSX data, which covered one summer

season. Short et al. (2011) and Beck et al. (2015) test the viability of TSX data for the interferometry analysis in the Canadian Arctic. Regmi et al. (2012) use TSX data for one summer season to characterize drained thermokarst lake basins in Alaska. Jones et al. (2013) use a single TSX image to detect bedfast ice on the lakes in Alaska. Ullmann et al. (2014) implement polarimetric analyses of TSX data for classifying tundra environments in the Canadian Arctic. Duguay et al. (2015) assess the potential of polarimetric TSX data for shrub monitoring in the Canadian subarctic. These studies mainly use single TSX images or time series, limited to one season. Evaluation of multiyear time series of repeat-pass TSX data in permafrost landscapes had been lacking prior to this thesis.

1.1.3 Research goals

This thesis aims to estimate the potential of a unique time series of SAR data for a variety of permafrost-related applications. The time series consists of a three-year long set of TSX imagery (X-band) with high temporal (11 day) and spatial (~3 m) resolution. Field data was extensively used to interpret and validate the remote sensing results.

Three different case studies were conducted to assess the potential of TSX data for permafrost applications:

- Detection of environmental land surface changes, relevant for permafrost areas, such as ground freezing/thawing, wetness variations, snow cover onset, and snowmelt (Chapter 2).
- Monitoring lake ice regimes (bedfast or floating) and ice phenology (Chapter 3).
- Detection of thaw subsidence with SAR interferometry (Chapter 4).

1.1.4 Technical background on SAR

Unlike optical imagery, the use of **microwave** imagery is favorable in polar areas as it is not affected by the often persistent cloud cover and polar night. Compared to optical remote sensing, however, interpretation of microwave remote sensing data is less straightforward. Microwave instruments are divided into **passive** and **active** sensors. Passive sensors detect natural microwave emissions of objects on Earth and

provide low spatial resolution, whereas active sensors (or **radars**) transmit pulses of energy to the objects and receive an echo of these pulses via an antenna. The spatial resolution of radar imagery depends on the size of the antenna. **Synthetic Aperture Radar (SAR)** uses the motion of the antenna during the time when the pulse returns back in order to "enlarge" the antenna artificially. Radar systems operate in a variety of frequency bands from 0.3 GHz to 300 GHz, corresponding to wavelengths from 1 m to 1 mm, which define the penetration depth of the signal as well as the size of the target which can be detected. The portion of transmitted energy that is received by the antenna is called **backscatter**. The data obtained by radar are complex and represented by the **amplitude** and **phase** of the returned signal. The amplitude (after calibration) provides a conventional grey-scale image and characterizes the intensity of the backscatter. This intensity is mainly defined by two properties of the scattering object: the surface roughness and the dielectric constant. As the surface roughness relative to the sensor's wavelength increases, the backscatter intensity increases due to a diffused scattering (Fig. 2a). In case of a smooth surface relative to the wavelength of the sensor, the signal is specularly reflected away from the antenna, resulting in low backscatter intensity (e.g. calm water or asphalt) (Fig. 2b). Imagine two surfaces that form a right corner facing the radar beam. In this case, the signal is reflected twice and most of the transmitted energy returns back to antenna, resulting in very high backscatter intensity (e.g. man-made constructions and corner reflectors) (Fig. 2c). In the case of inhomogeneous media characterized by randomly distributed discrete elements in a volume (e.g. snow, ice, or vegetation), the signal can scatter from and between these elements, thus creating a complex interaction (Fig. 2d). Depending on the size of the scattering elements compared to the wavelength, signal attenuation or amplification prevails, resulting in lower or higher backscatter intensity, respectively.

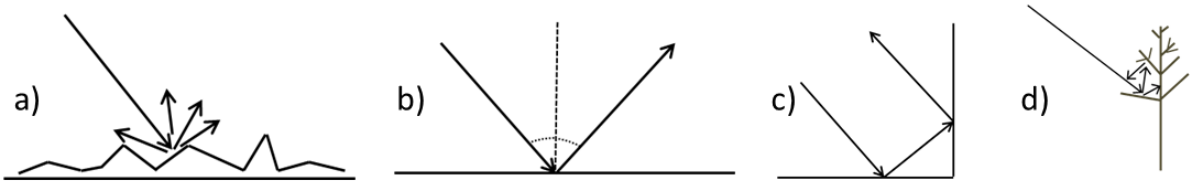

Figure 2. a) Diffused scattering of the signal from a rough surface results in high backscatter intensity; b) specular reflection of the signal from a smooth surface results in low backscatter

intensity; c) double-bounce reflection results in very high backscatter intensity; d) volume scattering in a tree. Figures are adapted from ASAR product handbook (Copyright 2000-2007, European Space Agency).

The dielectric constant of the scattering object can significantly increase with water content, resulting in shallower signal penetration depth, higher reflectivity, and, consequently, higher backscatter intensity. However, the latter is not the case for the standing water. Based on this effect, it is possible to detect wetness variations of the ground, as well as ground freezing and thawing.

One of the distinctive properties of a radar signal is its capability to penetrate through fresh ice. In the case of **floating** lake ice, which has liquid water underneath, backscattering occurs from the ice-water interface due to the high dielectric contrast between ice and water. The backscatter intensity is high due to a rough ice bottom (e.g. Atwood et al., 2015). In the case of **bedfast** ice, which is ice grounded to the lake bottom, the radar signal penetrates through the ice layer. The signal partially transmits through the frozen lake bottom due to the low dielectric contrast between ice and frozen sediments, which results in low backscatter (Fig. 3). Thus, it is possible to detect and monitor bedfast lake ice based on the prominent decrease of backscatter during the winter season.

Lake **ice phenology** (i.e. freeze up, melt onset, and water clear of ice) can be monitored using variations in backscatter intensity caused by changes in backscattering properties of ice during different growth stages. Thin, newly formed ice is characterized by low backscatter intensity due to specular reflection of the signal (e.g. Surdu et al., 2015). Ice thickening results in an increase of backscatter intensity up to a saturation point after which the backscatter remains stable during the rest of the winter in case of the floating ice (e.g. Jeffries et al., 1994). The onset of surface melt corresponds to changes (increase or decrease) of backscatter intensity from its stable winter condition (e.g. Jeffries et al., 1994). Water clear of ice can be identified by low backscatter caused by specular reflection from the open water, but only in the case of calm water. Under windy conditions, backscatter increases and open water cannot be easily identified (e.g. Surdu et al., 2015).

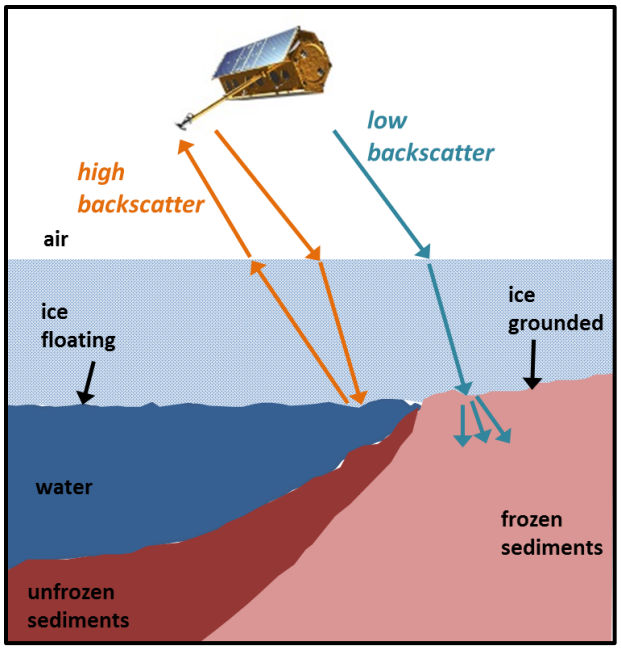

Figure 3. Principle of radar backscattering for different ice regimes (floating and grounded) at a typical lake in a permafrost landscape.

In contrast to SAR backscatter intensity analysis, **SAR interferometry (InSAR)** uses the phase component of the microwave signal. This method is used to produce Digital Elevation Models (DEMs) or to detect surface displacements. It is based on measuring a phase difference between two SAR datasets which are taken simultaneously by two sensors from different positions (for DEM generation) or at different times from exactly the same positions (for displacement detection) (Fig. 4).

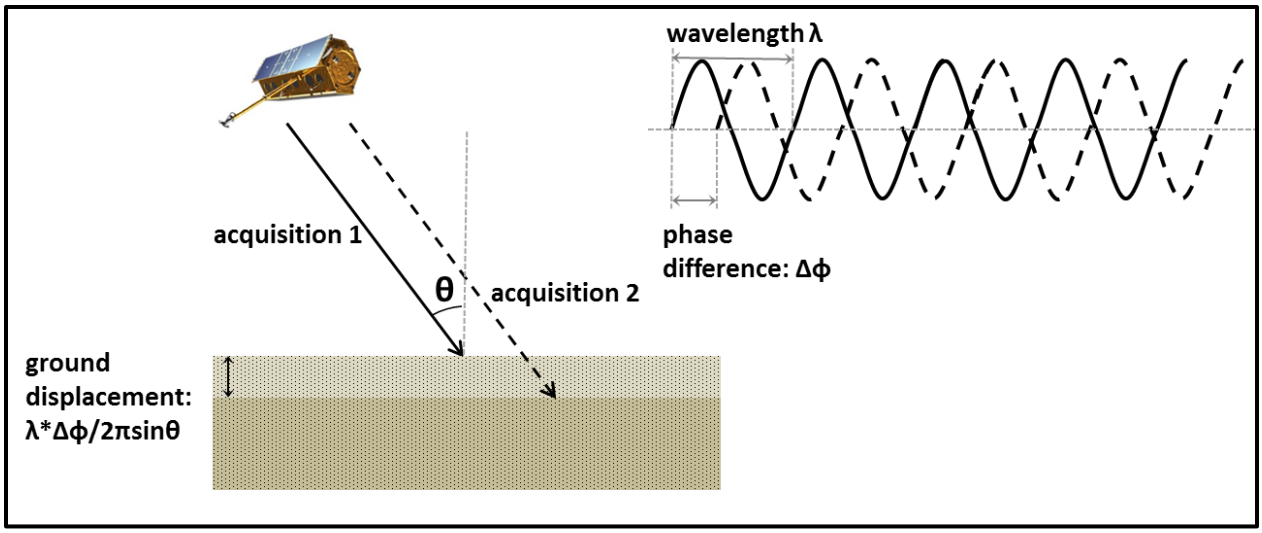

Figure 4. Principle of InSAR: two SAR acquisitions are taken over the same area at different times and the phase difference is converted to the physical displacement of the object.

InSAR has been successfully applied for detecting ground movements associated with earthquakes and volcanic eruptions (e.g. Massonnet et al., 1993). Ground subsidence, which occurs in permafrost landscapes due to the melting of ground ice, can potentially be monitored with InSAR as well. Recently, the method has been tested by a number of studies (e.g. Rykhus & Lu, 2008; Liu et al., 2010; Short et al., 2011; Strozzi et al., 2012; Liu et al., 2014; Short et al., 2014; Liu et al., 2015; Beck et al., 2015). One of the main limitations for InSAR is the insufficient **phase coherence** between SAR images due to land surface changes that occur between SAR acquisitions (Zebker and Villasenor, 1992). The coherence varies between 0 (completely decorrelated signals) and 1 (perfectly correlated signals). Low coherence restricts the use of InSAR. However, the low coherence can be used in this case as a direct geophysical signal for the detection of such land surface changes (e.g. Rignot & van Zyl, 1993; Wegmüller & Werner, 1997). Examples of land surface changes, resulting in coherence loss, are snow cover onset and snow melt (i.e. when the nature of backscattering elements is completely changed). The wavelength of a SAR system impacts the coherence. Longer waves (such as L-band) penetrate through vegetation, resulting in the main backscatter originating from the underlying soil, whereas shorter waves (such as X-band) scatter mainly from leaves and branches and therefore are much more vulnerable to the motion of these elements. The underlying soil is more stable over time than the vegetation above; therefore, the coherence of longer waves can be much higher than that of shorter waves over the same time period.

1.2 Study area

The Lena River Delta is situated in northeastern Russia, and is bordered by the Laptev Sea from the North, East and West, as well as by the Chekanovsky and Kharaulakh mountain ridges from the South (Fig. 5). It occupies more than 1500 islands of various sizes and totals about 30 000 km² in area, and is the largest delta in the Arctic. The Lena River Delta belongs to the Lena Delta Wildlife Reserve, the largest protected area in Russia, founded in 1985. The fauna of the Reserve includes 109 species of birds, 43 species of fish, and 32 species of mammals amongst which lemming, polar fox, wolf and wild reindeer are the most abundant (Sofronov, 2001).

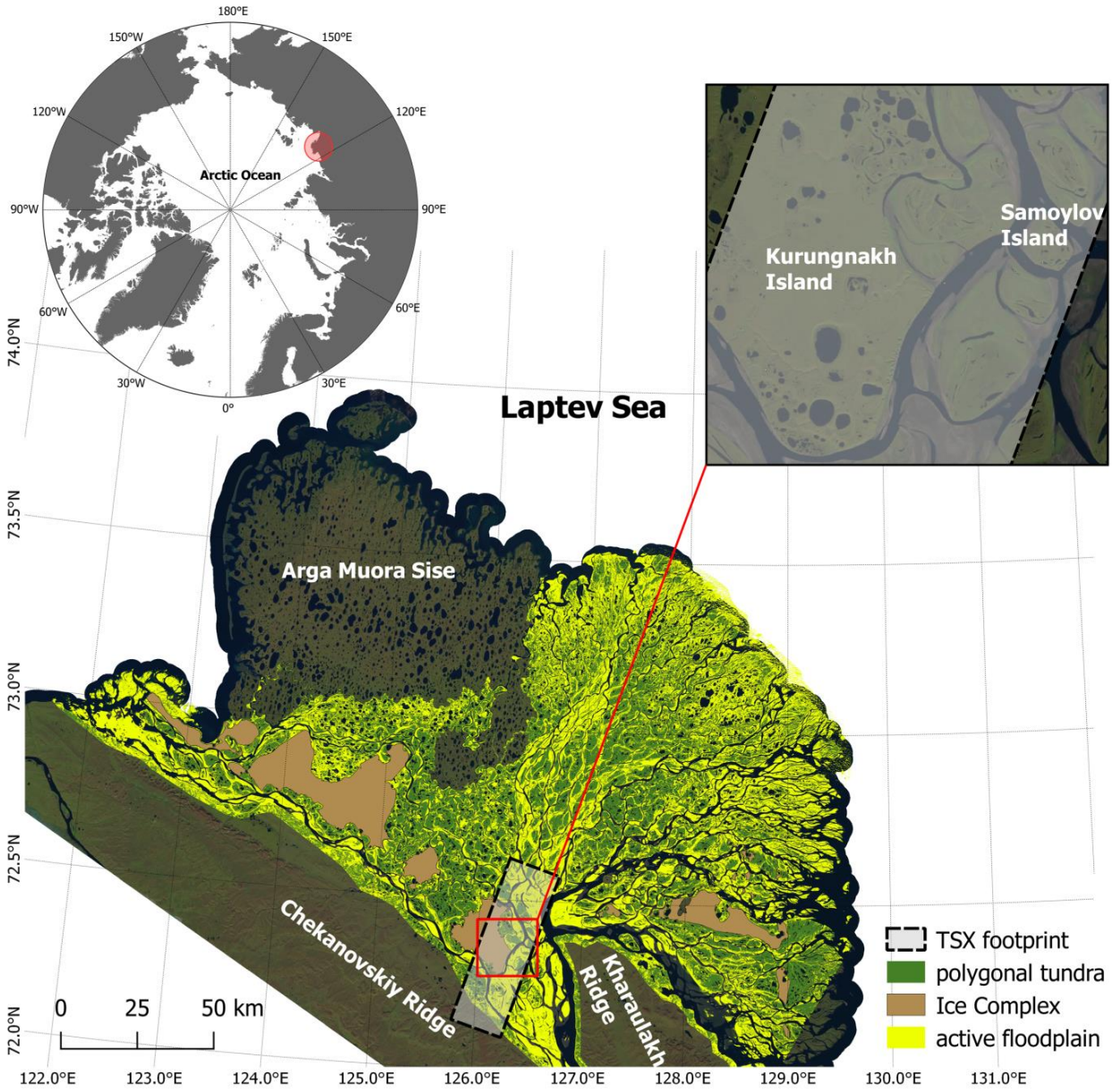

Figure 5. The study area located in the Siberian North (upper left) in the Lena River Delta, Siberia shown on Landsat-8 mosaic (NASA 2016). The Kurungnakh Island (upper right, enlarged red square) is the main study site. The TSX image frame is delineated in the black dashed rectangle. Landscape classification of the delta includes polygonal tundra, active floodplains and Ice Complex remnants (Morgenstern et al., 2011; Zubrzycki et al., 2013).

The climate in the Lena River Delta area is polar marine and characterized by extremely cold, long winters and short, cool summers. Boike et al. (2013) summarizes the recent climatic characteristics for the period 1999 to 2011 from the meteorological measurements in the central-southern part of the delta. The annual

mean air temperature is -12.5 °C (10.1 °C mean temperatures for July and -33.1 °C for February). Rainfall usually comprises more than half of the annual precipitation with a mean value of 125 mm. Snow accumulation typically starts in late September and snow-melt lasts from mid-May to early June. Wind-induced snow redistribution results in uneven snow thicknesses; however, snow depths are typically low on the order of a few decimeters.

The delta is located in the zone of continuous permafrost, which largely defines the geomorphology of the region. Permafrost depths reach up to 500-650 m, but decrease significantly towards the coast (Grigoriev, 1993). Active layer thickness varies from 0.3 to 0.9 m. Permafrost in the Lena Delta is classified as cold with temperatures of -9 °C at the depth of zero annual amplitude (Boike et al., 2012). A large submeridional fault splits the delta into two parts. Past tectonic movements are responsible for different altitudes of elevated units (Grigoriev, 1993). Modern uplifting comprises 0.5-1.9 mm per year (Borisov, 1973) resulting in regional seismic activity.

Geomorphologically, the major part of the delta is represented by active floodplains and a slightly elevated (up to 12 m above sea level (a.s.l.)) unit, which features regular polygonal relief (Fig. 5, 6a, 6c). The floodplains tend to grow in areal extent through sedimentation (Fig. 6b), while the elevated parts of the delta experience severe erosion due to permafrost thaw and river activity (Fig. 6c). Typically, the polygons have relatively dry elevated rims and wet (or water filled) low centers; however, high-center polygons are also present (Grigoriev, 1993). Mosses cover the largest fraction of the land surface. Additionally, dry tundra on polygon rims and high centers is represented by a few species of herbaceous and flowering plants, as well as willow shrubs and lichens. Wet tundra in low polygon centers is dominated by hydrophilic mosses, sedges, and marsh cinquefoils. Water bodies in this area mainly consist of numerous polygonal ponds a few meters in diameter and large thermokarst and oxbow lakes up to a few hundred meters in diameter (Muster et al., 2013) (Fig. 6c). The floodplain areas can include vegetated tundra (predominantly shrubs and sedges) and non-vegetated sandbanks (Fig. 6b) (Boike et al., 2013).

The north-western part of the delta is elevated by 20-30 m a.s.l. and represented by a few large sandy islands, with the largest, Arga Muora Sise Island, occupying 18% of

the delta (Fig. 5). Unlike other parts of the delta, this part is not dissected by river branches but characterized by numerous north-northeast oriented thermokarst lakes (Grigoriev, 1993).

About 6% of the delta is occupied by the remnants of a late Pleistocene accumulation plain, elevated by up to 60 m a.s.l., containing the so-called Ice Complex (or Yedoma) deposits (Fig. 5). The upper part of the Ice Complex deposits features large ice wedges up to 20 m deep, which can be observed from the natural cliff exposures (Fig. 6d). Typical topographic features of the Ice Complex uplands are thermokarst basins (known as *alases*), large thermokarst lakes, and thermo-erosional valleys (Morgenstern et al., 2011) (Fig. 6e, 6f). The vegetation is dominated by sedges and dwarf shrubs with a well-developed moss layer. Larger dwarf shrubs grow on the slopes of the gullies and in the depressions.

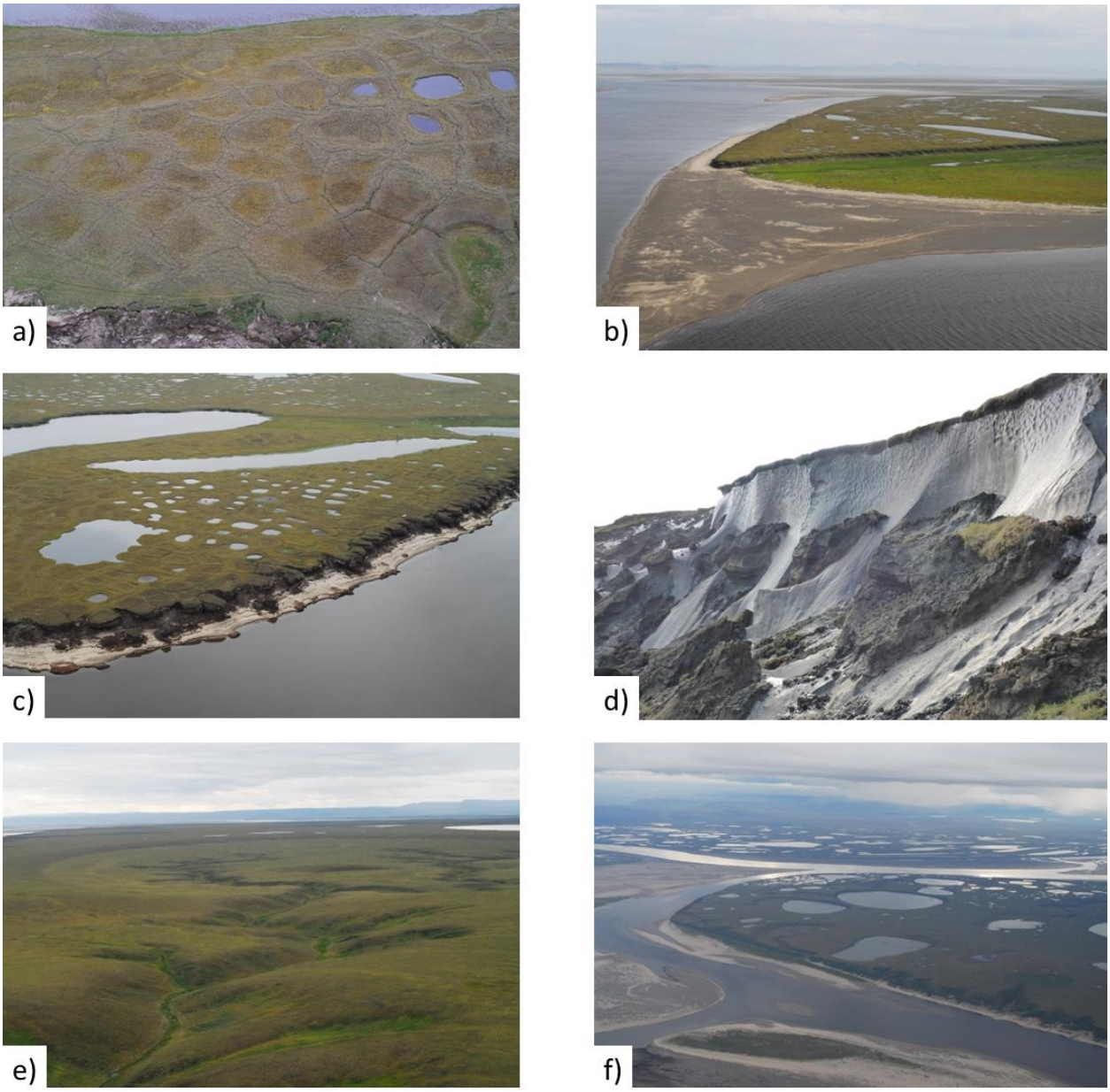

Figure 6. a) Aerial photograph of typical polygonal tundra relief; b) aerial photograph of a sandbank, floodplain, and elevated unit with polygonal tundra; c) aerial photograph of eroding polygons and water bodies, typical for polygonal tundra; d) cliff of the Ice Complex featuring giant ice wedges, which are up to 20 m deep; e) aerial photograph of a thermo-erosional gully with a thermokarst basin on the Ice Complex; f) aerial photograph of an Ice Complex island. The dimensions of these characteristic landscape elements range between orders of meters for the polygonal tundra in picture a) to the order of kilometers for the thermokarst lakes in picture f). All pictures are courtesy of the author.

The German Aerospace Center has recognized the Lena River Delta as a long-term permafrost-monitoring site and started seven new TSX acquisitions over the central part of the delta in August 2012 (Fig. 7a). Extensive field measurements were conducted in different parts of the delta by international research groups since the 1990s. A new research station opened on Samoylov Island in 2013, which facilitates year-round access to the site (Fig. 5, 7b).

The main focus area of this thesis was Kurungnakh Island in the central part of the delta belonging to the Ice Complex unit (Fig. 5, 6d, 6e, 6f).

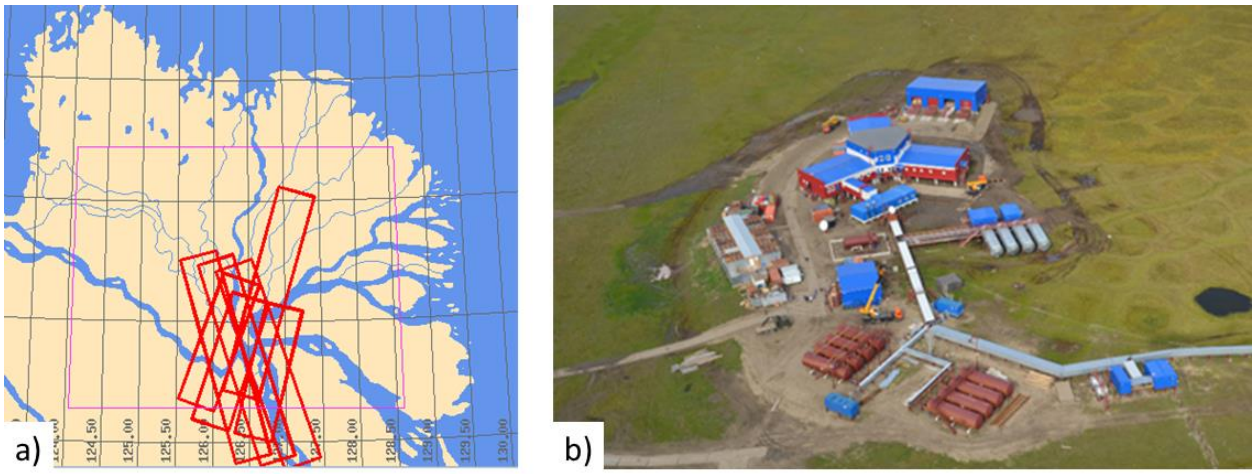

Figure 7. a) Seven relative TSX orbits over the central Lena River Delta (source: DLR); b) Aerial photograph of the new research station "Samoylov Island" (credit: M. Grigoriev).

1.3 Data and methods

1.3.1 SAR data

The SAR dataset used in this study includes 95 Single-Look Slant Range Complex (SSC) dual-polarisation (HH/HV or HH/VV) repeat-pass images acquired by TSX between August 2012 and October 2015. Since the work on this thesis began in 2013, parts of the study made use of shorter time series, including data which were available at the time. Only HH-polarised data were used. Table 1 provides all the technical details of the used TSX dataset.

Table 1. Details of TSX data (2012-2015) used in this study.

Wavelength	3.1 cm
Frequency	9.6 GHz
Slant range pixel spacing	0.9 m
Azimuth pixel spacing	2.4 m
Scene size	ca. 18x56 km
Revisit cycle	11 days*
Incidence angle	~32 °
Overpass	Descending
Looking	Right
Polarization	HH
Local time of acquisition	08:34 (UTC 22:34)

*there were some gaps in acquisitions

Details of SAR data processing can be found in the next chapters.

1.3.2 Field data

A variety of field data was used to interpret and validate the remote sensing results. Meteorological data, including air temperature, snow height, rainfall, wind speed, as well as daily descriptions of weather and surface conditions were available from the automated weather stations on Samoylov Island and from the human-operated meteorological station Khabarova (also known as Stolb, WMO ID: 21721). Photographs of the ground from an automated time-lapse camera on Samoylov Island were available as well. In spring 2015, in situ ice thickness was measured at 14 locations on a number of lakes with varying depths on Kurungnakh Island. Measurements of surface displacement due to melt and re-freezing of ground ice were conducted using steel pipes and fiberglass rods installed at least 1 m below the maximum active layer depth. 12 steel pipes were installed in the spring of 2013 and provided measurements up to 2015. In addition, 19 fiberglass rods were installed in the spring of 2014 and provided measurements up to 2015 as well.

1.3.3 Methods

The following methods were used for the three different case studies (i.e. environmental change detection, ice phenology and bedfast ice monitoring, and thaw subsidence detection).

1.3.3.1 Analysis of backscatter intensity and interferometric coherence for the detection of environmental changes

A one-year time series (2012-2013) of 35 TSX backscatter intensity images and 31 11-day coherence images were analysed. Six different landscape types that were likely to exhibit differences in backscatter and coherence variations were chosen for the extraction of regions of interest (ROIs): wet **polygonal tundra**, drier and more homogeneous **Ice Complex upland**, well-vegetated recently **drained lake basin**, partly vegetated/partly barren **floodplain**, **sandbank,** and area of **rocky outcrops** with absent or sparse vegetation. A variety of ground information, such as meteorological data (air temperatures, precipitation, wind speed), daily descriptions of weather and surface conditions, as well as photographs from an automatic time-lapse camera were used for the interpretation of backscatter intensity and coherence variations. Additionally, principal component analysis (PCA) was applied to the time series of backscatter and coherence images. PCA aids in extracting the maximum information from redundant data, such as multi-temporal imagery. Axes of multi-dimensional data are transformed in such a way that the new axes, which are the principal components, stand for variances within the data, with the first principal component accounting for the largest variance and the last principal component accounting for the smallest variance. Therefore, PCA can be useful for change detection. The eigenvector values of this transformation represent a correlation between each original image and each principal component. A more detailed description of the applied methods can be found in Chapter 2.

1.3.3.2 Analysis of backscatter intensity and interferometric coherence for the monitoring of lake ice phenology and bedfast ice

A three-year time series (2012-2015) of 95 TSX backscatter intensity images and 83 11-day coherence images were analysed. In situ measurements of ice thickness were conducted on a number of lakes on Kurungnakh Island. ROIs were chosen to contain the location of each in situ measurement. Temporal variations in the mean values of backscatter and coherence within the ROIs were analysed. Based on these variations, lake ice was attributed to a grounded or floating regime. This was verified with in situ measurements. Additionally, ice thickness was simulated with the one-

dimensional thermodynamic Canadian Lake Ice Model (CLIMo). Based on TSX-derived timing of ice grounding and simulated ice thickness, the thicknesses of grounded ice were obtained at the points of in situ measurements, which were used to validate the results. Ice phenology was monitored based on backscatter intensity variations caused by events related to lake ice evolution. A more detailed description of applied methods can be found in Chapter 3.

1.3.3.3 Differential SAR interferometry for the detection of thaw subsidence

During the course of working on the first case study, the 11-day coherence time series was analysed for one year (2012-2013). The annual coherence cycle exhibited large variability and coherence was found to be poor for many pairs. The summer of 2013 featured suitable coherence for a continuous series of 11-day and 22-day interferograms. Differential interferograms were produced using a DEM, which was derived from an interferogram from the same TSX dataset. These individual interferograms were affected by atmospheric artefacts; therefore, cumulative displacement over the summer was obtained. Field measurements of vertical ground displacement were used for the validation of interferometry. A more detailed description of applied methods can be found in Chapter 4.

1.4 Main results

The following section summarizes the results of the three case studies, which are documented in detail in the corresponding articles (Chapters 2, 3 and 4).

1.4.1 Environmental land surface changes detection

Due to its short wavelength, the TSX signal has limited penetration through the vegetation layer. Therefore, the backscatter intensity for the vegetated land surfaces expectedly demonstrated little variations throughout the annual cycle. Sequential 11-day coherence time series, on the other hand, demonstrated remarkable variability during the same time period. Seasonal and intra-seasonal land surface changes, detected by meteorological records and time-lapse camera photographs, were compared to variations in backscatter intensity and coherence. Backscatter intensity was insensitive to ground freezing and thawing and generally to variations in

precipitation. However, a continuous rain event, which lasted for nine hours before and also at the time of TSX acquisition, resulted in a 2-3 decibel (dB) increase of backscatter intensity. Backscatter intensity was also found to be generally insensitive to the presence of snow cover; however, a strong snow shower, which coincided with abnormally high air temperature of -13 °C in December, resulted in a 1 dB decrease of backscatter intensity. The spring snowmelt period featured a refrozen crust on the surface of the snowpack at the time of TSX acquisition and resulted in a 3 dB increase of backscatter intensity. Flooding of the sandbank was evident from remarkably low backscatter values on the order of -23 dB. Various surface types demonstrated differences in backscatter intensities: rough and poorly vegetated rocky outcrops generally returned the highest backscatter; the smooth barren sandbank yielded the lowest backscatter, and vegetated regions yielded intermediate backscatter values.

The coherence dropped significantly after the snow cover onset and snow melt for all of the land surface types. Generally, coherence was higher in winter, reaching 0.8 in January and February for vegetated surfaces, as well as the sandbank, and 0.9 for the rocky outcrops. In summer, vegetated regions yielded low coherence on the order of 0.3–0.4 and rocky outcrops showed variable coherence in the range from 0.4 to 0.8. The lack of more detailed information on vegetation (i.e. phenology stages) and snowpack properties (e.g. moisture, grain size, and density), as well as the absence of any on-site observations at the remote locations (e.g. rocky outcrops), did not allow for an explanation of coherence variability except when the latter was caused by snow cover onset and melt.

PCA of the backscatter intensity stack revealed that the PC2 eigenvector was highly correlated (0.91) with surface air temperatures. This could indicate a latent relationship between backscatter and temperature, which was not observed by direct comparison.

The demonstrated level of coherence was, in general, suitable for the interferometric analysis of seasonal ground subsidence associated with the thawing of the active layer. The freezing period featured poor coherence for many pairs. Interferometry analysis is the subject of the third case study of this thesis (Chapter 4).

1.4.2 Monitoring ice phenology and bedfast ice

TSX backscatter intensity demonstrated excellent viability for monitoring floating and bedfast (or grounded) ice regimes. Backscatter intensity of floating ice demonstrated a stable response during the winter on the order of -10 to -4 dB, whereas shallow lakes eventually experienced a decrease in backscatter intensity, indicating the ice grounding. Backscatter intensity signatures were mostly confirmed by in situ ice thickness measurements conducted during the last year of the study period. For a number of cases, backscatter intensity demonstrated an abrupt and clear drop (up to 8 dB); however, for some other cases backscatter intensity decreased gradually over one to two months, complicating the monitoring of ice grounding. The high temporal resolution of the TSX time series generally allowed for the extraction of the timing of ice grounding within the 11 days intervals, but sometimes posed a challenge due to a multi-step backscatter drop. Such a multi-step drop was possibly caused by the freezing of sediments or non-uniform grounding of the ice within the area of the mean backscatter extraction. Also, ice thickness was simulated using the lake ice model CLIMo and the thickness of grounded ice for each season was retrieved using the TSX-extracted timing of ice grounding. Comparison with grounded ice thicknesses, measured in situ in the last year of study period, showed fairly good agreement in the year of in situ measurements and poor agreement in the previous two years. The poor agreement might be due to differences in the lake water level between years, or incorrect extraction of the time of ice grounding.

Coherence generally demonstrated sensitivity to the ice grounding as well as to backscatter intensity. An increase of coherence from 0.2 (steady noise) to the range of 0.3 to 0.6 indicated ice grounding for two of three winter seasons. This increase occurred typically later than the backscatter drop and often coherence gradually increased until the onset of spring melt.

Ice phenology stages were generally tracked by TSX backscatter intensity time series. Freeze onset was characterized by low backscatter (on the order of -20 dB) which was often indiscernible from open water. However, contrasting cracks and ridges visible in the image provide evidence of the onset of freezing. Backscatter intensity

then gradually increased, reaching the stable condition (on the order of -10 to -5 dB), which persisted, in the case of floating ice, until the melt onset. Melt onset was detected in most cases by an alteration of backscatter intensity from its winter stable condition. However, the timing of alterations differed between locations and alterations were both positive and negative. Furthermore, a prominent drop of backscatter intensity up to 13 dB, consistent in time for most of the locations, was observed in each season and could be due to water ponding on the ice surface. A rapid drop of interferometric coherence in spring, observed for grounded ice in the first and last seasons, was consistent in time for all grounded locations, and could therefore serve as an additional more robust indicator of snow melt onset. On the other hand, the use of coherence was limited to shallow water bodies characterized by grounded ice. Water clear of ice was detected visually in the case of no-wind by low backscatter from the open water.

1.4.3 Vertical ground displacement detection

Field measurements showed tangible seasonal and inter-annual subsidence for two years of observations. The magnitude of seasonal subsidence was different for the two climatically different summer seasons. The cooler summer (2013) showed a mean subsidence at the end of August (relative to the observation from the previous spring) of 1.7±1.5 cm (mean for 8 sites). The warmer summer (2014) showed a mean subsidence of 4.8±2 cm (mean for 31 sites).The different summer climatic settings and, consequently, different summer subsidence magnitudes were responsible for the different inter-annual displacement patterns of the two following winter seasons. Measurements in the spring after the cooler summer showed both uplift and subsidence relative to the initial reference, in the range of -2 to +1.5 cm. Measurements in the next spring, after the warmer summer, showed a well-pronounced subsidence over two years, with a mean of 4.4±2.6 cm.

High spatial variability of displacements was detected with the in situ measurements. It is likely that the main controlling factors that influence the spatial variability are local topography and wetness variations. Two sites in wet local depressions demonstrated almost no displacement, whereas two other sites on relatively high and dry spots showed a subsidence of 2.5 cm each during the cooler

summer. Sub-meter variability in subsidence of up to 5.6 cm was observed in the warmer summer.

DInSAR cumulative displacement demonstrated slight displacements from -1 to +0.5 cm for the cooler summer. Subsidence was more pronounced in thermokarst basins, although still not larger than 1 cm. Obvious was significant underestimation of DInSAR-derived subsidence compared to in situ data. A large part of the 11-day interferograms for the warmer summer was strongly decorrelated and consequently precluded DInSAR analysis for this year.

1.5 Conclusions and Outlook

This thesis contributes to ongoing efforts aimed at developing remote sensing schemes for permafrost landscape observations by assessing the potential of unprecedented TSX time series with an 11-day repeat cycle, multi-year length, and high spatial resolution. Different applications for indirect permafrost monitoring in the Lena River Delta were addressed by a comprehensive TSX time series analysis. Extensive use of ground truth data were made in this study for the interpretation and validation of the remote sensing observations. The main findings are as follows.

1.5.1 Applicability of TSX backscatter intensity

TSX backscatter intensity was generally found to be insensitive to land surface changes, except for events occurring at the time of TSX acquisition (rain, snow shower, melt/freeze crust on snow). Therefore, the development of soil moisture and freeze/thaw monitoring algorithms for the tundra environment does not appear to be viable for X-band sensors. PCA of a one-year time stack of backscatter intensity images revealed a very curious dependency between a principal component's eigenvector and surface air temperature. Therefore, one of the future tasks is to check whether this dependency is valid for other years, areas, and radar data, as well as to determine a physical explanation of this phenomenon.

Much more promising is the prospect to monitor Arctic lake ice with TSX backscatter time series. This study shows that TSX backscatter intensity can very successfully detect bedfast lake ice. The improved temporal resolution of the TSX time series, compared to previously investigated SAR data, allows for a more accurate detection

of the timing of ice grounding. This information, together with an ice growth model, provide the thickness of grounded ice, and therefore, water depth in shallow water bodies. The study also revealed uncertainties regarding the extraction of the timing of ice grounding. These uncertainties are likely connected to the interaction between the SAR signal and the lake bottom or to the choice of a region for the backscatter averaging. This requires additional investigations and more field data for validation in future studies. Various TSX-based applications with utmost importance for hydrology and permafrost observations could be developed for Arctic lake ice monitoring. First of all, a rough estimation of the fraction of bedfast lake ice in the central Lena River Delta could be done based on already existing TSX acquisitions of the area. New one-time late winter acquisitions, which cover the entire delta, or even the entire Arctic, could be acquired for this purpose as well. This dataset would also allow for the estimation of talik distribution on regional or pan-Arctic scales. Depending on the TSX lifetime, multi-year monitoring of grounded lake ice fractions could be observed and linked to local impacts of climate warming (i.e. the change in maximum ice thickness or water level variations). Besides TSX, SAR data from other past and present missions, as well as from newly launched satellites, such as Sentinel-1 twin, could also be used for such analyses (when available for an area). However, combining data from different sensors with different wavelengths, spatial/temporal resolution, radiometric accuracy, and incidence angle is very challenging.

While 11-day temporal resolution is considered to be high for bedfast ice detection compared to the previous studies, this resolution is rather coarse for lake ice phenology monitoring. In this study the main events in lake ice phenology (freeze up, melt onset, and water-clear-of-ice) were mostly well detected by TSX backscatter on the order of 11 days. However, the timing of these events could be significantly improved by using data from existing overlapping TSX acquisitions. In this case, however, the geometries of the different acquisitions have to be taken into account. Sentinel-1 data with a 6-day revisit cycle could also significantly improve the temporal resolution. Still, depending on the purpose of an application, an 11-day TSX revisit cycle can be useful for ice phenology monitoring, especially in Arctic regions, where optical data are often unavailable due to strong cloudiness.

1.5.2 Applicability of interferometric coherence

Time series of sequential interferometric coherence showed a large variability over one year of the study. Mostly, this variability could not be explained by available meteorological data. The coherence was likely sensitive to processes that were too site-specific and too small scale to be reflected in available meteorological data. Further investigations are needed to elucidate the response of coherence on the surface changes. However, snow cover onset and snow melt coincided with total decorrelation over the entire image, suggesting a possibility to detect these events by using coherence. The use of coherence for this purpose is especially valuable because TSX backscatter did not react on snow cover onset. The coherence time series was also shown to detect bedfast ice in shallow lakes, although the signal was not as straightforward as backscatter intensity and could be partly contaminated by noise from surface effects, such as snow drift. Alternatively, the signal could be affected by penetration into lake sediments. However, the latter could potentially help monitor freezing of lake sediments.

Such coherence study provided valuable insights into the potential of SAR pairs, suitable for interferometric analysis.

1.5.3 Ground displacement observations

TSX DInSAR cumulative displacement underestimated subsidence, which was directly measured in the field. The observed high spatial variability of in situ displacements, even on a sub-meter scale, posed a challenge for the interpretation of interferometry results. Thus, it is likely that conventional DInSAR processing flow is unsuitable for permafrost landscapes. Alternative ways of processing should be considered in the future to accurately represent the spatial variability of thaw displacement. Most of the previous studies exploring DInSAR analysis for the estimation of displacements in permafrost areas did not use ground truth data for the verification of remote sensing results. This study suggests that even though DInSAR can generate a thaw displacement map, the accuracy of its results is potentially poor when compared to in situ measurements. The DInSAR analysis in this study was generally limited by often low coherence of TSX pairs, even with a minimal time span. Previous investigations and this study suggest that using a

longer wavelength is likely more viable for DInSAR analysis in tundra environments than using the X-band. However, even for longer wavelength, DInSAR processing should be carefully controlled.

Overall, this thesis highlights the limitations and potential of long-term TSX time series with high temporal resolution. Limitations are mainly related to the shallow penetration depth of the X-band signal and, consequently, the general insensitivity of backscatter to land surface changes and a quick interferometric coherence loss. On the other hand, the coherence loss can indicate some of these surface changes (e.g. snow cover onset and snowmelt). Based on this study, the major potential of TSX in permafrost landscapes is lake ice monitoring, which should be further developed in future work.

2

Spatio-temporal variability of X-band radar backscatter and coherence over the Lena River Delta, Siberia

Abstract

Satellite-based monitoring strategies for permafrost remain under development and are not yet operational. Remote sensing allows indirect observation of permafrost, a subsurface phenomenon, by mapping surface features or measuring physical parameters that can be used for permafrost modeling. We have explored high temporal resolution time series of TerraSAR-X backscatter intensity and interferometric coherence for the period between August 2012 and September 2013 to assess their potential for detecting major seasonal changes to the land surface in a variety of tundra environments within the Lena River Delta, Siberia. The TerraSAR-X signal is believed to be strongly affected by the vegetation layer, and its viability for the retrieval of soil moisture, for example, is therefore limited. In our study individual events, such as rain and snow showers, that occurred at the time of TerraSAR-X acquisition, or a refrozen crust on the snowpack during the spring melt were detected based on backscatter intensity signatures. The interferometric coherence showed marked variability; the snow cover onset and snow melt periods were identified by significant reduction in coherence. Principal component analysis provided a good spatial overview of the essential information contained in

backscatter and coherence time series and revealed latent relationships between both time series and the surface temperature.
The results of these investigations suggest that although X-band SAR has limitations with respect to monitoring seasonal land surface changes in permafrost areas, high-resolution time series of TerraSAR-X backscatter and coherence can provide new insights into environmental conditions.

2.1 Introduction

Permafrost affects nearly 24% of the land surface in the northern hemisphere, making it one of the largest areal components of the cryosphere. According to Hugelius et al. (2014), permafrost soils in the northern hemisphere contain a total of about 1300 Pg of organic carbon. The release of carbon dioxide and methane from thawing arctic permafrost is currently a major focus of climate change science. Moreover, irreversible landscape transformations resulting from a warming climate (e.g. thaw subsidence, thermo-erosion, and slope failure) disturb the hydrology, fluxes of energy and matter, and moisture balance, affecting both ecosystems and human infrastructure (e.g. Nelson et al., 2001; Kääb, 2008; Osterkamp et al., 2009; Jorgenson et al., 2013). These far-reaching consequences make the monitoring of the thermal conditions and structural stability of permafrost and the prediction of its future state particularly important.
Sporadic and intermittent in situ observations are often inadequate for monitoring surface changes considering the vastness, remoteness, and poor accessibility of the Arctic region. Satellite remote sensing offers a possible alternative that is able to provide both regular observations and broad spatial coverage. Satellite monitoring systems are well established for other components of the cryosphere (e.g. glaciers, sea ice and snow cover), and provide essential information on the processes and impacts of a changing climate on the Arctic region. In contrast, no such monitoring systems currently exist for permafrost, mainly because permafrost is a sub-surface element and cannot be monitored directly through satellite observations (Westermann et al., 2015a).
However, various land surface changes that occur in association with permafrost degradation (such as the formation, expansion, and drainage of lakes, or the

occurrence of thaw slumps and ground thaw subsidence) are observable by remote sensing and can therefore provide insight into the actual condition of the underlying permafrost (e.g. Duguay et al., 2005; Riordan et al., 2006; Mars & Houseknecht, 2007; Lantuit & Pollard., 2008; Jones et al., 2011; Günther et al., 2013). In addition, different remote sensing products such as land surface temperature and snow water equivalent can be used as forcing data for permafrost modeling (Langer et al., 2013; Westermann et al., 2015b). Despite a number of successes in the use of remote sensing for permafrost-related problems, operational satellite-based permafrost monitoring systems remain under development and in need of further improvement (Westermann et al., 2015a).

2.1.1 SAR backscatter intensity for seasonal change detection

Microwave imagery has a distinct advantage over optical imagery in polar areas as it allows data to be acquired independently of cloud cover and solar illumination. Synthetic Aperture Radar (SAR) is an active microwave system that transmits pulses of energy to the target and receives an echo of these pulses through an antenna. The backscatter intensity (subsequently referred to simply as backscatter) of an SAR signal is the portion of transmitted energy that is received by the system. Two properties of the backscattering surface that mainly define the backscatter are the surface roughness and the dielectric constant of the backscattering media. Since the presented study has one focus on radar backscatter, we outline those factors that have the potential to influence backscatter in the context of a typical tundra environment underlain by permafrost. There are static conditions such as the variations in surface roughness associated with different land cover types, and dynamic conditions associated with, for example, soil moistening and drying, soil freezing and thawing, or snow cover onset and melt. Higher surface roughness (relative to the SAR wavelength) typically causes diffuse scattering resulting in higher backscatter, whereas smooth surfaces cause more specular reflection of the signal resulting in lower backscatter. Where surfaces are vegetated it is important to take into account volume scattering within the vegetation which can significantly alter the total backscatter either due to increased backscatter by leaves and branches

or due to attenuation of the backscattered signal from the terrain beneath the vegetation layer.

The moisture of soil or vegetation affects the backscatter due to variations in their dielectric properties with water content. Moister soil normally results in higher backscatter than the drier soil. The relationships between radar backscatter and soil moisture have been investigated by, for example, Ulaby et al. (1978, 1979), Kane et al. (1996), Lu & Meyer (2002). The backscatter from frozen ground appears similar to that from dry ground because the dielectric constant is much lower for water in a frozen state than for water in a liquid state. Freezing of the ground therefore typically reduces the backscatter and thawing results in a higher backscatter. The influence of ground freezing and thawing on backscatter has been investigated by, for example, Wegmüller (1990) and Rignot & Way (1994). The presence of snow cover affects backscatter in a more complicated manner than freezing and thawing or variations in soil moisture. This is due to complex backscattering within the snowpack and from its surface, as well as from the surface of the ground beneath (if reached by the radar waves). SAR system properties, acquisition parameters, and snowpack conditions all have a strong influence on the observed backscatter. Dry snow typically appears "transparent" to SAR frequencies such as those in X-band and lower, and backscattering occurs mainly from the ground surface beneath the snowpack (e.g. Mätzler & Schanda, 1984). Wetting of the snow can have a major effect on the backscatter as the dielectric contrast at the air-snow interface becomes significant and energy transmission into the snowpack is reduced. The snow surface properties then begin to have a major effect on the backscattered signal, with smooth surfaces (relative to the wavelength of the signal) resulting in low backscatter due to specular reflection of the signal and rough surfaces resulting in higher backscatter.

Volume scattering within the snowpack is influenced by the SAR frequency and acquisition incidence angle, as well as by the properties of the snow such as its density, liquid water content, and grain size. Snow metamorphism, such as changes in crystal size and structure or the formation of ice lenses or layers, can also influence backscatter (e.g. Du et al., 2010). Backscatter signatures from different snow conditions have been investigated by, for example, Strozzi et al. (1997) and Nagler & Rott (2000).

Radar parameters such as frequency, incidence angle, and polarization configuration had a strong influence on the results of the above-mentioned investigations, for which C-band scatterometers and SAR were commonly used. Far fewer investigations into the conditions and processes related to permafrost have been carried out using higher frequency X-band sensors due to the limited availability of such data to date. Among these are investigations by Regmi et al. (2012) who used TerraSAR-X backscatter for dating drained thermokarst lake basins, by Ullmann et al. (2014) who carried out polarimetric analysis of TerraSAR-X data for different tundra surfaces in the Canadian Arctic, and by Duguay et al. (2015) who tested the use of TerraSAR-X backscatter for monitoring tundra shrub growth.

2.1.2 SAR interferometric coherence

A second focus of this study is on radar coherence over permafrost landscapes. In contrast to SAR backscatter analysis, SAR interferometry (InSAR) exploits the phase component of the microwave signal. It uses the phase difference between two SAR images covering the same area but acquired at different times to detect surface displacements. InSAR has been shown to be a powerful technique for detecting ground displacement associated with earthquakes and volcanic eruptions (e.g. Massonnet et al., 1993). The method has also recently been tested for monitoring permafrost thaw subsidence and frost heave (e.g. Rykhus & Lu, 2008; Liu et al., 2010; Short et al., 2011; Strozzi et al., 2012; Liu et al., 2014; Liu et al., 2015; Beck et al., 2015). Other applications of InSAR are for monitoring water level and inundations in the wetlands (e.g. Alsdorf et al., 2000; Hong et al., 2010; Xie et al., 2013) and for the retrieval of snow water equivalent (Guneriussen et al., 2001; Rott et al., 2003; Deeb et al., 2011).

One of the main limitations of InSAR is the signal loss due to insufficient phase coherence between SAR datasets. This phase coherence (or interferometric correlation) over time indicates the quality of the interferometric phase. There are a number of possible reasons for a loss of phase coherence including thermal noise from the antenna, a large interferometric baseline, topographic effects, misregistration between the SAR images, and atmospheric effects, but it can also be due to land surface changes that occur between SAR acquisitions (Zebker and

Villasenor, 1992). The latter are of special interest here because if all other factors causing decorrelation are minimized, the temporal decorrelation due to changes in the land surface can be used as a direct geophysical signal for the detection and interpretation of such changes (e.g. Rignot & van Zyl, 1993; Wegmüller & Werner, 1997). Interferometric coherence is defined by both amplitude and phase components of the SAR signal and is therefore potentially more sensitive to changes in the land surface than amplitude variations alone. The use of coherence has, however, been less investigated compared to the use of changes in backscatter. Examples of coherence use include the detection of changes in glacier surfaces (Weydahl, 2001a), delineation of the extent of glaciers (Atwood et al., 2010; Frey et al., 2012), Arctic ecozones classification (Hall-Atkinson & Smith, 2001), and mapping wet snow covers (Strozzi et al. 1999).

Similar factors to those influencing backscatter (as discussed in the previous sub-section), may also affect coherence. Some studies have used SAR coherence to supplement backscatter for the detection of temporal changes to the ground conditions (e.g. Rignot & van Zyl, 1993; Strozzi et al., 1999; Moeremans & Dautrebande, 2000; Barrett et al., 2012). The results of these investigations have suggested a limited sensitivity of coherence to moisture variations or soil freeze and thaw (i.e. to changes in dielectric properties) compared to variations in backscatter. Far more marked decorrelation can occur due to physical displacement of backscattering elements (for example, due to soil ploughing), a complete change in the nature of backscattering elements (such as from snow-free to snow-covered surfaces, or from bare ground to vegetated ground), or to volumetric decorrelation caused, for instance, by volume scattering in the vegetation layer. The level of decorrelation also depends on the time span between the SAR images used to compose coherence images relative to the rate of change of the backscattering elements, and on the wavelength of the SAR signal. Wickramanayake et al. (2016) investigated all possible interferometric combinations of 34 RADARSAT-2 (C-band) images in order to evaluate coherence variability with respect to temporal baseline and master image.

2.1.3 Principal Component Analysis (PCA)

PCA is a well-established technique in remote sensing for the visualization of multidimensional data (e.g. Gonzalez & Woods, 2002). It reduces redundancy in multiband or multitemporal imagery, increases the signal-to-noise ratio and provides an opportunity to use multitemporal datasets for change detection. PCA transforms the axes of multidimensional data in such way that the new axes (the principal components) account for variances within the data, with the first PC accounting for the largest variance and the last PC accounting for the smallest variance. PCA has mainly been used in optical remote sensing applications, such as for multitemporal analysis of Normalized Difference Vegetation Index images (Townshend et al., 1985) or landscape change detection based on multisensor data (Millward et al., 2006). Few investigations have attempted to use PCA on SAR imagery for soil wetness assessments (Verhoest et al., 1998; Bourgeau-Chavez et al., 2005; Kong & Dorling, 2008).

2.1.4 Objectives

TerraSAR-X is a new generation X-band radar satellite that has been providing high spatial resolution (up to 1 m) and high temporal resolution (11 day repeat orbit) SAR imagery since 2008. On the one hand its short wavelength (2.5-3.75 cm) is expected to generate greater loss of coherence than longer wavelengths such as C-band (3.75-7.5 cm) and L-band (15-30 cm) over a given time span due higher probability of temporal decorrelation, because scatterers change or motion of a significant fraction of an X-band wavelength is more likely to occur on the surface. On the other hand exactly this effect could be beneficial for a more sensitive analysis of surface changes. However, the shorter revisit time of TerraSAR-X satellite compared to ERS, ENVISAT, RADARSAT or ALOS satellites (but not Sentinel-1 with 12 days, or 6 days once both satellites are in operation) may lead to improved coherence, thus to some extent potentially compensating for the greater loss of coherence due to the shorter wavelength.

In order to investigate the potential of TerraSAR-X for monitoring surface changes within typical Arctic lowland permafrost areas, this study made use of a time series of TerraSAR-X data from August 2012 to September 2013, covering the full range of

seasonal surface changes. These changes are important for the assessment of regional climate change impacts and as input and validation for numerical permafrost models. We have explored time series for both radar backscatter intensity and interferometric coherence over a variety of landscapes in the Lena River Delta region, also making use of detailed supporting information that is available on meteorological conditions and snow coverage.

This is, to the best of our knowledge, one of the first studies of Arctic Siberian lowland permafrost to analyse such a high-resolution time series of SAR imagery in terms of backscatter and interferometric coherence. The explorative nature of this work meant that our objective was not to come up with concrete models or algorithms for SAR analysis, but rather to highlight the potential and limitations of X-band time series for monitoring surface related processes in tundra permafrost landscapes.

2.2 Study area

Our investigation focused on the southern part of the Lena River Delta in Siberia (Fig. 8a). The delta occupies an area of about 30 000 km² and includes more than 1500 islands of various sizes. It lies within the zone of continuous permafrost, with permafrost thicknesses of up to 600 m (Grigoriev, 1960). The delta can be divided into three geomorphological units or terraces on the basis of their height above sea level, geological age, and the composition of the deposits (Fig. 8b). The first terrace (1–12 m a.s.l.) comprises the youngest deposits (from the mid-Holocene) and features ice-wedge polygonal tundra and modern floodplains. The second terrace (20–30 m a.s.l.), formed between the late Pleistocene and the early Holocene, is represented by sandy deposits that host numerous thermokarst lakes. The third terrace (20–60 m a.s.l.) is the remnant of a late Pleistocene accumulation plain and contains large quantities of ground ice known as Ice Complex deposits (Grigoriev, 1993; Schwamborn et al., 2002). The landscape in the delta as a whole has generally been shaped by water through erosion and sedimentation (Fedorova et al., 2015).

The scene frame of the repeat TerraSAR-X data used in this study covers parts of the first and third terraces, as well as an area of prominent rocky outcrops to the south of the delta (Fig. 8c). Our research focused in particular on two islands, each

representing one of these terraces: Kurungnakh-Sise (or Kurungnakh) Island (third terrace) and Samoylov Island (first terrace).

Pleistocene Ice Complex deposits, also known as Yedoma, comprise the main part of Kurungnakh Island (Figs.8e and 9c). Thermokarst basins (known as *alasses*), thermokarst lakes, and thermo-erosional valleys are typical topographic features of the Ice Complex upland of this island, with alasses and lakes occupying about 40% of the island's area (Morgenstern et al., 2011). Where the surface is unaffected by degradation processes the island is mostly flat, but the elevation decreases gradually from southeast to northwest. This gradual slope has provided favorable conditions for the development of a network of small drainages that covers the Ice Complex upland (Morgenstern et al., 2013). The vegetation consists of typical tundra plants dominated by sedges and dwarf shrubs < 40 cm tall, with a well-developed moss layer. Larger dwarf shrubs (birch and willow) grow on the slopes of the gullies and in the depressions. Tussocks are present on the slopes of alasses.

Samoylov Island features two types of landforms that are both typical of the first terrace: highly patterned ice-wedge polygonal tundra on the elevated river terrace, and the active floodplain of the Lena River (Figs. 8d, 9a-b and 9f-g). The surface of the terrace is generally flat but polygons form a distinctive microtopography. Water bodies with surface areas of less than 1000 m² are dominant in this permafrost landscape, in terms of both number and surface area (Muster et al., 2012; Muster et al., 2013). Relatively large thermokarst and oxbow lakes (up to few hundred meters in diameter) are also present. The polygonal tundra areas on the island can be considered to be a mixture of dry tundra (consisting mainly of the polygon rims and raised polygon centers) and wet tundra in the depressed polygon centers and cracks (Muster et al., 2012). Up to 98% of the land surface is covered by mosses. In addition to these mosses, the dry tundra also contains a few species of herbaceous and flowering plants, as well as willow shrubs and lichens. The wet tundra is dominated by hydrophilic mosses, sedges, and marsh cinquefoils (Boike et al., 2013). The floodplain consists of 56% vegetated tundra (predominantly dwarf vegetation) and 44% non-vegetated sandy banks (Boike et al., 2013).

The climate in the Lena River Delta area is subject to both marine and continental influences. Microclimatic variations occur across the delta depending on proximity

to the Laptev Sea and to mountainous ridges. However, extremely cold, long winters and short, cool summers are typical for the entire region. The climatic characteristics of Samoylov Island for the period from 1999 to 2011 have been summarized in Boike et al. (2013). The mean monthly temperatures were 10.1 °C for July and -33.1 °C for February. Summer precipitation typically occurred from the middle of May until the end of September, with a mean annual rainfall of 125 mm. The start of snow accumulation varied between late September and late October. The end of snow melt varied between late April and mid-June, but typically occurred around the end of May. Snow redistribution by the wind and the presence of polygonal microrelief combined to make the snow thickness extremely uneven, but the depth of snow cover did not exceed 56 cm (within a polygon center, in 2004). The duration of the snow melt period was approximately two weeks. The maximum mean active layer depth reached about 50 cm during August.

The main features of the annual energy balance for these sites with continuous permafrost in the subsurface typically include low net radiation, higher atmospheric latent heat flux than sensible heat flux, and a large proportion of soil heat flux (Langer et al., 2011a, 2011b). Previous publications have reported that shallow ponds (< 1 m deep) freeze completely in winter but that the timing of freeze-back can vary by up to 2 months between years, thus affecting the storage and production of methane (Langer et al., 2015). Larger thermokarst lakes remain unfrozen at depth, with mean annual lake –bottom temperatures of between 2.7 and 4 °C (Boike et al., 2015).

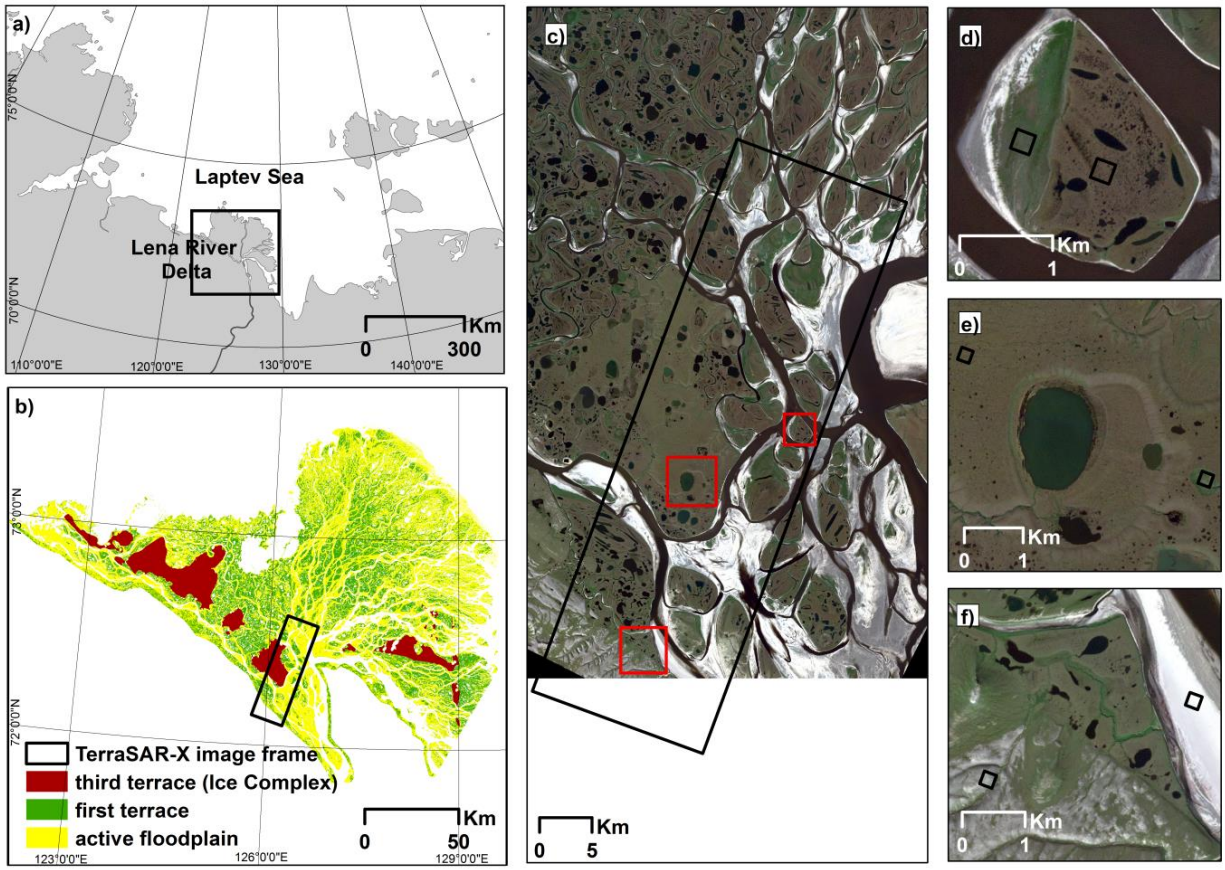

Figure 8. Study area. a) Laptev Sea region and the Lena River Delta with the black square frame delineating the area shown in b). b) Distribution of the first terrace, active floodplain, and third terrace within the Lena River Delta with the TerraSAR-X image frame delineated in black. c) RapidEye image (quasi true-color RGB 3-2-1; acquisition date: 4 August 2010) with the TerraSAR-X image frame delineated in black and the areas of the detailed images in d), e) and f) shown as red squares. d) Two regions of interest (ROIs) on Samoylov Island delineated in black. e) Two ROIs on the Ice Complex of Kurungnakh Island, delineated in black. f) Two ROIs, one on a sandbank and the other in an area of rocky outcrops, delineated in black.

2.3 Data and methods

2.3.1 SAR data

The German Aerospace Center (Deutsches Zentrum für Luft- und Raumfahrt, DLR) has designated the central Lena Delta as a long-term monitoring site that meets the Requirements for Monitoring of Permafrost in Polar Regions for the WMO Polar Space Task Group (Bartsch, 2014). The DLR has provided access to a unique dataset acquired by the TerraSAR-X satellite. TerraSAR-X (TSX) is a radar satellite launched in 2007, operating in X-band (wavelength 3.1 cm, frequency 9.6 GHz). The SAR dataset used in this study includes 35 Single-Look Slant Range Complex (SSC) images acquired by TSX between August 2012 and September 2013, at approximately 08:34 local time (UTC: 22:34). The time span between acquisitions was 11 days, with three exceptions when the time spans were 22 days. The StripMap imaging mode used in this study has a range and azimuth pixel spacing of 0.9 and 2.4 m, respectively. The scene size measured approximately 18 x 56 km. The chosen orbit was in descending pass and the radar was right-looking. The acquisition incidence angles were between 31.6 ° and 31.7 °, the polarization channel was HH for all used images.

2.3.2 TSX data processing

The data were processed using the GAMMA radar software (Werner, 2000). SSC data were converted to GAMMA Single Look Complex (SLC) format and the SLC data were then consecutively co-registered with subpixel accuracy (typically better than 0.2 pixel) in such a way that a co-registered slave image became a master for the next image. The co-registered SLC data were multilooked by factors of 4 and 3 in range and azimuth directions, respectively, in order to obtain intensity values with reduced speckle and roughly square ground range pixels. Intensity images were calibrated to sigma nought and converted to dB using:

$$\sigma^0_{dB} = 10\lg(k_s * |DN|^2 * sin\theta), \qquad (1)$$

where k_s is the calibration constant, DN is the amplitude of a complex number representing a pixel value of SLC data, and θ is the local incidence angle. According

to the TerraSAR-X Image Product Guide relative radiometric accuracy for the StripMap product is 0.3 dB and absolute radiometric accuracy is 0.6 dB.
Interferometric coherence, defined as the magnitude of the complex cross-correlation coefficient of an SAR image pair, was then computed using:

$$\rho(x,y) = \frac{\langle s_1(x,y) s_2^*(x,y) \rangle}{\sqrt{\langle |s_1|^2 \rangle \langle |s_2|^2 \rangle}}, \qquad (2)$$

where ρ is the coherence value at pixel location (x,y), s_1 and s_2 are the complex values of SLC images 1 and 2 at pixel location (x,y), and * stands for the complex conjugation. The spatial averaging (marked by ⟨ ⟩) was processed over a window of 3 x 3 pixels. Coherence varies from 0 (decorrelated signals) to 1 (perfectly correlated signals).
Coherence images, each with a temporal baseline of 11 days, were obtained from interferometric pairs of SLC images, co-registered in the manner described above.
To investigate the possible influence of a large spatial baseline on coherence loss we calculated the spatial correlation term using a formula from Zebker and Villasenor (1992):

$$\rho_{spatial} = 1 - \frac{2*|B|*R_y*cos^2(\theta)}{\lambda * r}, \qquad (3)$$

where B is the baseline, R_y is the range resolution, θ is the incidence angle, λ is the wavelength, and r is the radar to target distance. Taking the largest baseline in our dataset (≈300m), we obtain $\rho_{spatial} \approx 0.98$, indicating a negligible influence of the baseline on decorrelation.

2.3.3 Principal Component Analysis (PCA)

Both the backscatter intensity images and the coherence images were geocoded to the WGS84 ellipsoid with a pixel size of 10 x 10 m in the Universal Transverse Mercator (UTM) projection Zone 52N. Two time series were established based on the backscatter and coherence image stacks. We applied PCA to the time series of backscatter and coherence images using the PCA tool in ArcGIS™ (ESRI). We

present herein only the first few PCs for backscatter and coherence, noting that higher PCs might contain information of interest for specific investigations.

2.3.4 Time series for regions of interest

We chose six regions of interest (ROIs), each with dimensions of 30 x 30 pixels, within the SAR scene (Fig. 8d-f). These ROIs represented typical different landscape types that were likely to exhibit different seasonal variations in backscatter and coherence. They comprised an area of wet polygonal tundra (Fig. 9a, 9b and 9f), an Ice Complex upland area (Fig. 9c), a well-vegetated recently drained lake basin (Fig. 9d and 9e), a floodplain area (Fig. 9f and 9g), part of a sandbank (Fig. 9h), and an area of rocky outcrops to the southwest of Kurungnakh Island (Fig. 9i). We calculated the mean backscatter intensity and coherence values over each ROI for every intensity and coherence image and established time series of the mean values.

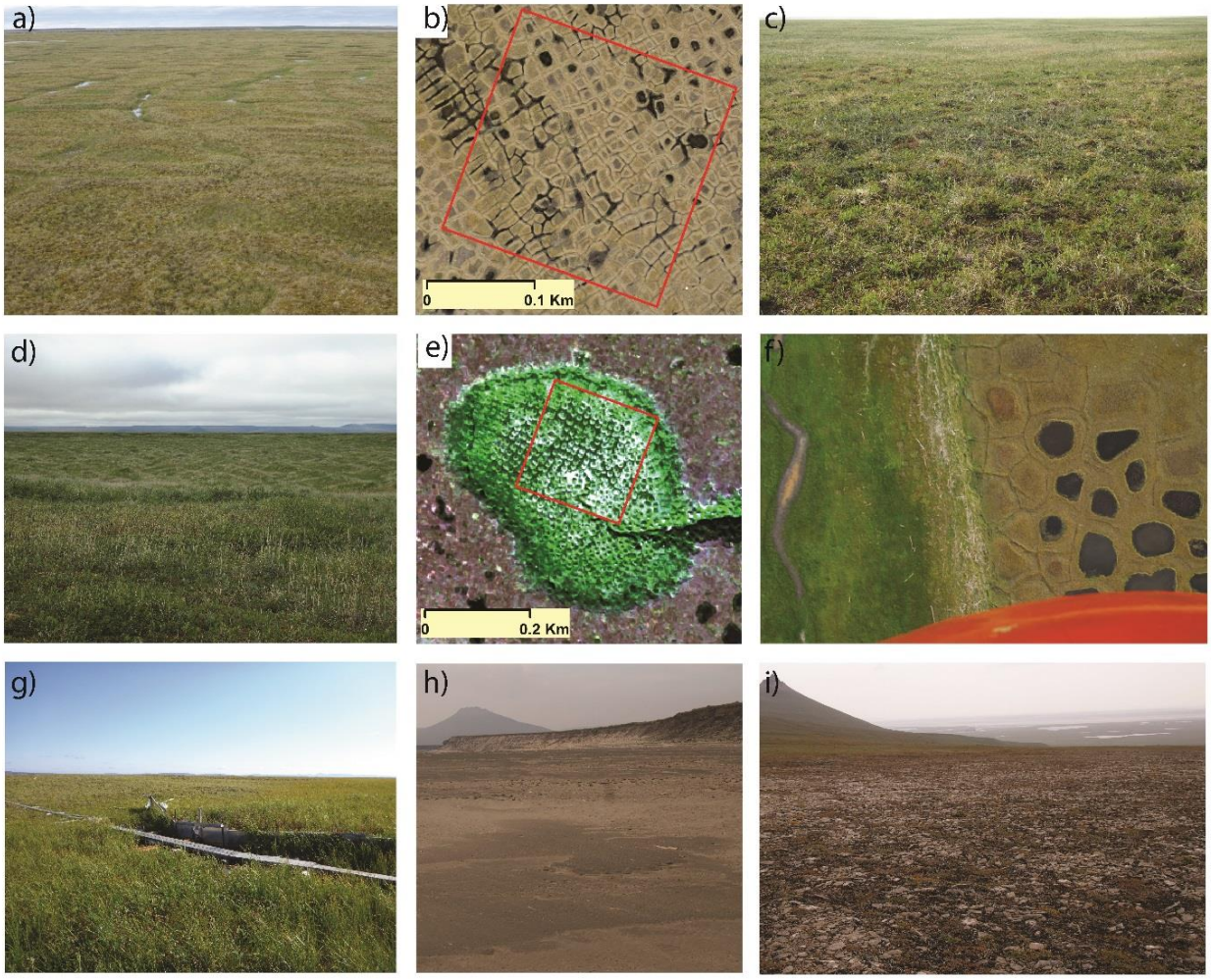

Figure 9. Regions of interest (ROIs). a) Wet polygonal tundra, Samoylov Island (see also Fig. 8d, right hand ROI). b) Subset of an orthorectified aerial photograph of polygonal tundra on Samoylov Island (Muster et al., 2012), with an ROI delineated in red (see also Fig. 8d, right hand ROI). The image shows distinct low-centered polygons, some filled with water and some with water between rims of adjacent polygons, all vegetated with thick moss layers and sedges. c) Ice Complex upland with a relatively dry surface, thick moss layers, and moderately pronounced hummocks up to 15 cm high (see also Fig. 8e, left hand ROI). d) Recently drained highly vegetated lake basin (see also Fig. 8e, right hand ROI). e) Part of a GeoEye-1 satellite image of the drained lake basin with the ROI indicated in red: very rough, hummocky surface with tall, vigorous shrub vegetation (see also Fig. 8e, right hand ROI). f) Aerial photograph covering part of Samoylov Island: the sharp boundary between green vegetated floodplain on the left and brownish polygonal tundra on the right can be clearly seen (see also Fig. 8d). g) Samoylov Island floodplain (see also Fig. 8d, left hand ROI). h) Non-vegetated, regularly flooded sandy area (see also Fig. 8f, right hand ROI). i) Typical rocky outcrops to the south of the Lena River Delta: distinct topographic features with hills and depressions; very dry surface features sorted stones with low, patchy vegetation (see also Fig. 8f left hand ROI).

2.3.5 Meteorological data

Land surface changes were interpreted in the context of meteorological conditions. Daily descriptions of weather and surface conditions at 09:00 local time (time of TSX acquisition was 08:34 local time) were available from the Khabarova hydrological station located about 10 km to the east of Samoylov Island (http://rp5.ru/Weather_archive_on_Stolb_Island; accessed April 2016) (see Table A1 in Appendix). Air temperature measurements, infra-red surface temperature measurements, snow height, liquid precipitation, and wind speed measurements were available from an automated weather station, located on Samoylov Island (data are published in PANGAEA). Plots of these variables can be found in the Appendix (Figs. A2 - A5). Some parameters were taken from both Samoylov and Khabarova stations for cross-validation. Visual observations of ground surface conditions were available through an automatic time-lapse camera installed at a height of 10 m on Samoylov Island (see Fig. A1 in Appendix,).

2.3.6 Optical satellite imagery

We used a series of Landsat-7 ETM (Enhanced Thematic Mapper) and Landsat-8 OLI (Operational Land Imager) images covering the spring and summer of 2013 for auxiliary information on the surface conditions in some of the ROIs. We also used an orthorectified and atmospherically corrected RapidEye multispectral optical image taken on 4 August 2010 for retrieval of the Normalized Difference Vegetation Index (NDVI) that is (Near Infrared - Red) / (Near Infrared + Red).

2.4 Results

2.4.1 Time series of backscatter for regions of interest

We first compared time series of backscatter for the different ROIs; the mean backscatter over the 30 x 30 pixel ROIs are plotted against the dates of acquisition in Figure 10. There is a notable difference in backscatter values over the different types of land cover and the ROIs yield different ranges of values during the different seasons. During the first snow-free season (03.08-27.09.2012) the rocky outcrops with very poorly developed and sparse vegetation yielded the highest backscatter (-10 dB), the floodplain yielded lower values (-12 dB), the Ice Complex upland, polygonal tundra and drained lake basin all yielded similar values (around -14 dB), and the barren sandbank, which was presumably smooth, yielded the lowest values (-17 dB). During winter (27.09.2012–24.04.2013) the backscatter from the rocky outcrops and the sandbank remained the highest and lowest respectively, but the range of values for each of the other four ROIs changed. During the second summer (07.06-14.09.2013) the sandbank yielded the highest backscatter values, with these falling to the values from the rocky outcrops by the end of the period. The polygonal tundra yielded the lowest values over this period (-14 dB), which were similar to those in the first summer. By the end of the second summer the backscatter from the polygonal tundra, the Ice Complex upland, the floodplain and the drained lake basin become almost identical to each other.

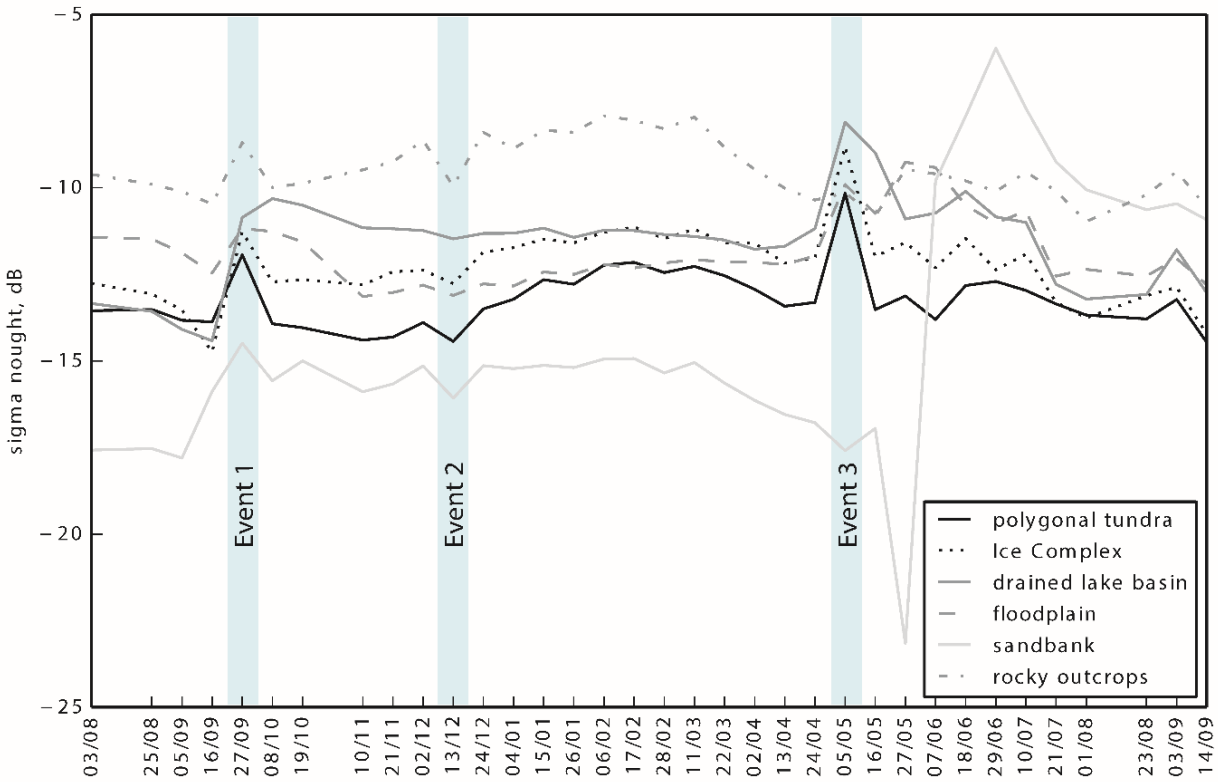

Figure 10. Mean backscatter time series for six ROIs (August 2012 to September 2013). Dates on x-axis are TSX acquisitions dates (date format: DD/MM). Distinct backscatter variations are marked as Events by blue shading.

We calculated the Normalized Difference Vegetation Index (NDVI) from a RapidEye multispectral optical image to distinguish between the different vegetation vitalities in our ROIs (Fig. 11). The NDVI values for the four vegetated ROIs showed a gradual increase from the polygonal tundra (median ~ 0.23) to the drained lake (median ~ 0.45). The rocky outcrop yielded significantly lower values than the four vegetated ROIs, with a median ~ 0.06. The backscatter values for the vegetated ROIs during the summer of 2013 differed from each other, varying almost according to their NDVI values: values for the Ice Complex were slightly higher than those for the polygonal tundra, values for the drained lake were higher than those for the Ice Complex, and values for the floodplain were higher than those for the drained lake (although the NDVI for the drained lake was higher than that for the floodplain). However, backscatter during August-September 2012 were only higher for the

floodplain, while values for the drained lake were even lower than those from the Ice Complex and the polygonal tundra.

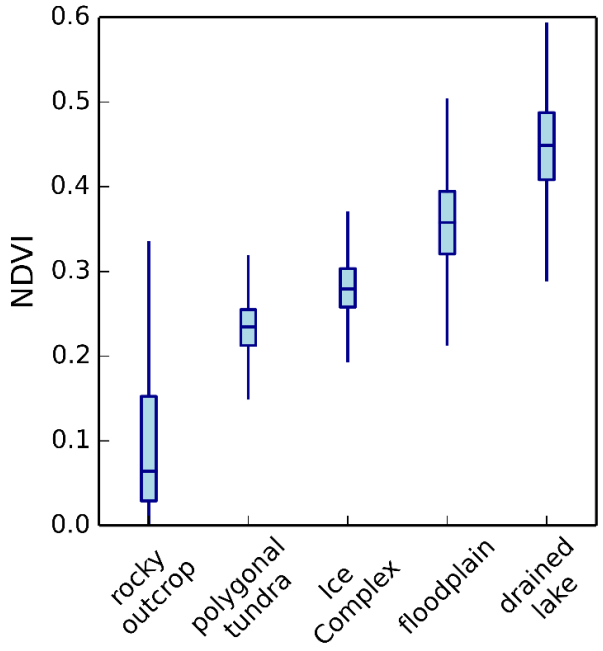

Figure 11. NDVI for all ROIs (except for the sandbank), derived from Rapid-Eye satellite image acquired on 4 August 2010. Minimum, 25% quartile, median, 75% quartile and maximum are shown using boxplots.

A number of distinct temporal variations in backscatter occur in the various ROIs. The first event was a 2-3 dB increase in backscatter on 27.09.2012, observed in most of the ROIs (Fig. 10). Meteorological conditions on this day featured continuous rain for a few hours before TSX acquisition, and also at the time of acquisition (Table 2).
The second event was a slight (~1 dB) but congruent decrease in backscatter for some of the ROIs (rocky outcrops, polygonal tundra and sandbank) on 13.12.2013 (Fig. 10). This event coincided with continuous snow fall at the time of TSX acquisition preceded by snow showers and with anomalously warm air temperatures (Table 2).
The third event was a distinct increase in backscatter values (~3 dB) on 05.05.2013 for four of the ROIs (excluding the rocky outcrops and sandbank) (Fig. 10). Day and night temperature variations around 0 °C were observed prior this date (Table 2), with patchy snow cover persisting in depressions (see Appendix, Fig. A1).

Table 2. Meteorological conditions close to the time of TSX acquisition for three specific dates (see Table A1 in Appendix for the rest of the TSX acquisition dates). Air temperatures were measured on Samoylov Island at 08:30 local time. Weather descriptions and surface conditions are from the Khabarova hydrological station at 09:00 local time.

Date	Air temperature	Weather	Surface condition
27.09.2012 (Event 1)	3.2 °C (previously positive all the time)	-constant, non-freezing light rain -also continuous during previous 9 hours	
13.12.2012 (Event 2)	-13.1 °C	-constant light snowfall -constant snowfall during previous 21 hours, including snow showers	uneven layer of dry, powdery snow covers the surface completely
05.05.2013 (Event 3)	-2.1 °C (previously positive during the days and negative during the nights)		packed or wet snow covers at least half of the surface

The backscatter for the Ice Complex, the drained lake basin and the floodplain ROIs revealed a slight but consistent decreasing linear trend during both summer periods (slope ~ -0.03 and R^2 typically higher than 0.65 for all three ROIs).

We also examined a series of Landsat-7 ETM (Enhanced Thematic Mapper) and Landsat-8 OLI (Operational Land Imager) images covering the spring and summer of 2013 to obtain auxiliary information concerning the conditions on the sandbank and the rocky outcrop surfaces (Fig. 12).

The sandbank ROI showed a distinctly different trend in backscatter during the spring and summer of 2013 from the other ROIs. There was no backscatter peak on 05.05.2013 which suggests different snow conditions and the Landsat image from 23.03.2013 shows a snow free sandbank surface, supporting this suggestion. There was a rapid reduction in backscatter from -17 to -23 dB on 27.05.2013 and the Landsat image from 28.05.2013 clearly shows flooding of the area. On 07.06.2013 the backscatter then increased rapidly to -10 dB and the Landsat image from 11.06.2013 shows river ice accumulated on the sandbank. The backscatter continued to increase for the next two measurements and then decreased gradually, remaining stable from August until the end of the summer. From the Landsat imagery, it seems likely that the accumulated river-ice floes took until the end of June to melt completely. Backscatter values from the sandbank in the summer of 2013 were

significantly higher overall than in the summer 2012. Both the sandbank and rocky outcrops ROIs demonstrated a decreasing trend in backscatter from 11.03 until 24.04.2013, although the Landsat imagery indicated that snow conditions on the rocky outcrops differed from those on the sandbank.

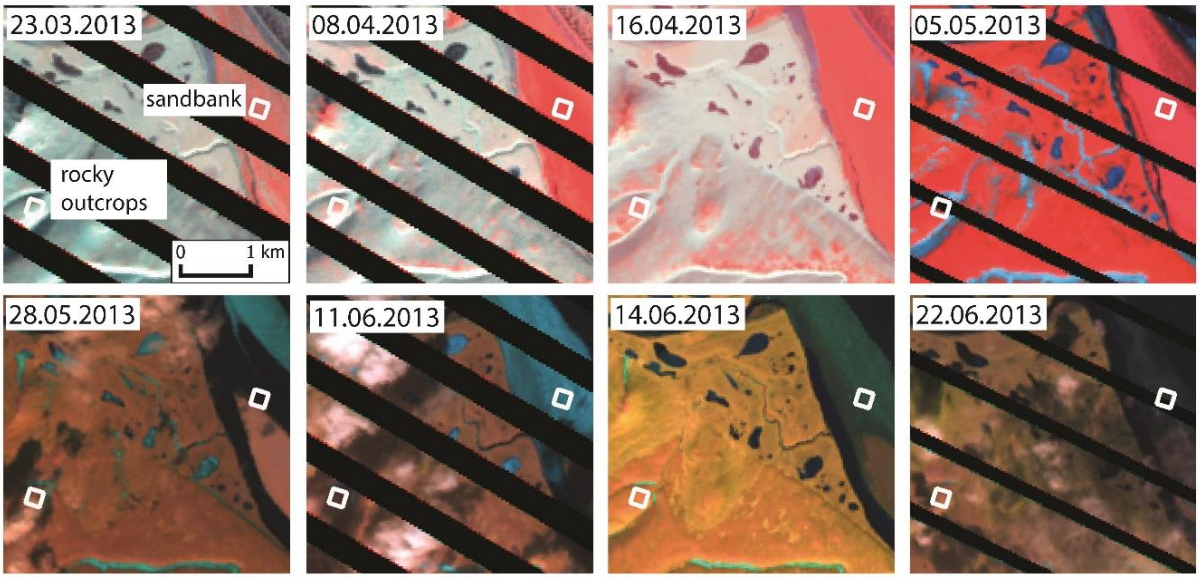

Figure 12. Series of Landsat-7 ETM (RGB 5-4-3) and Landsat-8 OLI (RGB 6-5-4) color composites of the sandbank and rocky outcrops ROIs (white rectangles) from March to June 2013, showing surface changes within the ROIs. Black stripes across the images are due to the failure of the Scan Line Corrector in the ETM+ instrument. Date format: DD.MM.YYYY.

2.4.2 Comparing coherence and backscatter time series

We selected four ROIs in which to compare coherence time series with backscatter time series, these being the polygonal tundra, drained lake basin, sandbank and rocky outcrops ROIs.

The coherence generally revealed greater variability than the backscatter (Fig. 13). The coherence in all four ROIs gradually decreased over the first summer (until the snow cover onset). The highest coherence during this period (0.6-0.9) was from the rocky outcrops ROI, followed by the sandbank ROI (0.4–0.7), and the polygonal tundra (0.4-0.6), with the drained lake basin (which was the most vegetated of the ROIs) returning the lowest coherence values (0.2-0.4). All the ROIs responded to snow cover onset with a reduction in coherence (down to ~0.2). The change in backscatter between 16.09 and 27.09.2013 due to continuous rain on 27.09, had

little effect on the coherence, except for the drained lake basin ROI, where there was a reduction in coherence coinciding with a change in backscatter.

Following the onset of snow cover the vegetated ROIs (polygonal tundra and drained lake basin) showed low coherence values (0.2 – 0.3) until the end of December. The coherence then increased, yielding the highest values (~0.75) in January and February and then decreasing again. The drained lake basin yielded greater variability during the winter than the polygonal tundra. Unvegetated or sparsely vegetated ROIs (the sandbank and rocky outcrops) did not show the same period of low coherence at the beginning of the winter, but instead showed an increase in coherence immediately after the onset of snow cover. The reduction in coherence observed for the rocky outcrops and sandbank ROIs in December coincided with a reduction in backscatter on 13.12.2013. Both of these ROIs yielded their highest coherence values (0.8-0.9) in January and February with the rocky outcrops yielding the highest coherence values (> 0.9) of all ROIs over that period.

All ROIs reacted to spring snow melt with a reduction in coherence down to ~0.2, except for the rocky outcrops where this reduction was less evident (with coherence values of ~0.4). The second summer period revealed greater variability in coherence between ROIs than the other seasons. The coherence of the polygonal tundra varied between 0.2 and 0.4, while the drained lake basin values were generally lower and varied between 0.2 and 0.3. The sandbank yielded low coherence values (0.2) until the end of June, which coincided with the spring flood and the presence of river ice. From the end of June the coherence started to increase (reaching 0.7 at the end of summer) and at the same time the backscatter started to decrease gradually. The rocky outcrops showed the largest variability in coherence (between 0.4 and 0.8) and at the same time the highest coherence values of all ROIs during the second summer period.

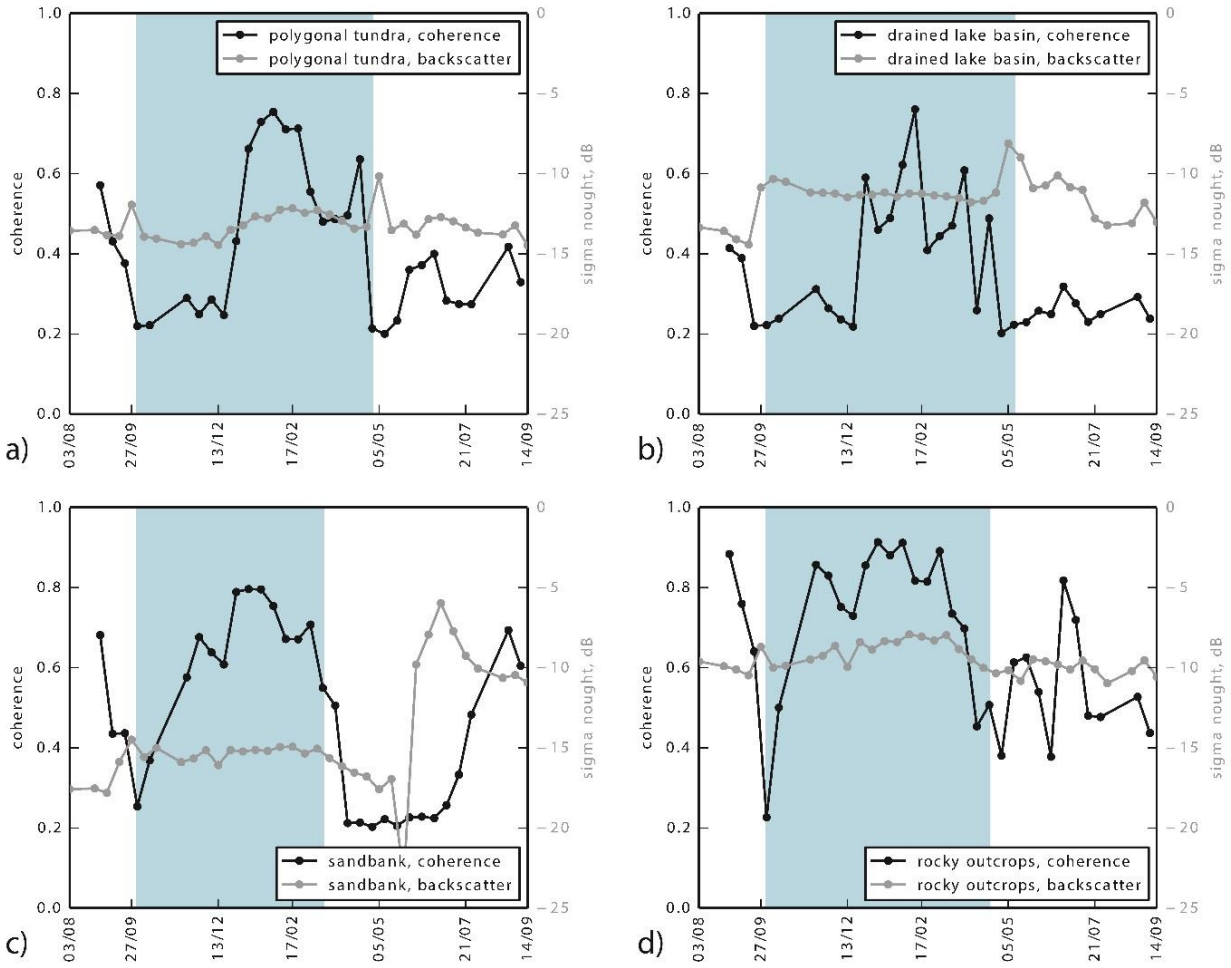

Figure 13. Mean coherence and backscatter intensity time series for four ROIs (August 2012 to September 2013). Dates on x-axis are selected TSX acquisition dates (date format: DD/MM). The light blue shading indicates the period of full snow cover (based on automatic time-lapse camera images from Samoylov Island, together with Landsat imagery).

2.4.3 Principal Component Analysis

2.4.3.1 PCA for the time series of backscatter images

In the PCA for the time series of backscatter images the PC1 accounts for 32.4% of the total variance (or unique information). It represents the dominant common backscatter features in the input image stack (Fig. 14a). The eigenvector values (representing a correlation between each original image and each PC) are all negative for PC1 indicating that high PC1 values correspond to low backscatter values, and vice versa (Fig. 15). This is also evident in the image representing the PC1: river channels show positive values while the strongest backscatterers (such as

rocky outcrops, highly eroded cliffs on the east shore of Kurungnakh and Samoylov Research Station in the southern part of Samoylov Island) are negative. Eigenvector values are very stable during the winter and more variable during the spring and both of the summers. The PC2 explains 20.6% of the total variance in the initial dataset. All water bodies are clearly distinguishable by low PC2 values (Fig. 14b). The PC2 eigenvector values demonstrate high seasonality, with positive values corresponding to warm periods and negative values to the winter. The PC2 eigenvector shows a remarkably strong correlation with surface temperatures recorded close to the time of each SAR acquisition (08:30 local time) by the automatic measurement station on Samoylov Island during the snow-free season: the correlation coefficient between these variables is 0.91. The amount of variance explained by higher principal components is far smaller and is already reduced in PC3, which accounts for only 3.8% of the total input variance. This component has the strongest negative correlation with the backscatter image from 07.06.2013, when river channels and sandbanks to the south of Kurungnakh were completely blocked with river ice giving high backscatter (and low PC3) and the north-eastern part of the image featured open water (evident in the Landsat image from a few days later) resulting in low backscatter (and high PC3) (Fig. 14c).

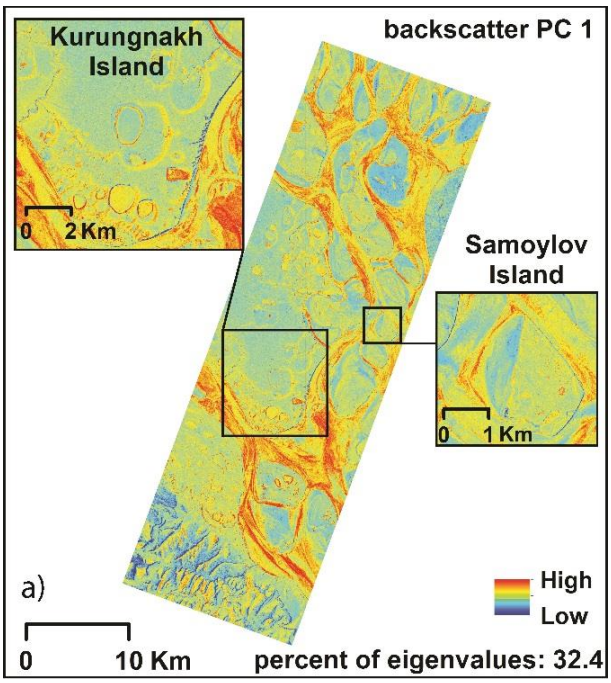
backscatter PC 1
Kurungnakh Island
0 2 Km
Samoylov Island
0 1 Km
a)
High
Low
0 10 Km
percent of eigenvalues: 32.4

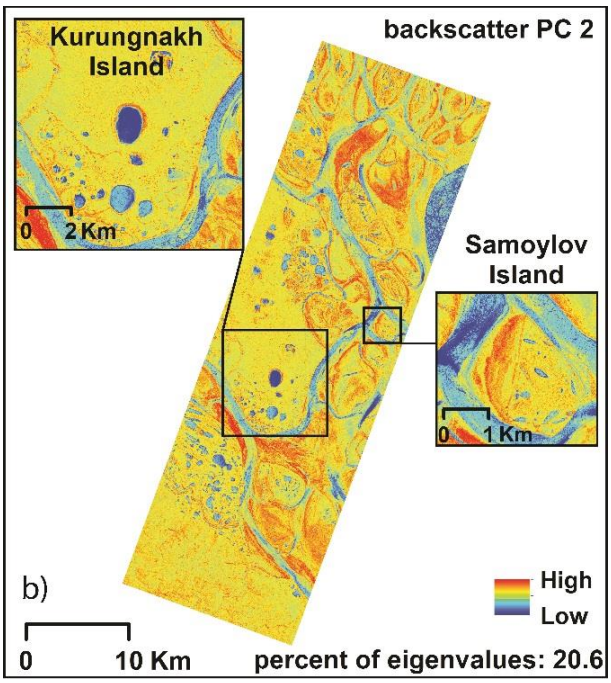
backscatter PC 2
Kurungnakh Island
0 2 Km
Samoylov Island
0 1 Km
b)
High
Low
0 10 Km
percent of eigenvalues: 20.6

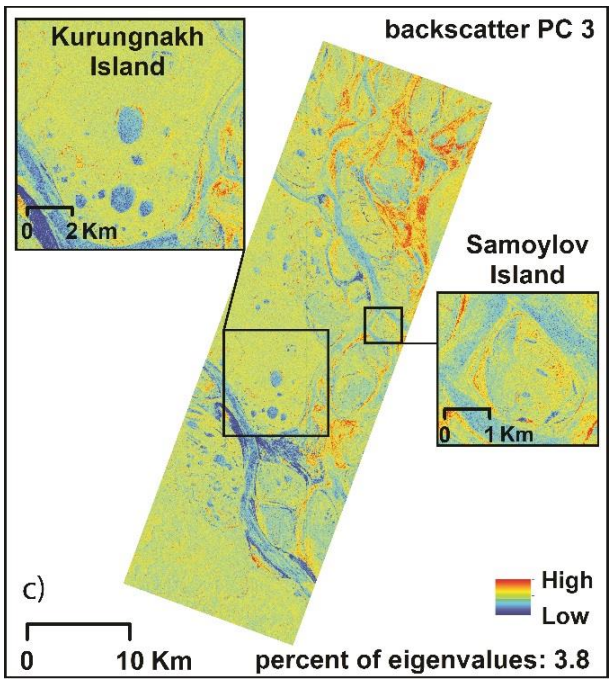

Figure 14. a)-c): first three principal components of the time series of backscatter images.

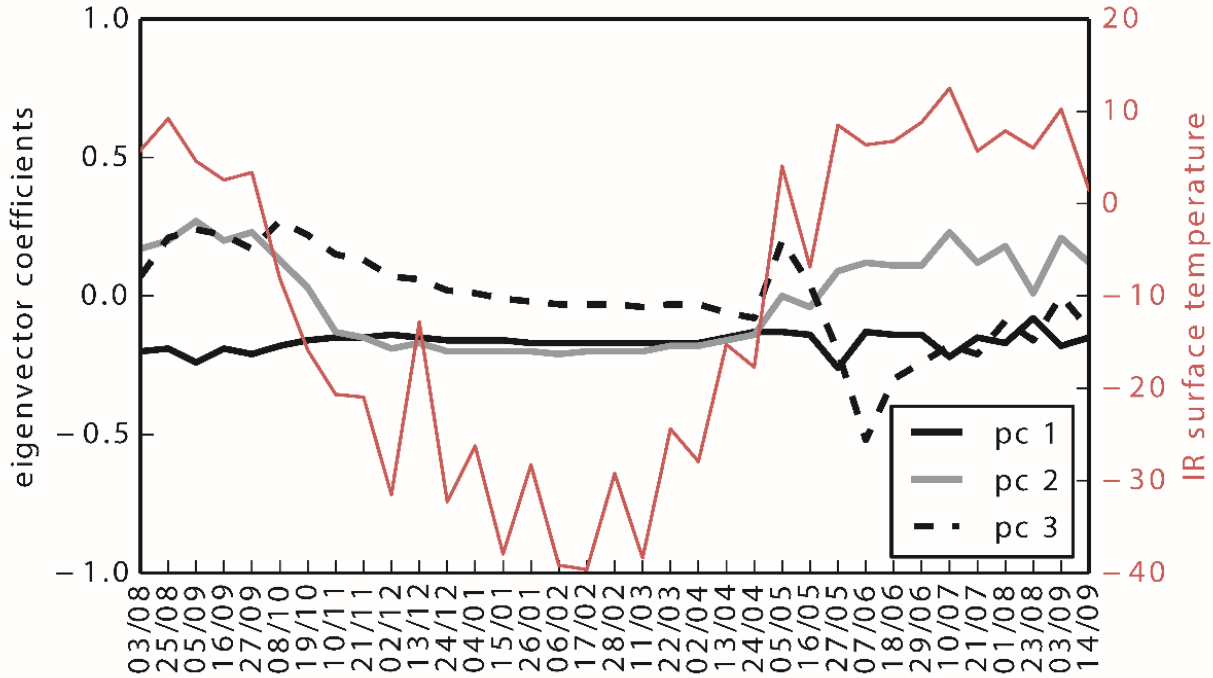

Figure 15. Eigenvectors for the first three principal components of the time series of backscatter images. Surface temperatures at 08:30 local time of every acquisition day are plotted with the red line. SAR acquisition date format: DD/MM.

2.4.3.2 PCA for the time series of coherence images

In the PCA for the time series of coherence images the PC1 accounts for 30.3% of the total input variance. It represents the dominant common coherence features in the input image stack (Fig. 16a). Three main classes of surface are clearly distinguishable: water (low PC1 values), rocky outcrops in the south (high PC1 values), and the rest of the land area (intermediate PC1 values). All eigenvector values are positive which means that the higher the coherence, the higher the PC1 (Fig. 17). The variance explained by higher principal components is already reduced in PC2 (only 9.8% of the total input variance). A clear north-south gradient is evident, with high PC2 values to the north and low PC2 values in the southern part of the image (Fig. 16b). The main contributors with negative eigenvector values are the 10.11-21.11.2012 and 21.11-02.12.2012 coherence pairs, explaining the low PC2 values in the rocky outcrop areas (high coherence in these particular images). The high positive eigenvector values of 02.04-13.04.2013 and 13.04-24.04.2013 confirm this pattern: low coherence in the southern part of these two images results in low PC2 values and high coherence in the northern part of these images results in high PC2 values.

PC3 accounts for 8.9% of the total variance. Sandbanks, parts of the rocky area, and the gullies all exhibit high PC3 values, while some of the first terrace islands (for instance the three islands to the south of Kurungnakh Island) and part of the Samoylov Island floodplain show low PC3 values (Fig. 16c). Eigenvector values for PC3 demonstrate high seasonality, with negative values corresponding to warm periods and positive values to winter. The PC3 eigenvector values during the snow-free season show a strong negative correlation with surface temperatures recorded at 08:30 local time in the middle of the 11-day period between SAR acquisitions. The correlation coefficient between these variables is -0.87.

PC4 accounts for 4.6% of the total variance. Notable contributors to this component are the 27.05-07.06.2013 and 07.06-18.06.2013 coherence pairs, whose negative eigenvector values explain the low PC4 values on the Ice Complex and parts of the first terrace areas (Fig. 16d).

The eigenvector values for all PCs from the 27.09-08.10.2012 and 24.04-05.05.2013 pairs are close to zero, indicating a lack information from highly decorrelated image pairs, which is attributed to snow cover onset and snow melt.

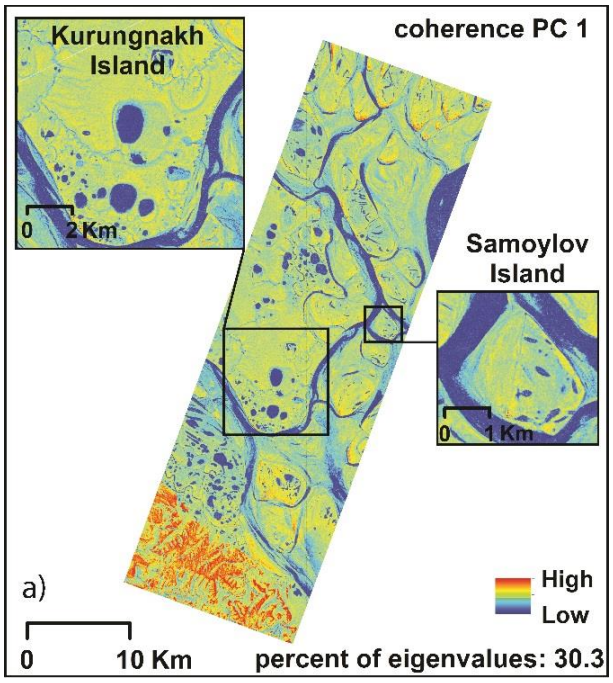

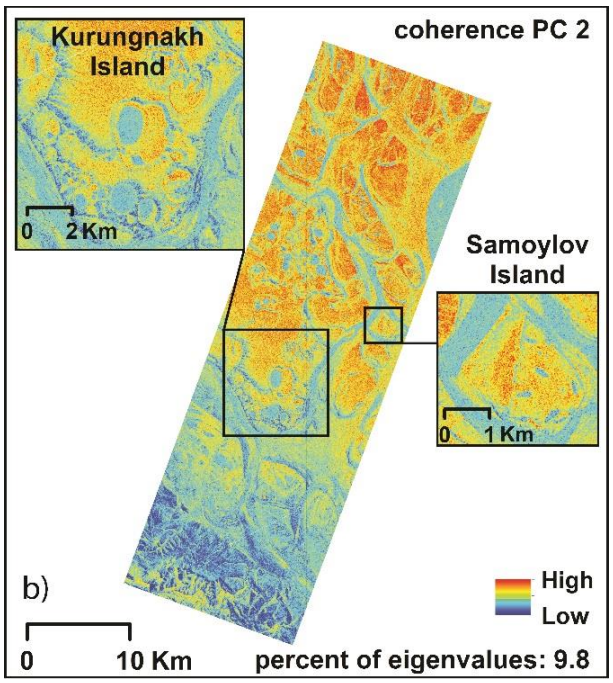

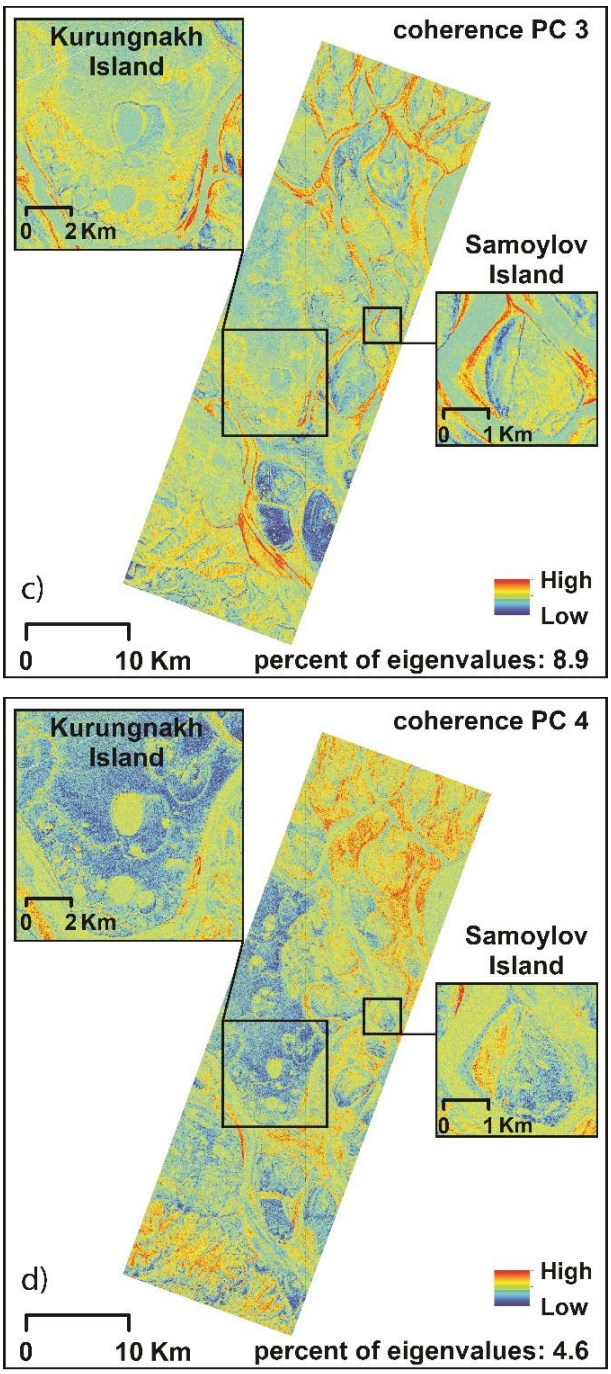

Figure 16. a)-d): first four principal components of the time series of coherence images.

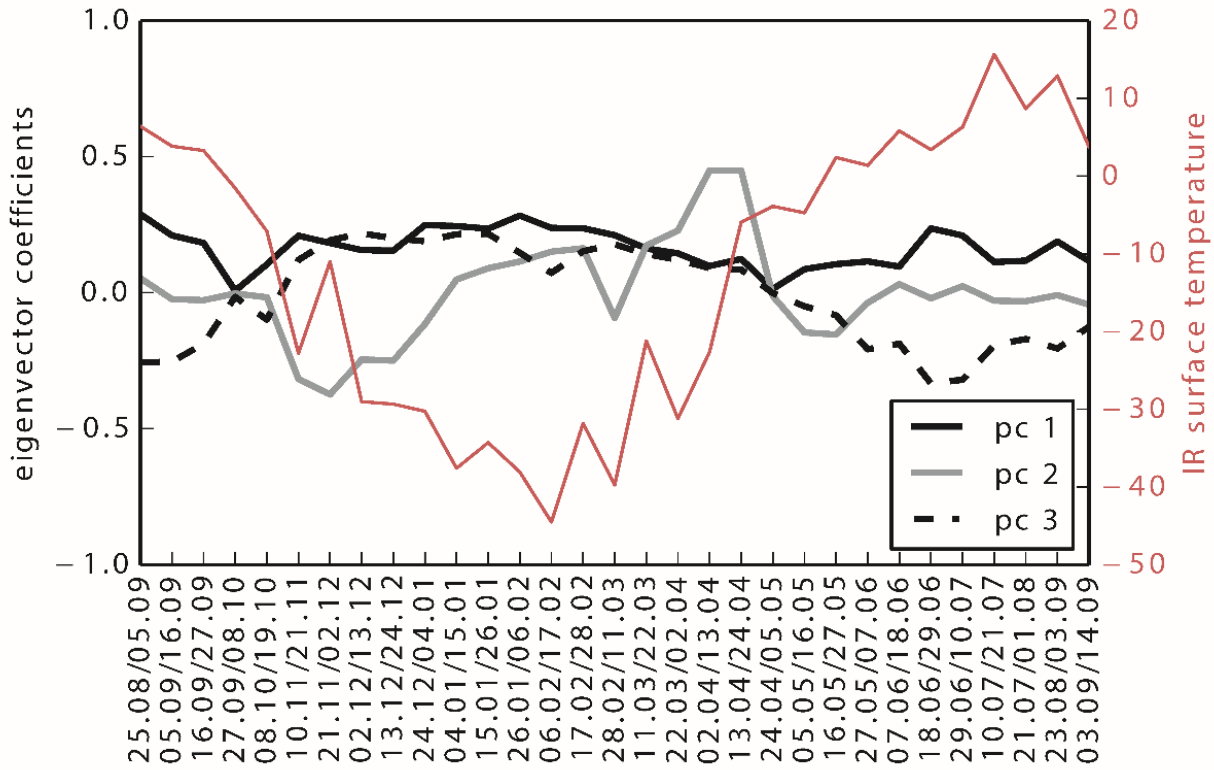

Figure 17. Eigenvectors for the first three principal components of the time series of coherence images. Surface temperatures at 08:30 of the sixth day after each acquisition (in the middle of the 11-day period between SAR acquisitions) are plotted with the red line. Coherence pairs date format: DD.MM/DD.MM.

2.5 Discussion

2.5.1 Backscatter intensity time series

Comparing backscatter time series for different ROIs revealed that most of the ROIs can be distinguished from each other by general differences in backscatter. The highest backscatter was generally from the rocky outcrops ROI and the lowest from the sandbank ROI (except of the summer of 2013), while the backscatter time series from the other (vegetated) ROIs were less clearly distinguished from each other, typically lying between the time series for the two unvegetated ROIs. Rayleigh's criterion for a rough surface is:

$$h > \frac{\lambda}{8\cos(\theta)}, \qquad (4)$$

where h is a parameter of the surface roughness (the mean vertical offset from a mean surface height), λ is the SAR wavelength and θ is the acquisition incidence angle. Using this formula we obtain h > 0.45 cm, indicating that most of the surfaces considered in our study are definitely rough in terms of TSX signal. It is likely, however, that the sandbank appears relatively smooth for the TSX signal, resulting in low backscatter during the first summer (2012) and the following winter. A probable explanation for the substantially higher sandbank backscatter (by ~6 dB) during the second summer (2013) is the presence of river ice blocks on the sandbank at the beginning of summer, followed presumably by extensive melting of the ice floes. However, whether or not similar conditions occurred during the summer of 2012 remains unknown. The rocky outcrops ROI appears to have rather rough surface and at the same time lacks the volume scattering of vegetation canopies, which may explain why it generally has the highest backscatter of all the ROIs. The vegetated surfaces yielded backscatter values that were intermediate between those of the sandbank and the rocky outcrops, indicating the significance of volume scattering and signal loss due to attenuation in vegetation canopies.

The different factors that influence the variations in backscatter (based on previous investigations and our own observations) are discussed in the following sections.

2.5.1.1 Effect of vegetation

For a microwave signal a vegetation layer can be considered to act as a heterogeneous medium in which the scattering elements are the leaves and branches. The dimensions of these elements are typically comparable to, or larger than, the wavelength of the X-band radar system. An X-band signal therefore typically does not penetrate deeply through vegetation and primary backscatter occurs from the vegetation layer. The backscatter signature depends on the dielectric properties (i.e. moisture content) of the plants and the size, shape and orientation of the backscattering elements in the vegetation layer. Volume scattering can lead to either an increase or a decrease in backscatter. There is generally a positive correlation between biomass density and backscatter up to a saturation point (dependent on the radar wavelength and acquisition parameters), after which backscatter appears to lose its sensitivity to biomass or even to develop an inverse correlation (Woodhouse, 2005).

A number of investigations have been carried out into deriving agricultural crop parameters (height, cover percentage, biomass), crop identification and classification, and crop phenology, from backscatter intensity (e.g. Le Toan et al., 1989; Brown et al., 1992; Brisco et al., 1998; Baghdadi et al., 2010). Most of the results from these investigations can not, however, be applied to tundra landscapes because the vegetation in such areas is not easily separable from the underlying soil due to presence of thick moss layers, and because it has no regular pattern or discernable stages of crop development from sowing to harvesting such as can be observed in agricultural fields.

There have been few investigations relevant to the vegetation in tundra environments. Svoray et al. (2001) investigated a variety of vegetation types (including herbaceous vegetation and dwarf shrubs) in a semiarid region of Israel and found no relationship between ERS-2 backscatter and either the Leaf Area Index (LAI) or the above-ground biomass; they did, however, find a strong negative correlation between backscatter and the derived Green Leaf Biomass Volumetric Density (GVD) index. Kasischke et al. (2003) found no relationship between ERS-2 backscatter and in situ biomass in Florida wetlands (both flooded and non-flooded), although the MIMICS theoretical model predicted a reduction in backscatter with

increasing biomass due to the attenuating effect of vegetation on C-band SAR signal. Duguay et al. (1999) analysed a one-year time series of ERS-1 backscatter over the Canadian subarctic tundra. Their willow site (representing shrubs with mean canopy height of 0.43 m) showed no sensitivity to a summer foliage appearance. Regmi et al. (2012) used TSX backscatter to investigate the ages of Alaskan thermokarst lake basins. They found a relationship between backscatter and basin age, with younger basins showing a higher backscatter than older basins, although this did not apply for modern basins less than 50 years old. Their mean late summer backscatter value for modern basins was -5.3 dB, which is significantly higher than for the basin in our study (~-13 dB) (which has approximately the same age). Using SAR polarimetry Ullmann et al. (2014) revealed that tundra vegetation showed distinct volume or mixed (volume and surface) scattering for X-band. They also demonstrated that backscatter in August and September did not vary between areas of low tundra (no shrubs, vegetation height < 20 cm) and medium tundra (< 50% dwarf shrubs, height < 50 cm) dominated by grass and herbs (-12 to -11 dB). Tundra, dominated by high shrubs (> 50% dwarf shrubs, height < 100 cm) yielded slightly higher values (0.5 dB higher). These values are in accordance with those obtained from vegetated surfaces in our own investigations (polygonal tundra, Ice Complex upland, drained lake basin and floodplain) at the same time of the year, although the differences between sites in our study are more pronounced. Duguay et al. (2015) carried out investigations in the Canadian sub-Arctic and found that TSX backscatter increased with shrub coverage only up to shrub density of 20% and showed a weak correlation with shrub height. They also showed that TSX backscatter was not affected by the characteristics of the underlying soil but increased in winter when snow was present, indicating that the TSX signal did not penetrate to the ground through the volume of vegetation and snow.

These studies indicate the difficulties that remain in relating vegetation parameters to radar backscatter, especially for shallow-penetrating X-band signal. Our investigations have revealed some consistency between summer backscatter range and the NDVI for different ROIs. The slight decreasing trend in backscatter during the summer of 2013 for vegetated ROIs may reflect processes within the vegetation layer. However, the absence of any detailed field measurements recording vegetation

parameters during the different stages of seasonal vegetation development prevented us from achieving a more thorough understand of the effect that tundra vegetation has on TSX backscatter.

2.5.1.2 Effect of the surface wetness and precipitation

The difference in dielectric constant between moist and dry soils makes it possible to use microwave remote sensing for soil moisture monitoring. Previous studies found that, for bare soils with a given roughness and texture, there was a linear relationship with a high correlation coefficient between backscatter and volumetric soil moisture (e.g. Dobson & Ulaby, 1986; Aubert et al., 2011). The presence of vegetation, however, limits the sensitivity of the SAR signal to soil moisture. Establishing empirical and theoretical models for the retrieval of soil moisture information from beneath a vegetation cover using radar backscatter data remains an important topic in active microwave remote sensing studies. The vast majority of such studies have been conducted on agricultural fields where in situ data can be obtained regularly and relatively easily (e.g. Ulaby et al., 1974; Dobson & Ulaby, 1986; Baghdadi et al., 2007). The availability of such in situ data from remote Arctic sites is very limited. The continuous layer of vegetation in the tundra (ranging in height and density from mosses to dwarf shrubs) affects SAR signals, especially in the short wavelengths of an X-band system. Some investigations have been carried out into variations in SAR backscatter due to changes in surface wetness at Arctic sites or sites with conditions similar to the tundra vegetation. Kane et al. (1996) used two ERS-1 images to compare backscatter with in situ moisture measurements in a watershed in Alaska, located in a treeless zone of continuous permafrost. Linear regression between the variables revealed R2 values of around 0.5. Lu & Meyer (2002), using ERS-1 imagery over sparsely vegetated desert areas of New Mexico, attributed significantly higher backscatter in one of the images to increased surface wetness, probably due to a rain event registered within the 24 hour period prior to image acquisition. Kasischke et al. (2009) evaluated the sensitivity of ERS-2 backscatter to in situ soil moisture and water levels over Alaskan wetlands. While combined results from sites with different vegetation conditions did not indicate any backscatter dependency on soil moisture, some individual locations featuring emergent marsh vegetation demonstrated a

linear relationship between moisture and backscatter, with a correlation coefficient of 0.74. Wall et al. (2010) analysed backscatter from two RADARSAT-1 images together with in situ surface soil moisture in the Canadian High Arctic. They found no relationship between soil moisture and backscatter for the image with extremely wet surface conditions and a weak correlation (with coefficient of 0.41) for the image with less surface wetness.

The above studies have used only a few SAR images (often only two) and none have involved detailed time series analysis, at least not for tundra conditions. Investigations into the use of X-band data for soil moisture retrieval are also limited. Sobiech et al. (2011) evaluated X-band (TSX), C-band (ENVISAT ASAR), and L-band (ALOS PALSAR) backscatter in relation to in situ soil moisture variability on Samoylov Island in the Lena Delta. The L-band data best captured the spatial distribution of soil moisture (measured on the floodplain), while X-band data did not match the soil moisture pattern at all. Ulaby et al. (1982) referred to the dominant role of volume backscatter within the vegetation layer rather than backscatter from the underlying soil for frequencies higher than 8 GHz and incidence angles greater than 30 °. This was also the case in our investigations and the lack of any backscatter response to strong rain events that occurred some time prior to the acquisition (for example, prior to 10.07.2013, see Fig. A2) seems to support this observation. It appears that only a few hours are required after the end of a rain event for the vegetation layer to become dry within the investigated environment, whereas the soil, even with increased moisture, does not contribute to the overall backscatter. However, rain that occurred a few hours before, and continued during, the acquisition on 27.09.2013 resulted in a wet vegetation layer and an increase in backscatter was consequently observed.

2.5.1.3 Effect of soil freezing and thawing

Information on the frozen or thawed state of the active layer is crucial to an understanding of permafrost-affected lands and associated processes. Fluxes of greenhouse gases and energy between soil and atmosphere, ecosystem productivity, and hydrological processes are strongly limited to, and influenced by, the short period during which the active layer is not frozen.

SAR backscatter from frozen ground and vegetation should theoretically be lower than when they are unfrozen, due to a significant reduction in the dielectric constant for frozen material, and this has been confirmed in practice using spaceborne SAR data. Rignot & Way (1994) reported a 5 dB reduction in ERS-1 backscatter in areas of tundra following freezing. Morrissey et al. (1996) observed a 3-4 dB reduction in ERS-1 backscatter for a wetland tundra in Barrow, Alaska, under freezing conditions and a reduction of up to 2 dB for non-wetland areas. Duguay et al. (1999) investigated time series of ERS-1 images to detect backscatter variations attributable to seasonal changes in a Canadian subarctic study area that was mostly underlain by permafrost. The various sites within this study area showed similar responses to freezing and thawing, with reported reductions and increases in backscatter, respectively. A shrub site showed the smallest seasonal variations, although these were still significant (a 3.5 dB decrease due to freezing and a 5.6 dB increase due to thawing), while a well-drained heath site and a sedge hummocky site demonstrated the largest seasonal variations (~8 dB decrease and increase upon freezing and thawing, respectively). Park et al. (2011) used a time series of ENVISAT ASAR (C-band) Global Monitoring mode (1 km spatial resolution) data with high temporal resolution (~ three images per week) to develop a method for detecting freeze/thaw transition dates in permafrost areas of central Yakutia, based on the lower backscatter signatures in winter.

Only limited investigations have been carried out into backscatter response to soil freezing and thawing for shorter wavelengths. Wegmüller (1990) used a ground-based scatterometer that allowed measurements to be made with multiple frequencies and incidence angles. He observed clear variations in backscatter from bare soil following day and night thaw-freeze cycles and found distinctly higher backscatter from unfrozen ground than from frozen ground for a range of frequencies (3-11 GHz) at a fixed incidence angle (50 °), and for a range of incidence angles (20 °-70 °) at a fixed frequency (7.2 GHz). Spaceborne Ku-band (wavelength 2.14 cm) scatterometers have been extensively used to develop methods for identifying the frozen or thawed state of soil on the basis of higher backscatter in winter than in summer (e.g. Frolking et al., 1999; Kimball et al., 2001; Bartsch et al., 2007). However, high winter Ku-band backscatter is more likely to be explained by

snow accumulation than by soil freezing. Sobiech et al. (2012) reported that preliminary investigations on a coarse temporally resolved TSX backscatter time series did not show any change that coincided with soil freezing or thawing in an area of tundra. Our own investigations also failed to reveal any response of TSX backscatter to the freezing or thawing of soil or vegetation. A possible explanation for this is again the shallow penetration depth of the TSX signal. Since the signal seems to be generally insensitive to the wetting of the ground (with the exception of an extreme case where precipitation occurred at the exact time of image acquisition), it is likely to be similarly insensitive to the frozen or thawed conditions in the ground, which can be considered to correspond to dry and wet conditions.

2.5.1.4 Effect of snow

The total backscatter from snow-covered land comes from four sources: scattering from the snow surface, volume scattering from within the snowpack, scattering from the interactions between the ground surface and the snow volume and scattering from the ground beneath the snow cover (Rott et al., 2010). Scattering from the surface of dry snow is negligible due to the small difference between the dielectric properties of air and dry snow. Volume scattering depends mainly on the liquid water content, snow density, grain size, and stratification. For X-band (and lower frequencies) the grain size is typically much smaller than the wavelength, rendering the contribution from volume scattering insignificant. Ulaby et al. (1977) showed that, for frequencies up to 8 GHz, backscattering from an area covered with dry snow was predominantly from the ground beneath the snow. Mätzler & Schanda (1984) demonstrated the same effect for a frequency of 10.4 GHz. Our own results, which generally show no difference in backscatter between snow-free ground and ground covered by dry snow, support the results of these previous investigations.

For wet snow cover scattering is predominantly from the air-snow boundary. For smooth (relative to the wavelength) wet snow surfaces backscatter can be lower than from dry snow. However, when the wet snow surface is rough (relative to the wavelength) backscatter can increase significantly and even be higher than the backscatter from dry snow. Mätzler & Schanda (1984) used X-band scatterometer data to investigate the properties of snow in the Alps and found an approximate 9 dB

difference between backscatter from a thin cover of dry snow (-8.3 dB) and that from wet snow (-17.4 dB). However, they found an exceptional increase in backscatter immediately after a rainfall event that presumably increased the roughness of the snow surface. Strozzi et al. (1997) found that for Ka-band (35 GHz) the backscatter from wet Alpine snow was about 10 dB lower than from dry snow. However, they also found that a refrozen crust covering the wet snow surface (caused by melting and freezing events over a short time scale) had a crucial effect on backscatter, which became even higher (by 2 dB) than the backscatter from dry snow.

In our investigations backscatter from the polygonal tundra, Ice Complex upland, drained lake, and floodplain ROIs increased by up to 3 dB on 05.05.2013. A photograph of the Samoylov Island polygonal tundra taken on this day shows patchy snow covering about 65% of the land (see Appendix, Fig. A1), with snow preserved in depressions. An analysis of air temperatures over a number of days prior to this date suggests that the area underwent multiple day-melt and night-refreeze cycles. The temperature at the time of image acquisition was below zero so we hypothesize the formation of a rough frozen crust on the snow surface (similar to that reported by Strozzi et al., 1997), which would explain the increased backscatter. Backscatter from the drained lake basin remained high on 16.05.2013 compared to the other ROIs, probably due to the concave topography favoring a longer presence of snow with a frozen crust surface (the air temperature before and during the image acquisition on this date was stable and negative).

The backscatter decreased on 13.12.2012 for four ROIs: to a lesser extent (~0.5 dB) for the polygonal tundra and the Ice Complex upland and to a greater extent (~1 dB) for the sandbank and the rocky outcrop. This corresponds to extraordinary meteorological conditions involving snowfall at the time of image acquisition and snow showers for some hours prior to the acquisition. Anomalously warm temperature at -13 °C (for typical temperatures at this time of year see Table A1 or Fig. A3 in the Appendix) is likely to have influenced the properties of the snow. Potentially such a layer of fresh snow could attenuate TSX backscatter from the ground surface, thus decreasing the overall backscatter. The snowfall that occurred on 21.11.2012 (also at the time of image acquisition) had no effect on the backscatter, indicating that the unusually warm air temperature or the intensity of the snow

showers and greater thickness of fallen snow at the time of acquisition on 13.12.2012 (10 mm, as opposed to 3 mm on 21.11) were responsible for the decrease in backscatter.

2.5.2 Coherence time series

The annual coherence cycle shows greater variability than the backscatter cycle, with marked seasonal and intraseasonal variations for all ROIs. Excluding large-baseline effects, we attribute the low coherence values to changes in the ground surface that occurred between the acquisition dates of the two images that comprise the interferometric pair. It is difficult to discuss the peculiarities of annual coherence cycles in general since there have been almost no other similar investigations into coherence time series. Wickramanayake et al. (2016) investigated time series of C-band sequential coherence images (every pair with the time span of 24 days) over forest areas, urban areas and waste rock areas in Northern Sweden. They found a seasonal variability of coherence, with the highest coherence observed in summer periods, and intermittently high values in winter periods. Absent ground truth observations, low coherence values were speculated to be attributed to seasonal environmental and anthropogenic changes (such as snowfall and snow melt or snow ploughing).

In the following we discuss those environmental factors that have the potential to affect coherence based on both previous investigations and our own observations.

2.5.2.1 Effect of snow

Strozzi et al. (1999) using ERS-1 SAR data found that snow melt resulted in a significant reduction in coherence due to the accompanying change in backscatterer geometry. This effect was confirmed in the same study by C-band ground-based radar measurements recorded at an extremely high temporal resolution. Since then there have been a few attempts to map snow-covered and snow-free areas, or wet snow and dry snow areas, using SAR coherence (Shi et al., 1997; Li et al., 2001; Kumar & Venkataraman, 2011; Wang et al., 2015).

Rott et al. (2003) identified three main reasons for temporal decorrelation in snow-covered areas, these being snow melt, snow fall, and wind-induced snow drift.

Our own investigations show a significant reduction in coherence (to ~0.2) after the first snow fall (between 27.09 and 08.10.2012) for most of the ROIs. The greatest difference between coherence values before and after snow cover onset was for the rocky outcrops, where interactions between the surface and the SAR signal largely avoid the complications due to vegetation layers. We therefore consider the rocky outcrop ROI to be an indicative surface for which temporal decorrelation is likely to be due purely to meteorological conditions.

Another marked reduction in coherence occurred due to spring snow melt, which took place after 24.04.2013 in all of the ROIs except for the sandbank ROI, where snow melt started at least one month earlier (by 23.03.2013), and the rocky outcrops ROI where the snow melt had started by 08.04.2013, at the latest (based on Landsat imagery, see Fig. 12).

A reduction in coherence, occurred in December for the sandbank and rocky outcrops ROIs (the coherence for the vegetated ROIs had been similarly low prior to that time), coincided with a reduction in backscatter on 13.12.2012, discussed in the subsection 6.1.4. We assume, in accordance with Rott et al. (2003), that the relatively thick layer of fresh snow (which likely had different properties due to the much warmer condition) changed the nature of the scattering elements, causing the observed reduction in coherence.

We were not able to attribute other variations in coherence over the rocky outcrops during the winter to any particular snowfall or wind conditions. It should however be borne in mind that our meteorological data were acquired some 25 km away from the rocky outcrop site and in a different topographic setting, and that processes (such as, for example, snow metamorphism) may not be directly reflected in the meteorological parameters but may still have influenced the coherence.

2.5.2.2 Effect of vegetation

Where there is a vegetation layer present the decorrelation consists mainly of volumetric decorrelation due to volume scattering within the vegetation, and temporal decorrelation due to dislocation of the scatterers. Such dislocations can be caused by wind on a very short time scale, or by vegetation growth or decline over a longer time scale.

A number of investigations have been conducted into the use of coherence for land cover classification (Wegmüller & Werner, 1996; Weydahl, 2001b; Hall-Atkinson & Smith, 2001), and to derive parameters for crops or farming activities (Wegmüller & Werner, 1997; Engdahl et al., 2001; Blaes & Defourny, 2003). Tall dense vegetation leads to larger decorrelation than low sparse vegetation over the same time span, making a classification possible. Monitoring of crop parameters is based on the reduction in coherence due to plant growth. However, this method is highly sensitive to the time span between images used to form a coherence pair, and to the wavelength of the sensor. Same-day tandem ERS acquisitions were therefore often used to form coherence datasets in these investigations.

In our investigations we explored a time series of coherence data with 11 days between acquisitions. The coherence during the summer of 2013 was generally lower than over the winter. This may be due to the susceptibility of the vegetation to wind during the summer, in contrast to winter when it is under snow cover. Analysis of wind data did not reveal any relationship between the coherence in summer and the wind speed, but the extent to which our measured wind speeds really reflect the intensity of movement within the vegetation is open to speculation.

The highly vegetated drained lake basin yielded lower coherence values than the less vegetated polygonal tundra, and the sparsely vegetated rocky outcrops ROI yielded higher coherence values than the vegetated ROIs. This all agrees well with the expected behavior of coherence, with higher biomass leading to a stronger decorrelation. Vegetation growth did not appear to influence the coherence in our investigations – in fact, the coherence increased during the typical growth period of the tundra that occurs in June.

2.5.2.3 Effect of soil wetness variations

Nesti et al. (1995) conducted an experiment involving moistening a sand sample and measuring the microwave signal (2-12 GHz) phase shift due to the increased moisture; they found a well correlated signal despite the change in moisture. Engdahl et al. (2001) and Blaes & Defourny (2003) also noted only limited influence of soil moisture on coherence. In contrast, other studies have tried to attribute low coherence to soil moisture variations, although only qualitatively and with no ground

truthing (Weydahl, 2001b; Zhang et al., 2008). Luo et al. (2001) developed a model for investigating the effects of roughness and soil moisture on the coherence of bare soils. They found that only large soil moisture variations are likely to result in significant signal decorrelation, and that minor changes in soil moisture did not lead to decorrelation even though variations in backscatter could be observed. Barrett et al. (2012) confirmed this finding by assessing the viability of C-band and L-band coherence for soil moisture retrieval. They reported a poor relationship between these variables but also noted that a significant change in moisture did appear to affect the coherence.

Our investigations have not shown any clear evidence of decorrelation due to precipitation. As discussed in the section on backscatter variation, the TSX signal likely does not penetrate very deeply through the vegetation layer but rather interacts with it. We found that even a strong precipitation event does not influence the backscatter in long term, except when rain is actually falling at the time of image acquisition (such as on 27.09.2012). The coherence, however, showed no significant decrease over most of the ROIs for the 16.09-27.09.2012 pair, and the 27.09-08.10.2013 pair was decorrelated due to snow cover onset.

2.5.2.4 Effect of soil freezing and thawing

As is the case with variations in soil moisture, freezing and thawing change the dielectric properties of the media but not the geometry of the scatterer. Freezing and thawing are therefore not expected to affect the coherence. Borgeaud & Wegmüller (1996) reported high coherence (> 0.7) for an ERS tandem pair in spite of a freezing event, while the backscatter decreased significantly.

Our investigations were unable to detect either a reduction or stability in coherence due to soil freezing because the freezing occurred at the same time as the onset of snow cover (between 27.09 and 08.10.2012, based on the automated soil temperature measurements from a depth of 2 cm on Samoylov Island - data not included), which dominated the loss of coherence. Thawing of the soil (based on the same soil temperature data) occurred between 07.06 and 18.06.2013, which is later by more than a month than the onset of snow melt and the coherence value for the

polygonal tundra ROI from the 07.06-18.06.2013 pair was higher than most of the other coherence values during the summer of 2013.

2.5.2.5 Flood

Inundation can generally be relatively easily identified by low backscatter values due to specular reflection of the SAR signal from the open water (e.g. Ramsey III, 1995; Kasischke et al., 2003). However, even light wind conditions during image acquisition can cause roughness on the water surface and a consequent increase in backscatter, which may impose limitations on the use of SAR backscatter for inundation detection and mapping. Using the interferometric coherence helps to overcome this problem as coherence values always remain low over water bodies. This approach has been used for flood monitoring by, for example, Dellepiane et al. (2000), Nico et al. (2000) and Pierdicca et al. (2014).

Although our investigations yielded low coherence values (~0.2) for the sandbank during the flood on 27.05.2013, the previous and subsequent coherence values were also low. These low coherence values before the flood are attributed to snow melt, and those after the flood to the presence (and melting) of river ice floes accumulated on the sandbank. Coherence alone is therefore not always useful for flood detection, and synergetic use of different types of data (in our case SAR backscatter and optical data) may yield more reliable results.

2.5.3 PCA of backscatter and coherence image time series

PCA for SAR backscatter time series has been used by a few authors for soil moisture assessment. For example, Verhoest et al. (1998) used four ERS-1/2 tandem pairs to show that their PC2 image featured similarities to the drainage map of a catchment area in Belgium, from which they concluded that the PC2 of backscatter time series could be used to detect seasonal variations in soil moisture patterns. Bourgeau-Chavez et al. (2005) used PCA on a time series of 14 ERS backscatter images over a period of two years to evaluate surface changes related to hydrology in the Florida wetlands. Their PC1 was attributed to the areas featuring the most stable backscatter over time. The loadings for the PC2 correlated strongly with the total monthly rainfall, indicating a relationship between the PC2 and the hydroperiod. Kong &

Dorling (2008) applied PCA to a time series of 12 ENVISAT ASAR backscatter images and found that the PC2 values were inversely correlated (R^2 = -0.67) with temporal soil moisture variations inferred using the MOSES model.

In our study PCA provided a good spatial overview of the essential information contained within the multiple time slices. It was possible to track the main time slices contributing to the individual principal components. The PC1 for both time series showed the most common features of the contributing images: for the backscatter time series high and low PC1 values corresponded to low and high backscatter values, respectively, while for the coherence time series high and low PC1 values corresponded to high and low coherence values, respectively. A comparison of the PC1 with means of the temporal stacks showed strong agreement suggesting that the PC1 represents the mean of each time series. The PC1 of the coherence images seems to be more suitable for classification purposes than the PC1 of the backscatter images. The most distinct surface classes mapped were (i) water bodies (lakes and river), (ii) rocky outcrops, and (iii) the remaining land surfaces (Fig. 16a). The PC1 of the backscatter was contaminated by effects such as the presence or absence of lake ice and shadow/layover in the rocky outcrops region.

Anomalies in seasonal patterns were demonstrated by the higher PCs. The PC2 of the backscatter time series accounted for 20.6% of the variance and delineated water bodies. Analysis of the PC2 eigenvector revealed a positive correlation between backscatter input and PC2 during both summer periods (low backscatter from water bodies corresponded to low PC2 values) and a negative correlation during the winter (high backscatter from ice-covered water bodies corresponded to low PC2 values). The PC3 of backscatter accounted for only 3.8% of the variance in the dataset and represented the spatial variance in river ice conditions during spring that was evident from the Landsat imagery (not shown). The PC2 of coherence, which accounted for 9.8% of the variance in the coherence image stack, represented the spatially variable snow conditions in spring (snow melt to the south and stable snow cover to the north) evident from the Landsat imagery (not shown).

Of particular note was the high correlation coefficient (0.91) between the PC2 eigenvector of the backscatter and the surface temperature recorded close to the time of acquisition, indicating a latent relationship between surface temperature and

backscatter; a direct comparison of these variables does not show any correlation. The eigenvector for PC3 of the coherence time series also revealed a relationship with surface temperature, with a correlation coefficient of -0.87. A direct comparison of coherence with surface temperature also revealed a fairly high inverse correlation, with a correlation coefficient of -0.6 for the rocky outcrops, the polygonal tundra and the sandbank, and of -0.7 for the drained lake basin. These relationships between temperature and both backscatter and coherence PCs eigenvectors are mainly evident during the warmer time of year, i.e. when the ground is not snow covered (Figs. 15 and 17).

We also compared the temporal precipitation pattern with all of the PC eigenvectors in order to detect any latent relationships between surface moisture and backscatter or coherence, based on the results of the previous investigations mentioned earlier in this section. A possible problem is the insensitivity of the X-band signal to precipitation even if it occurs only a few hours before SAR acquisition, as shown in the backscatter time series for the ROIs. We therefore only calculated daily precipitation totals for the TSX acquisition dates, but a comparison with the PC eigenvectors still failed to reveal any correlation.

We therefore have to leave open at this stage the question of which processes could be behind the marked correlation between surface temperature and both the backscatter and coherence variations in warm periods (as revealed by their PC2 and PC3 eigenvectors, respectively). We also have to leave open the question of whether or not these relationships are specific to our study area, the acquisition parameters, and the particular time period investigated.

Possible associated processes could, at least in theory, range from atmospheric processes through to ground processes. Atmospheric processes could include morning fog (since the TSX acquisition was at 08:34 local time) or cloud cover, both of which could affect surface temperatures and surface moisture levels (for instance, through rime and dew), near-surface air turbulences or stability related to temperatures or temperature gradients (also affecting vegetation movement), and incoming and outgoing radiation levels, while relevant ground processes could be a result of, for example, higher temperatures leading to lower surface humidity through increased evaporation, or an opposite effect with increased evaporation (e.g.

through lower air humidity or more wind) leading to cooler surface temperatures. The processes involved need not necessarily be active at the time of acquisition, but could, for example, act over some hours (e.g. the previous night) or even several days. A first step to answering these questions would be to investigate other time series for the same area but over different years, or other time series for different areas.

2.6 Conclusions

Time series of X-band SAR backscatter intensity and 11-days interferometric coherence with high temporal resolutions have been used to interpret major seasonal land surface changes in a variety of tundra environments, namely an area of wet polygonal tundra, a drier Ice Complex upland area, a recently drained well-vegetated lake basin, a partly well-vegetated floodplain, a bare sandbank, and a very dry area of rocky outcrops. Seasonal variations in intensity and coherence were evaluated in the context of meteorological conditions such as air and land surface temperatures, as well as precipitation and snow cover status. The TSX signal appeared to have very limited penetration through vegetation and the observed variations in backscatter and coherence were therefore mainly attributed to processes in the upper layer of vegetation. Variations in the TSX backscatter intensities were mostly moderate throughout the annual cycle. Backscatter was found to be insensitive to ground freezing and thawing as well as being generally insensitive to precipitation, but it was sensitive to (i) an individual rain event at the time of SAR acquisition, (ii) an individual snow shower coinciding with unusually high air temperature, and (iii) the spring melt of the snowpack (likely with a refrozen icy crust on the surface). Flooding of the sandbank was clearly detectable from extremely low backscatter values. The selected ROIs demonstrated generally good separability on the basis of differences in their backscatter intensities: rough and very sparsely vegetated rocky outcrops yielded the highest backscatter and the smooth barren sandbank yielded the lowest backscatter. The backscatter from the vegetated ROIs yielding intermediate values, with the less vegetated ROIs returning lower backscatter.

Interferometric coherence comprises both amplitude and phase signal components and should therefore be more sensitive to surface changes than backscatter intensity

alone, especially at the X-band frequency, an assumption that is strongly supported by the results of our investigations. The coherence decreased dramatically with the onset of snow cover in all of the landscape types. The snow melt period was also clearly identified by another reduction in coherence. The snow shower that affected the backscatter also caused a reduction in coherence. January and February yielded the highest coherence values for all of the ROIs (with mean values of up to 0.9 for the rocky outcrops).

Our PC analysis demonstrated a clear discrimination of major landscape elements and thus a good potential for spatio-temporal land surface classification in a tundra environment based on SAR time series. Many spatial features revealed by the principle components of the backscatter and coherence time stacks showed a more or less clear relationship with spatial and seasonal variations in the land cover. Eigenvectors of some PCs were very highly correlated with surface temperatures, with a correlation coefficient of 0.91 for the PC2 eigenvector of the backscatter time series and -0.87 for the PC3 eigenvector of the coherence time series. The results indicate a latent relationship between backscatter and surface temperature, which was not observed by direct comparison. Direct comparison of coherence with surface temperature, however, yielded a fairly high correlation (correlation coefficient around -0.6 for most of the ROIs). Further research is required to investigate the possible processes influencing the correlations between surface temperature and backscatter or coherence, as well as investigating how unique these correlations are to our study area and acquisition parameters, or the time frame of the study. A number of indirect processes acting in the atmosphere or on the ground (or coupled) appear at a first glance to be possible, while direct links between surface temperature and backscatter or coherence appear physically unlikely.

The interferometric coherence levels recorded in this study could possibly allow to conduct differential interferometry in order to detect seasonal vertical ground movements associated with the freezing and thawing of the active layer, but this was not the focus of these investigations. The regions of interest (for instance, Ice Complex) yielded moderate coherence (up to 0.5) in some 11-days pairs over the relevant periods, but analysis of continuous interferometric time series would not be possible due to the unacceptably low coherence of some of the other pairs.

Ground truth data in particular, together with detailed meteorological observations and ground status information from a time-lapse camera, were of utmost importance in our study. For instance, without a detailed knowledge of the day and night air temperatures and the photographs from Samoylov Island it would have been impossible to infer a refrozen crust on the snowpack surface and hence to explain the increase in backscatter following the beginning of snow melt. Further detailed analysis of, for example, the vegetation (size of leaves, vegetation height, coverage, moisture, etc.) or the snowpack (density, structure, moisture, etc.) would be likely to assist in providing additional explanations for variations in backscatter and coherence. Extending our analysis to future TSX time series will be critical for verification of the presented results.

Acknowledgements

We thank the editor, Prof. Dr. Eric Kasischke, and the referees for their thoughtful and valuable comments. Special thanks go to the German Aerospace Center DLR and Achim Roth for invaluable help with the data access. We also thank Prof. Dr. Claude Duguay and Dr. Sebastian Westermann for valuable discussions. Parts of the study were conducted in preparation for the ESA GlobPermafrost project. A. Kääb acknowledges support by the European Research Council under the European Union's Seventh Framework Programme (FP/2007–2013)/ERC grant agreement no. 320816, and the Research Council of Norway through RASTAR, grant no. 208013. We are grateful for the support of the research station "Samoylov Island", the logistic support of Waldemar Schneider, and assistance in the field from Niko Bornemann.
This study has been conducted with the support of the Helmholtz Alliance HA310 'Remote Sensing and Earth System Dynamics'.

3

Monitoring Bedfast Ice and Ice Phenology in Lakes of the Lena River Delta Using TerraSAR-X Backscatter and Coherence Time Series

Abstract

Thermokarst lakes and ponds are major elements of permafrost landscapes, occupying up to 40% of the land area in some Arctic regions. Shallow lakes freeze to the bed, thus preventing permafrost thaw underneath them and limiting the length of the period with greenhouse gas production in the unfrozen lake sediments. Radar remote sensing permits to distinguish lakes with bedfast ice due to the difference in backscatter intensities from bedfast and floating ice. This study investigates the potential of a unique time series of three-year repeat-pass TerraSAR-X (TSX) imagery with high temporal (11 days) and spatial (10 m) resolution for monitoring bedfast ice as well as ice phenology of lakes in the zone of continuous permafrost in the Lena River Delta, Siberia. TSX backscatter intensity is shown to be an excellent tool for monitoring floating versus bedfast lake ice as well as ice phenology. TSX-derived timing of ice grounding and the ice growth model CLIMo are used to retrieve the ice thicknesses of the bedfast ice at points where in situ ice thickness measurements were available. Comparison shows good agreement in the year of field measurements. Additionally, for the first time, an 11-day sequential interferometric coherence time series is analysed as a supplementary approach for the bedfast ice monitoring. The coherence time series detects most of the ice grounding as well as

spring snow/ice melt onset. Overall, the results show the great value of TSX time series for monitoring Arctic lake ice and provide a basis for various applications: for instance, derivation of shallow lakes bathymetry, evaluation of winter water resources and locating fish winter habitat as well as estimation of taliks extent in permafrost.

3.1 Introduction

Thermokarst lakes and ponds are abundant and characteristic landscape features of the Arctic lowland permafrost regions on both the Eurasian and North American continents. Estimates of their areal coverage span a wide range and are scale dependent (Lafleur et al., 1997; Pienitz et al., 2008; Grosse et al., 2013), but all agree that they can occupy a significant proportion of the land area in high latitude regions (up to 40% in some areas (Grosse et al., 2013)). Arctic water bodies play a crucial role in land-atmosphere exchanges of greenhouses gases and energy fluxes (Zimov et al., 1997; Rouse et al., 2005; Brown and Duguay, 2010; Langer et al., 2011b), making them highly important for global climate change science. The seasonal ice cover can reach thicknesses of up to 2 m over an ice season of up to 8–9 months which alters greenhouse gas fluxes, as well as biological productivity within these water bodies. The ice-cover duration is also an important indicator of climate variability and knowledge of lake ice phenology from freeze onset to water-clear-of-ice is important in particular for regional climate change assessments (Lenormand et al., 2002; Duguay et al., 2006).

Shallow water bodies which have depths of less than the maximum ice thickness eventually experience grounding to the bottom (i.e., bedfast ice) during the winter time. After ice grounding, such water bodies significantly decrease their contribution to energy and gas fluxes as the biological activity is suppressed within the frozen sediments (Jeffries et al., 1999; Langer et al., 2015). Deeper water bodies where unfrozen water remains beneath the ice cover during the entire winter period favor the development of a talik (permanently unfrozen inclusion within permafrost). Therefore, distinguishing grounded from floating ice areas in high latitude lakes is essential for permafrost science from physical, chemical and biological aspects. Changes in lake ice regime from a floating to a grounded state and vice versa, due to

water level change or ice thickness variations, can also be used as an indicator of climate variability (Arp et al., 2012; Surdu et al., 2014). Variations in the fraction of ice that freezes to bed can also be a result of lake drainage or lake expansion indicating landscape transformations caused by local impacts of climate change (Arp et al., 2011).

Monitoring lake ice phenology and the fraction of bedfast ice using ground observations is not possible on a regular basis and over larger areas in remote Arctic territories. Remote sensing can provide frequent and spatially representative information on the ice regime of Arctic lakes. Optical remote sensing in the Arctic is limited due to polar night and often persistent cloud cover (e.g. Latifovic and Pouliot, 2007; Weber et al., 2016). Active microwave radar signals, on the other hand, penetrate through cloud cover and allow for systematic monitoring of lake ice phenology (Hall et al., 1994; Howell et al., 2009; Cook and Bradley, 2010; Surdu et al., 2015). Moreover, the difference in radar backscatter intensities between grounded (bedfast) and floating lake ice allows for mapping of these areas and estimation of the timing of grounding. The application of radar technology for this purpose began in the 1970s when airborne radar systems were used to acquire images over Alaskan lakes (Elachi et al., 1976; Weeks et al., 1977, 1978). These early studies were limited to the visual (qualitative) interpretation of imagery since no calibrated digital data were available. In the new era of spaceborne Synthetic Aperture Radar (SAR) in the 1990s, a number of studies utilized calibrated ERS-1 data (C-band) and the quantitative analysis of backscatter intensity for different periods during ice growth (Jeffries et al., 1994; Morris et al., 1995; Jeffries et al., 1996). However, the relatively low spatial resolution of SAR data used in these studies (240 m pixel size) confined the analysis to relatively large lakes, omitting the abundant number of water bodies smaller than the resolution. Advancements in technology have allowed for lake ice studies using higher spatial resolution (100 m or better) data from C-band RADARSAT-1, ERS-1 and ENVISAT ASAR (Duguay et al., 2002; Duguay and Lafleur 2003; Hirose et al., 2008; Arp et al., 2012; Surdu et al., 2014). One of the main constraints for SAR-based investigations to date has been the insufficient temporal resolution of time series, so that acquisitions obtained with different incidence angles or a multi-sensor approach must be employed (Duguay et

al., 2002; Surdu et al., 2015). Monitoring lake ice conditions using X-band SAR data has mostly been limited to the early airborne studies mentioned above. The potential of data from new generation X-band SAR, such as TSX with its spatial resolution up to 3 m, is far from fully investigated. Using a single high-resolution Spotlight TSX image, Jones et al. (2013) showed its excellent suitability for distinguishing bedfast from floating lake ice. Sobiech and Dirking (2013) used TSX imagery for the classification of ice and open water fractions during the ice decay period in lakes of the Lena River Delta. To our best knowledge, the latter study is also the only example of SAR-based investigation of lake ice conditions in the Siberian Arctic.

SAR-derived timing of ice grounding in combination with bathymetry information can be used as a proxy for the estimation of ice growth (Duguay and Lafleur, 2003; Hirose et al., 2008). Another approach is to use a numerical ice growth model: SAR-derived date of ice grounding can be assigned to a simulated ice thickness on that date, which, in turn, provides information on the depth of a lake (i.e., bathymetry) (Jeffries et al., 1996; Kozlenko and Jeffries, 2000).

In this study, we investigate the potential of high temporal resolution (11-day) TSX backscatter intensity time series for monitoring ice phenology and ice grounding during three years on lakes in the Lena River Delta, Siberia. In addition, for the first time, we produce a sequential interferometric coherence time series for detection of ice grounding and compare it to the backscatter intensity time series. Using TSX-derived timing of ice grounding and the numerical lake ice model CLIMo, we retrieve the thickness of bedfast ice and evaluate the results against in situ measured ice thicknesses.

3.2 Background on SAR Response to Lake Ice

3.2.1 Ice Grounding

Interactions between radar and ice cover are strongly dependent on backscattering interfaces (e.g. Gunn et al., 2015a). In the case of floating ice, there is a strong dielectric contrast between ice and the water beneath: the real component of the relative dielectric permittivity of fresh water at 0 °C for X-band frequencies is ~43 (e.g. Kaatze and Uhlendorf, 1981) and that of freshwater ice is ~3 (Vant et al., 1974).

This large dielectric contrast causes a strong reflectance of the radar signal from the ice–water interface. Using polarimetric analysis, recent studies have demonstrated that the single bounce at this interface is the main mechanism of backscattering from the floating ice (Engram et al., 2013; Atwood et al., 2015). Thus, backscatter intensity in the case of floating ice is mostly controlled by roughness at the ice–water interface. In the case of grounded ice, there is no sharp dielectric contrast between the ice and the frozen sediments as the relative permittivity for frozen silt and clay is ~3–6 (Hoekstra and Delaney, 1974). Absence of the dielectric contrast leads to a strong signal absorption into the frozen sediments causing much lower backscatter intensity compared to floating ice. Thus, the rapid decrease of backscatter intensity during wintertime can indicate the change from floating ice to grounded ice conditions. Various studies have documented the magnitude of the drop in backscatter intensity with ice grounding at different radar frequencies (Table 3). The variations in the magnitude of backscatter drop between different studies are likely associated with sensor settings (frequency, incidence angle, polarization) as well as regional settings (composition and structure of lake sediments, frozen/unfrozen condition of sediments or wetness of sediments).

Table 3. Magnitude of the drop in backscatter intensity with ice grounding documented in different studies.

Reference	Study Area	Sensor	Polarization	Incidence Angle	Magnitude of Drop in Backscatter from Floating to Grounded Ice (in dB)
Jeffries et al., 1994	Alaska North Slope	ERS-1 (C-band)	VV	20.1–25.9 °	10–12
Morris et al., 1995	Alaska North Slope, Yukon Delta, Bristol Bay	ERS-1 (C-band)	VV	20.1–25.9 °	4.8–8.8 (sub-Arctic lakes) 7.8–11.8 (Arctic lakes)
Duguay et al., 2002	Churchill, Manitoba	RADARSAT-1 (C-band)	HH	20–49 °	6
Brown et al., 2010	Sagavanirktok River delta, Alaska	ASAR AP (C-band)	HH, VV	19.2–31.4 °	threshold: –10 *
			HV, VH		threshold: –19
Engram et al., 2013	northern Seward Peninsula, Arctic Coastal Plain	ALOS PALSAR, JERS-1 (L-band)	HH	24–40 °	3–6
		ERS-1,-2 (C-band)	VV	23 °	8–9
Jones et al., 2013	Arctic Coastal Plain	TSX (X-band)	HH	46 °	threshold: –12.3
Gunn et al., 2015b	Churchill, Manitoba	Field-based scatterometer (X- & Ku-band)	VV, VH	39–45 °	2–4

* In case a time series was not present in the study, a fixed threshold value set to differentiate floating from grounded ice is indicated.

Repeat-pass SAR interferometry (InSAR) employs the phase of the radar signal to detect surface displacements. It calculates the phase difference between two SAR images covering the same area at different times. Usage of InSAR can be strongly limited due to insufficient phase coherence between two SAR images. Potential reasons for a loss of phase coherence include thermal noise from the antenna, a large interferometric baseline, topographic effects, misregistration between the SAR images, atmospheric effects, as well as surface changes that occur between SAR acquisitions (Zebker and Villasenor, 1992). In case of lake ice, such surface change is defined by the continuously evolving ice–water interface, with ice growth changing the backscattering interface at each SAR acquisition. Therefore, for floating ice the coherence is expected to be constantly low because the ice–water interface is never the same over the entire winter period. However, once the ice becomes grounded, the backscattering interface does not change significantly (depending largely on the freezing front expanding into the sediments), causing potentially an increase in

coherence. Thus, we expect an increase in coherence to be a good indicator of ice grounding, in addition to the decrease in backscatter.

3.2.2 Ice Phenology

Monitoring ice phenology using SAR backscatter is possible by associating backscatter variations to changes in the backscattering potential of the ice medium. Initial freeze-up (or ice-on) is characterized by low backscatter due to specular reflection from a thin and smooth undeveloped ice cover. At the beginning of ice formation, C-band backscatter intensity values for thin, smooth ice have been reported to range from −22 to −16 dB (ERS-1, VV) (Jeffries et al., 1994), −16 to −13 dB (RADARSAT-1, HH) (Duguay et al., 2002) and −15.9 dB to −4.8 dB (ASAR, HH) and −17.4 dB to −11.7 dB (RADARSAT-2, HH) (Surdu et al., 2015). However, it can be difficult to detect initial ice formation due to similarly low backscatter of newly formed ice and open water under calm wind conditions. The potential presence of cracks and ridges in the ice, which appear as bright linear features contrasting against the surrounding dark lake surface, can support the detection of early freeze-up (e.g. Morris et al., 1995). Ancillary data, such as air temperature observations from nearby meteorological stations, can also help with freeze-up detection.

Ice growth (thickening) is marked by an increase in backscatter up to a saturation point after which the backscatter remains relatively stable until melt onset (if the ice has not grounded). We designate this period of stable backscatter as a “stable stage”. Jeffries et al. (1994) and Morris et al. (1995) report backscatter values between −6 dB and −7 dB (ERS-1 VV, 20.1 °–25.9 ° incidence angle) and Duguay et al. (2002) report values from −9 to 2 dB (RADARSAT-1, HH, 20 °–27 ° incidence angle) for floating ice during the stable stage. Howell et al. (2009) state a difference of 6 dB between the stable stage and freeze onset for QuikSCAT (Ku-band, HH, 46° incidence angle) time series of Great Bear and Great Slave lakes (Canada). Threshold values of the same order of magnitude are given in Surdu et al. (2015) for ASAR (HH, 15 °–42 ° incidence angle) (5.5 dB) and RADARSAT-2 (HH, 20 °–46 ° incidence angle) (6.5 dB) time series.

Melt onset is characterized by a significant alteration of backscatter intensity compared to the stable stage. Generally, melt onset begins with snow melt on the top

of the ice cover (if snow is present). Therefore, backscatter variations during melt onset depend mainly on snow cover properties. Wet snow typically causes high absorption of a SAR signal and consequently a significantly reduced backscatter intensity. Additionally, water ponding on the ice surface can reduce backscatter intensity due to specular reflection of the radar signal away from the ponding surface. However, when the snow cover melts and refreezes due to day and night air temperature variations around 0 °C, the backscatter intensity can increase due to increased roughness on the snow cover surface. Jeffries et al. (1994) observe both ERS-1 backscatter decrease and increase of 10 dB for different locations during the melt period. Duguay et al. (2002) report RADARSAT-1 backscatter intensity as low as −21 to −12 dB for the melt period. Howell et al. (2009) observe a pronounced decrease in Ku-band backscatter with melt onset and found a difference of 4 dB between the stable stage and melt onset. Geldsetzer et al. (2010) report RADARSAT-2 (HH) backscatter values of about −21 dB from lake ice following melt onset. Surdu et al. (2015) indicate backscatter values ranging from −20.4 to −15.7 dB (ASAR) and from −22.9 to −16.1 dB (RADARSAT-2) at the beginning of break up period.

Water clear of ice (or ice-off), which corresponds to the date when the water body becomes totally ice free at the end of break-up period, can be easily identified by low backscatter values under calm wind conditions due to specular reflection of the radar signal away from the water surface. However, under windy conditions, the roughened water surface causes high backscatter, so that the detection of water clear of ice becomes difficult. Howell et al. (2009) observe a difference of 10 dB between the stable stage and water clear of ice from QuikSCAT Ku-band scatterometer time series, while Surdu et al. (2015) report a difference of 7.5 dB for ASAR and 8.5 dB for RADARSAT-2.

3.3 Study Area

The Lena River Delta (73 °N; 126 °E) in Siberia occupies an area of about 30,000 km² and is located in the zone of continuous permafrost that reaches depths of up to 600 m (Grigoriev, 1960). The region belongs to the typical Arctic tundra ecozone. Water bodies of different size cover about 20% of the delta's land area (Muster et al., 2012). The climate of the Lena River Delta area is characterized by extremely cold, long winters and short, cool summers. Boike et al. (2013) described the recent climatic characteristics of the region based on regular measurements on Samoylov Island in the southern part of the delta (Fig. 18) during the period from 1998 to 2011. The annual mean air temperature was −12.5 °C with February mean temperatures of −33.1 °C and July mean temperatures of 10.1 °C. Rainfall usually took more than half of annual precipitation with a mean of 125 mm. Snow accumulation usually began in October and snow melt typically started in the second half of May and lasted until early June. The snow depth featured high spatial heterogeneity due to microtopographic features (i.e., polygonal relief) and snow redistribution by wind, but typically did not exceed several decimeters.

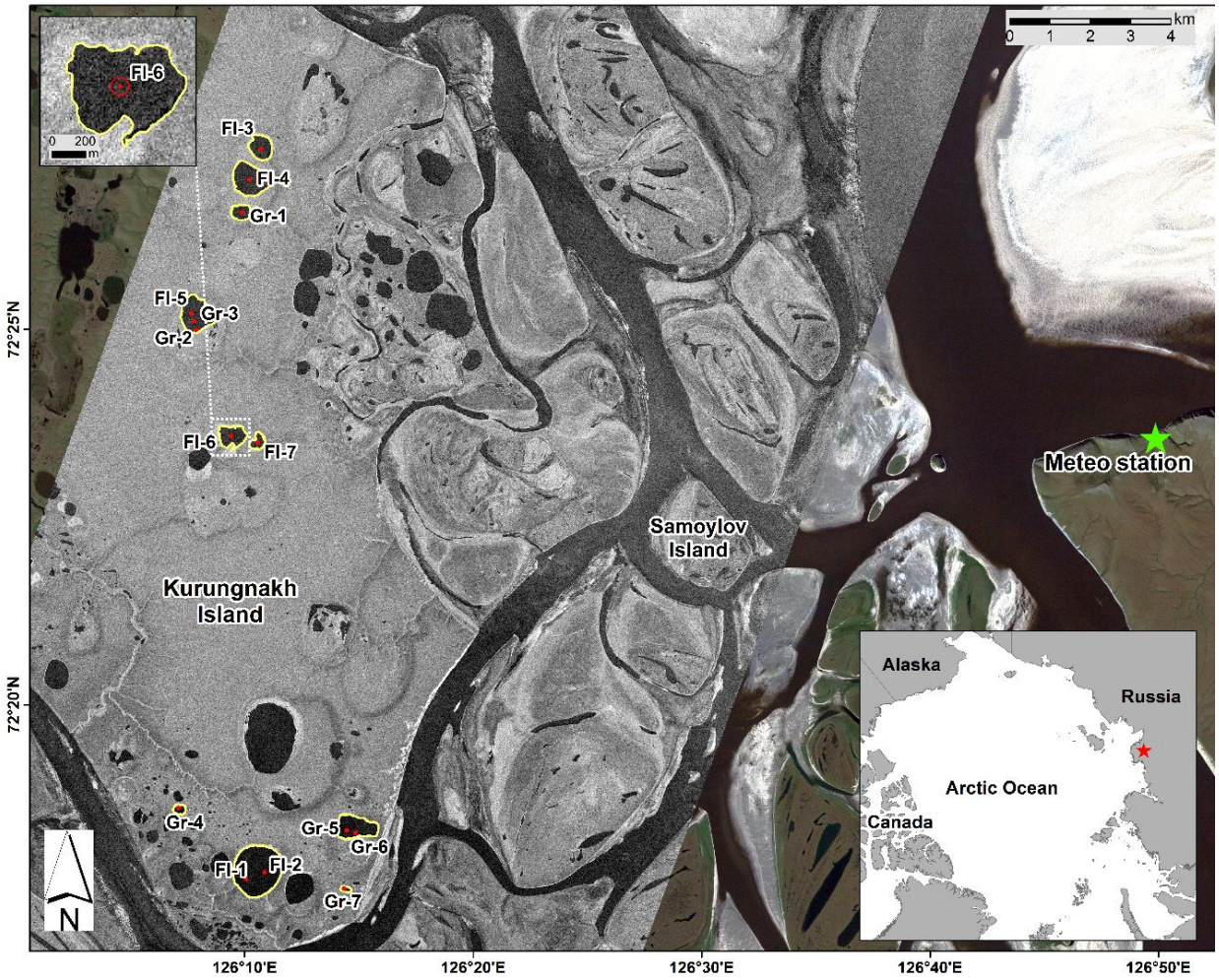

Figure 18. TSX backscatter intensity image from 25 August 2012 (underlain by a RapidEye image; RGB 3-2-1) of the study area with lakes of this study delineated in yellow. Drilling locations in April 2015 are marked as red dots. The meteorological station is marked as a green star. The upper left inset shows an example of a region of interest (ROI) around the drilling location. In the lower right inset, the location of the study area is marked as a red star.

In this study, we focus on the southern part of the delta, particularly on Kurungnakh-Sise (or Kurungnakh) Island (Fig. 18). The main part of the island consists of Pleistocene Ice Complex deposits (also known as Yedoma), which are underlain by fluvial sands and covered by a thin Holocene layer. The island has a maximum elevation of 55 m a.s.l. On its generally flat surface, deep thermokarst lakes and basins have made incisions as a result of permafrost degradation that started about 12 ka ago. About 7.5% and 38% of the island area is covered by thermokarst lakes and basins, respectively. Only 16% of the total basin area is

occupied by remaining lakes, indicating past and current drainage processes (Morgenstern et al., 2011).

3.4 Data and Methods

3.4.1 In Situ Measurements

In order to evaluate the potential of TSX to monitor ice grounding, in situ ice thickness measurements were collected at 14 locations from a sample of 10 lakes in April 2015 (Fig. 18, Table 4). Additionally, snow depth on the ice surface and water depth beneath the ice cover (if present) were measured. Seven of these locations featured grounded ice and the other seven floating ice. In the following, we refer to the former locations as "shallow" and the latter as "deep".

Table 4. Coordinates of measurements and measured parameters in April, 2015. Grey shading is for the shallow locations where the ice was determined to be grounded. Total depth in the last column includes ice thickness and water depth beneath (if present).

No.	Date	Name	Lon, E	Lat, N	Snow Cover, m	Ice Thickness, m	Total Depth, m
1	13/4/2015	Fl-1	126.1785	72.2987	0	1.90	4.55
2	13/4/2015	Fl-2	126.1653	72.2971	0	1.98	6.45
3	20/4/2015	Fl-3	126.1507	72.4592	0.28	1.55	5.00
4	20/4/2015	Fl-4	126.1433	72.4522	0.15	1.65	2.40
5	20/4/2015	Gr-1	126.1390	72.4449	0.15	1.80	1.80
6	20/4/2015	Fl-5	126.1052	72.4220	0.15	1.65	2.35
7	20/4/2015	Gr-2	126.1092	72.4184	0.18	1.60	1.60
8	20/4/2015	Gr-3	126.1074	72.4203	0	1.54	1.54
9	20/4/2015	Fl-6	126.1389	72.3952	0.24	1.65	2.55
10	20/4/2015	Fl-7	126.1586	72.3940	0.42	1.70	2.50
11	20/4/2015	Gr-4	126.1134	72.3121	0	1.58	1.58
12	20/4/2015	Gr-5	126.2370	72.3088	0	1.05	1.05
13	20/4/2015	Gr-6	126.2436	72.3084	0	1.10	1.10
14	13/4/2015	Gr-7	126.2371	72.2959	0	1.70	1.70

3.4.2 SAR Data

TSX is a synthetic aperture radar (SAR) satellite, operating at X-band (wavelength 3.1 cm, frequency 9.6 GHz). The SAR time series used in this study includes 95 StripMap Single-Look Slant Range Complex (SSC) images acquired by TSX between August 2012 and October 2015, at approximately 08:34 local time (22:34 UTC). The time span between acquisitions was 11 days, with a few exceptions when the time spans were 22 and 44 days. The slant range and azimuth pixel spacing is 0.9 m and 2.4 m, respectively. The scene covered an area of approximately 18 km × 56 km. The

chosen orbit was in descending overpass and the radar was right-looking. The acquisition incidence angles were between 31.6 ° and 31.7 °, and polarization was HH for all images.

3.4.3 SAR Data Processing

The data were processed using the commercial radar software Gamma (Werner, 2000). SSC data were converted to Gamma Single Look Complex (SLC) format and the SLC data were then consecutively co-registered with a subpixel accuracy (typically better than 0.2 pixel). The co-registered SLC data were multi-looked by factors of 4 and 3 in range and azimuth directions, respectively, in order to obtain intensity values with reduced speckle and roughly square ground range pixels. Intensity images were calibrated to sigma naught and converted to dB using:

$$\sigma_{dB}^{0} = 10\lg(k_s \times |DN|^2 \times sin\theta), \qquad (5)$$

where k_s is the calibration constant, DN is the amplitude of a complex number representing a pixel value of SLC data, and θ is the local incidence angle.

Interferometric coherence is the magnitude of the complex cross-correlation coefficient of an SAR image pair. The cross-correlation coefficient was computed using:

$$\rho(x,y) = \frac{\langle s_1(x,y)s_2^*(x,y)\rangle}{\sqrt{\langle|s_1|^2\rangle\langle|s_2|^2\rangle}}, \qquad (6)$$

where ρ is the coherence value at pixel location (x,y), s_1 and s_2 are the complex values of SLC images 1 and 2 at pixel location (x,y), and * stands for the complex conjugation. The spatial averaging (marked by ⟨⟩) was processed over a window of 3 × 3 pixels. 83 coherence images, each with a temporal baseline of 11 days, were obtained from interferometric pairs of SLC images.

Both the backscatter intensity images and the coherence images were geocoded to the WGS84 ellipsoid with a pixel size of 10 m × 10 m in the Universal Transverse Mercator (UTM) projection Zone 52N. A region of interest (ROI) was created around each in situ ice thickness measurement location as a circle with a diameter of

approximately 10 pixels (Fig. 18). Mean backscatter intensity and coherence values were extracted for each ROI of the images analysed.

3.4.4 Lake Ice Model

The one-dimensional thermodynamic Canadian Lake Ice Model CLIMo (Duguay et al., 2003) was used to simulate ice thickness and ice dates (ice-on and ice-off). We used the simulated ice thickness to retrieve depth of the shallow locations based on TSX backscatter intensity changes. One of the advantages of the model is that it takes into account overlying snow cover, which is a key factor for ice growth. CLIMo is described in detail in (Duguay et al., 2003) and has previously been shown to perform very well for the estimation of ice thickness of shallow Arctic water bodies (Duguay et al., 2003; Jeffries et al., 2005; Brown and Duguay, 2011; Surdu et al., 2014; Gunn et al., 2015a).

In this study, the model was forced for two lake depths representing the minimum and maximum depths of the lakes sampled in the field (1.05 m and 6.45 m; Table 4) using daily mean meteorological data obtained from a station located approximately 20 km to the east of the area of investigation (Fig. 18). Input data include air temperature, relative humidity, wind speed, cloud cover and snowfall (http://rp5.ru/Weather_archive_on_Stolb_Island). No snow density measurements were collected in the field in 2015 and past snow density from the area was measured only for land (Boike et al., 2013). Sturm and Liston (2003) reported about 20% higher density for lake snow than for land snow on the Arctic Coastal Plain, Alaska and provided average lake snow density value of 330–340 kg/m^3. We used a constant dry snow density value of 330 kg/m^3 in our model simulations. Besides ice thickness, the model output provides snow depth calculated from the input snowfall. Wind driven snow redistribution across the lakes is common on Arctic lakes and in our study area (see Table 4). Therefore, model simulations were performed using different snow cover scenarios from 0 to 100% of the precipitation-derived snow depth, with 0 corresponding to a snow free lake ice surface and 100% to the full amount of the calculated snow depth. In situ snow depth measurements on the lakes (Table 4) showed a wide range, corresponding to model scenarios from 0 to > 200% of the snow cover. However, these measurements represented snow depth at specific

points on a particular date (13 or 20 April 2015). Therefore, they did not necessarily capture the actual snow depth across the lakes, but rather exemplify the snow depth variability and possible ranges.

3.5 Results

Figure 19 shows time series of TSX backscatter for the deep and shallow lake locations as well as air temperatures for the period from August 2013 to October 2015. These times series are used for the bedfast ice detection and monitoring, as well as for the interpretation of ice phenology.

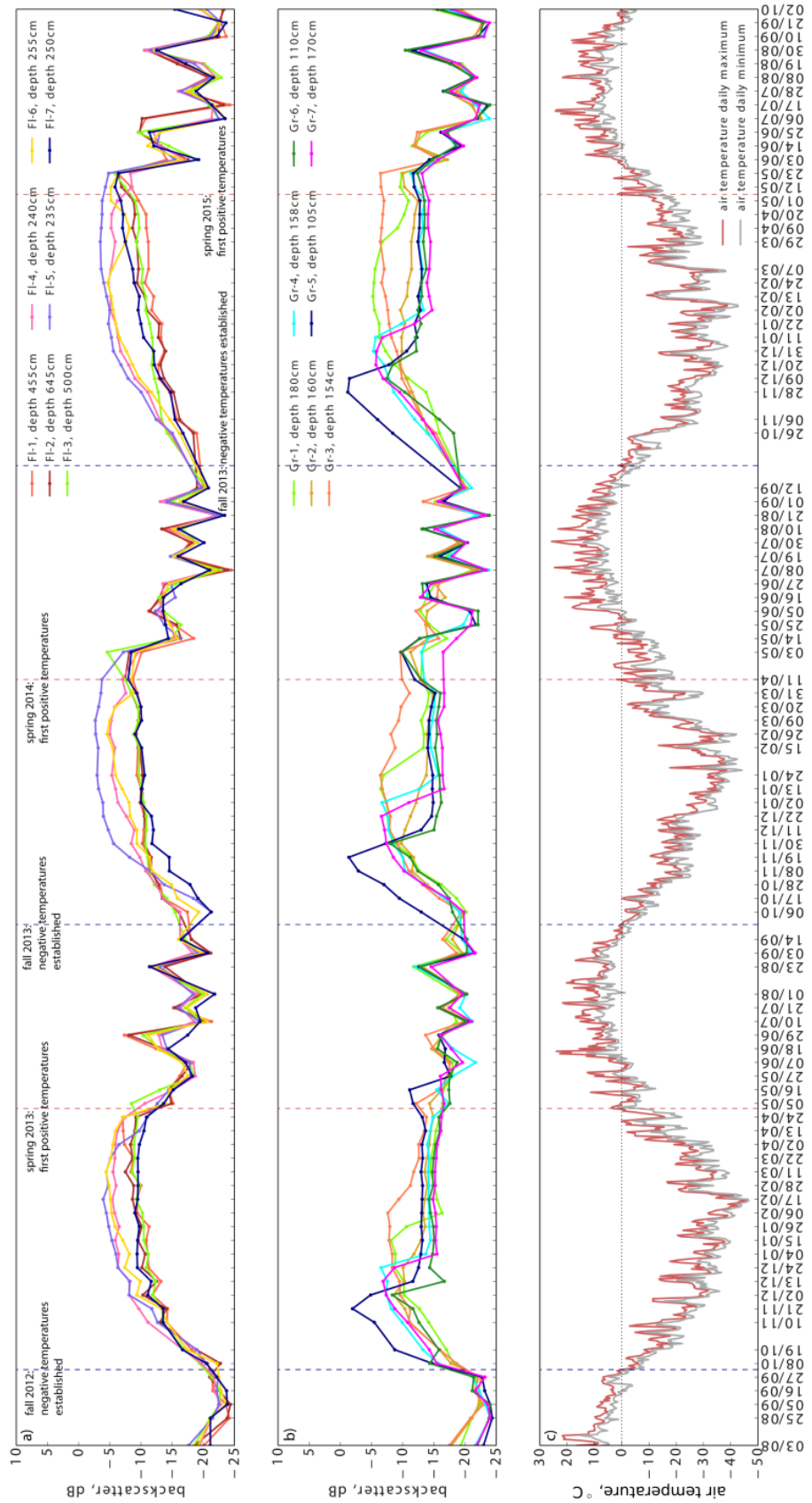

Figure 19. (a) TSX backscatter intensity time series for seven deep locations (Fl-1–Fl-7) with presumably floating ice in winter; (b) TSX backscatter intensity time series for seven shallow locations (Gr-1–Gr-7) with presumably grounded ice in winter; (c) Daily minimum and maximum air temperatures during study period. Dates on x-axis are TSX acquisitions (DD/MM).

3.5.1 Ice Grounding

3.5.1.1 Backscatter Intensity Time Series

Based on the in situ measurements obtained in April 2015, we separated seven locations where the ice was floating from seven other locations where the ice was grounded. Backscatter intensity (or simply backscatter) time series for the locations with floating and grounded ice are shown in Figure 19a and 19b, respectively. The backscatter temporal signatures largely confirmed the separation between the two types of lake ice. Backscatter from the floating ice increased after the freeze onset, then continued to increase gradually and then remained stable over the entire winter (stable stage) until melt onset. Backscatter from the grounded ice featured an abrupt decrease after the ice reached the lake bottom and remained low until surface melt onset. The time of the ice grounding was partly correlated to a location depth: backscatter from the shallowest locations (Gr-5 and Gr-6) decreased earlier than backscatter from deeper locations for all three seasons. Other locations, however, did not fully follow this temporal pattern. Backscatter from two locations (Gr-2 and Gr-3) lacked an abrupt drop but decreased gradually. The decrease in backscatter from Gr-2 lasted for two months in both 2012–2013 and 2013–2014 and resulted in a total decrease of 5.3 dB and 4 dB, respectively. In winter 2014–2015, a slight but consistent decrease in backscatter (2.9 dB in total) from Gr-2 lasted for three months. Backscatter from Gr-3 decreased by 6.2 dB and 5.4 dB in total over periods of three and two months in 2012–2013 and 2013–2014, respectively, but no decrease was demonstrated in 2014–2015. In addition, backscatter from Gr-1 featured a less pronounced drop in 2014–2015 (compared to the two previous years) and decreased gradually over a two month period by 5.2 dB in total. Other locations featured a clear drop in backscatter in the range of 4–13 dB, which lasted 11, 22 or 33 days. For cases when the backscatter drop lasted 22 or 33 days, we defined the time of ice grounding as the first acquisition date of the observed backscatter drop which was greater than the radiometric uncertainty (~1 dB). Table 5 shows the dates of the first backscatter drop and corresponding magnitude of this drop.

Table 5. Timing of the first drop in TSX backscatter intensity for three winter seasons and corresponding values of this drop. Locations are ordered from the deepest to the shallowest.

Location	2012–2013		2013–2014		2014–2015	
	Date of the First Backscatter Drop	Magnitude of the Drop, dB	Date of the First Backscatter Drop	Magnitude of the Drop, dB	Date of the First Backscatter Drop	Magnitude of the Drop, dB
Gr-1, 180 cm	26 January	2.5	15 February*	6.4	9 April	2.5
Gr-7, 170 cm	24 December	1.8	2 January	4.4	22 January	5.2
Gr-2, 160 cm	13 December	1.7	no clear drop		no clear drop	
Gr-4, 158 cm	4 January	7.2	13 January	6.0	22 January	4.1
Gr-3, 154 cm	17 February	1.8	15 February*	2.4	no drop	
Gr-6, 110 cm	13 December	8.3	11 December	7.0	31 December	3.8
Gr-5, 105 cm	2 December	2.9	30 November	5.9	20 December	6.3

* No TSX acquisition between 24 January and 15 February 2014: backscatter drop is indicated for 22-day period.

3.5.1.2 SAR- and CLIMo-Derived Ice Thicknesses Versus in situ Measured Ice Thicknesses

We used CLIMo to simulate ice thickness for three seasons (Fig. 20). Two curves represent two extreme snow cover scenarios, 0% and 100% of snow cover. In situ ice thicknesses of the floating ice locations in April 2015 showed consistency with the simulated ones within the range between 25 and 125%–150% of the snow cover scenarios (for clarity, scenarios other than 0% and 100% are not shown in Fig. 20).

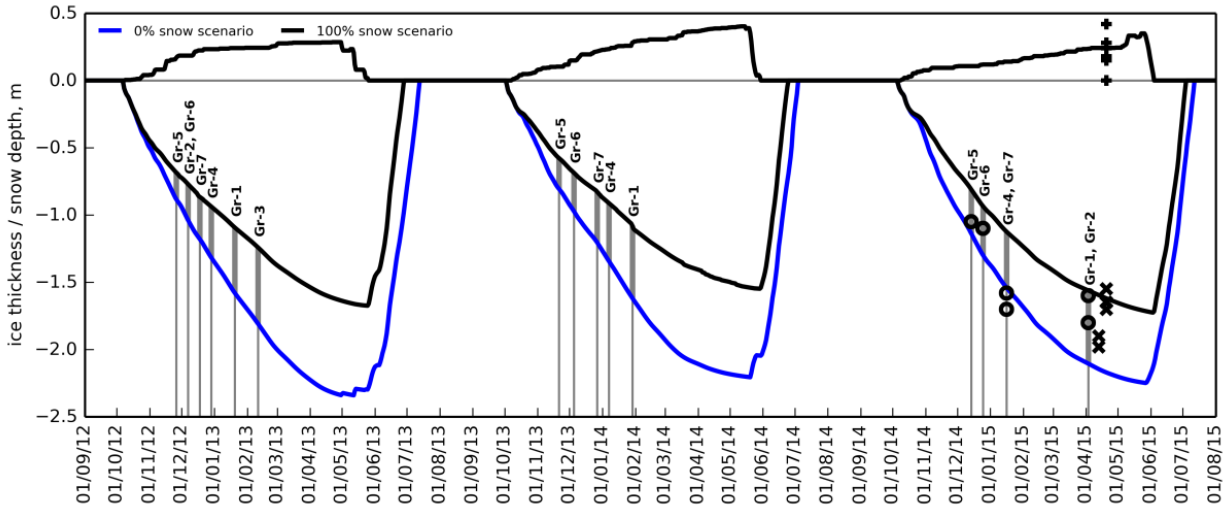

Figure 20. Model simulations of snow on ice and ice thickness for 0 and 100% snow cover scenarios for three ice seasons (2012–2013, 2013–2014, 2014–2015). In situ measured ice thicknesses for the floating locations (Fl-1–Fl-7) are shown with the "×" symbols. In situ measured snow depths are shown with the "+" symbols. Vertical lines correspond to the dates of ice grounding extracted from TSX time series. In situ ice thicknesses (measured in April 2015 at the grounded ice locations) by the time of ice grounding are shown with "o" symbols. Date format on x-axis is DD/MM/YY.

We assigned the time of the first TSX backscatter intensity decrease (i.e., mid-date of the 11-day period) of the seven grounded locations to the simulated ice thickness on those dates. We then compared the simulated ice thicknesses against ice thicknesses measured in situ at grounded locations in April 2015 (Table 6, Figure 20). In situ ice thicknesses were mostly in range of simulated ones in 2014–2015. Modelled ice thicknesses at locations Gr-4 and Gr-7 slightly underestimated in situ ice thicknesses. Field observations in April 2015 reported no snow at the locations Gr-4, Gr-5, Gr-6 and Gr-7 and the presence of snow on ice at locations Gr-1 and Gr-2. Although these snow conditions do not necessarily mean that they were the case for the entire winter, in situ ice thicknesses at lake locations without snow were closer to simulated ones with 0% snow cover scenario, and in situ ice thicknesses at locations with the presence of snow fell between 50% and 75%–100% of snow cover scenarios

In winters 2012–2013 and 2013–2014, most of the locations showed substantial differences between simulated ice thicknesses and those measured in situ in April 2015, with in situ ice thicknesses typically larger (up to 0.5 m) than that simulated for the two winters, even with a 0% snow cover scenario.

Table 6. Comparison of simulated and in situ measured ice thicknesses by the time of ice grounding.

Location	In Situ Measured Ice Thickness, m (April, 2015)	Simulated Ice Thickness by the Time of Ice Grounding, m (100% to 0% snow cover scenario)		
		2012–2013	2013–2014	2014–2015
Gr-5	1.05	0.68–0.88	0.58–0.81	0.81–1.14
Gr-6	1.1	0.77–1.04	0.69–0.97	0.93–1.3
Gr-3	1.54	1.24–1.81		
Gr-4	1.58	0.94–1.32	0.91–1.34	1.12–1.54
Gr-2	1.6	0.77–1.04		1.56–2.1
Gr-7	1.7	0.86–1.18	0.83–1.2	1.12–1.54
Gr-1	1.8	1.09–1.58	1.08–1.62	1.56–2.1

3.5.1.3 Spatio-Temporal Variability of Bedfast Ice

Figure 21 shows different selected stages of lake ice development on approximately the same dates (end of November, middle of January, end of March and middle-end of April) of all three seasons for one of the lakes. Spatially, ice grounding began mainly from the northeast- and south oriented shores, whereas other lake margins appeared to be deeper as ice grounding started much later (or did not at all). There was an evident interannual variability in this spatial pattern: by the same time of year, grounded ice occupied much more area of the lake in the first year than in the second year, while the third year featured dramatically less grounded ice than the previous years.

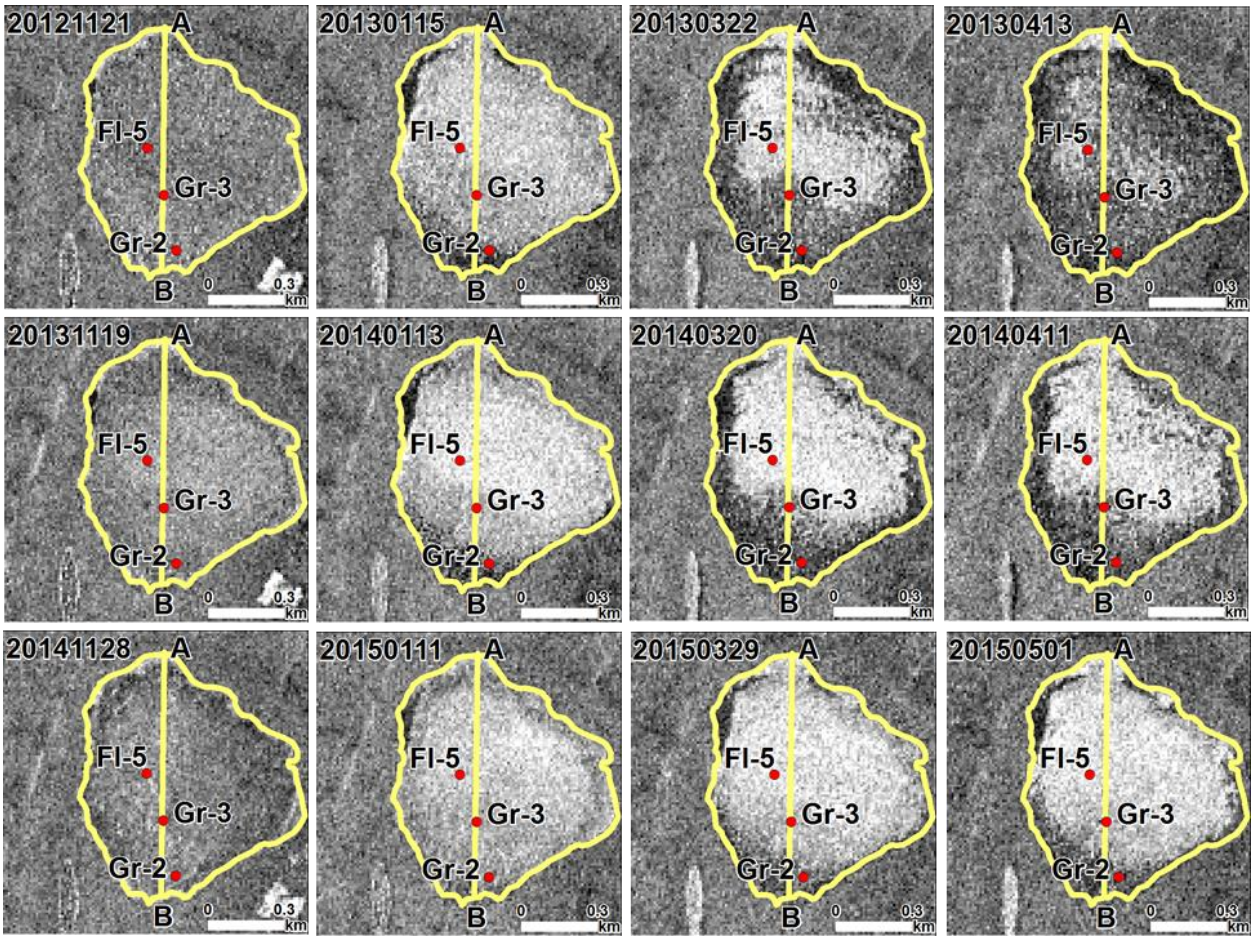

Figure 21. Selected stages of lake ice evolution for ice seasons 2012–2013 (upper row), 2013–2014 (middle row) and 2014–2015 (lower row). Profile A–B is used to represent the spatio-temporal development of backscatter intensity (Fig. 22). Date format is YYYYMMDD.

In order to demonstrate the spatio-temporal pattern without excluding any of 95 TSX images, we selected a profile across the same lake and produced a time series of backscatter intensity along this profile (Fig. 22). The time series shows the progression of ice grounding as darker pixels appear along profile A–B. The ice grounding propagation from the south shore (B) towards the middle of the lake is evident during each of three years, as well as interannual variability reflected in a much smaller area of dark pixels in the last winter compared to the two previous years.

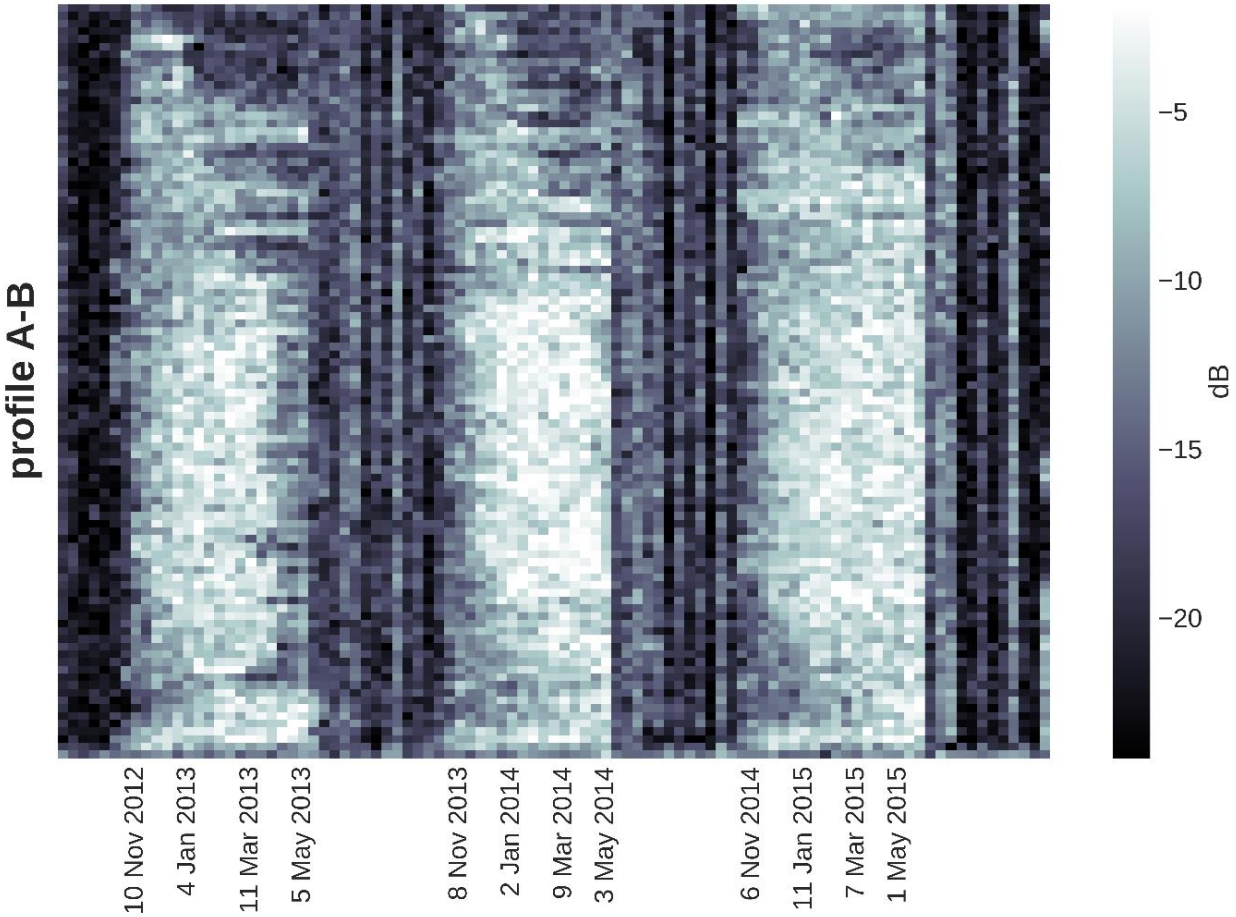

Figure 22. Spatio-temporal evolution of backscatter intensity along profile A–B (from Fig. 21).

3.5.1.4 Coherence Time Series

Figure 23 illustrates the difference between grounded and floating ice as revealed on both TSX backscatter intensity and coherence images. Grounded ice appeared dark (low backscatter) in a late winter backscatter image (upper row) due to low return caused by absorption of the SAR signal in the lake bottom sediments. Grounded ice appeared bright (high coherence) in a late winter coherence image (lower row) due to the absence of a change in the backscattering interface between two images, comprising a coherence pair.

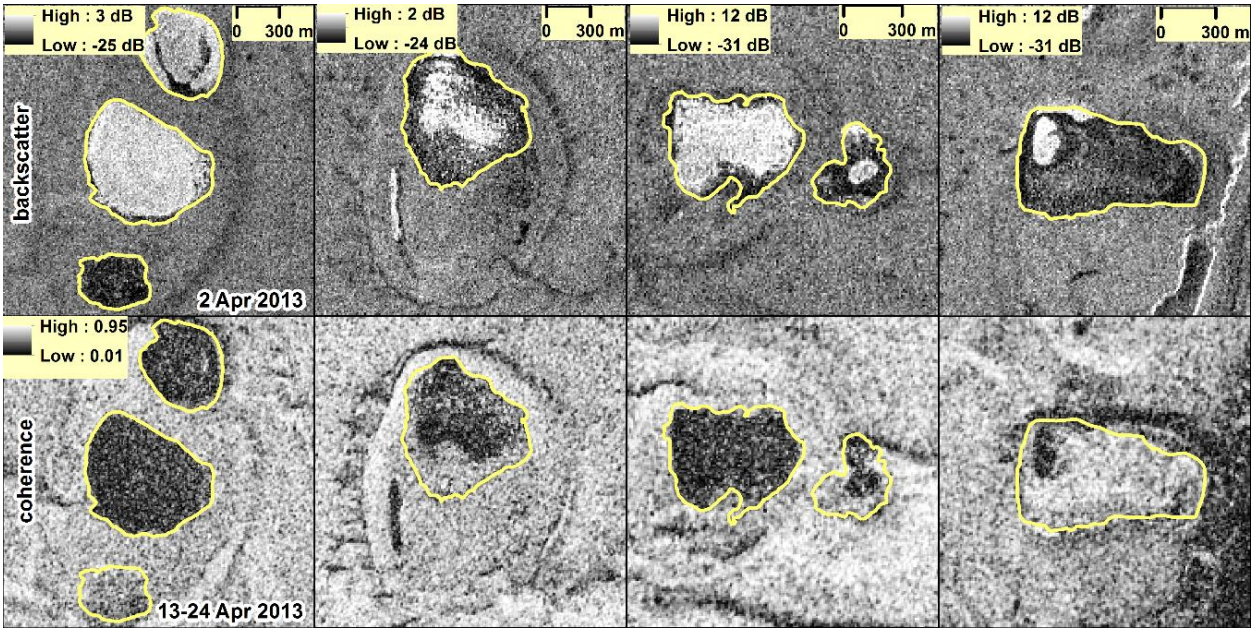

Figure 23. Upper row: late winter backscatter image (2 April 2013) which shows the difference in backscatter for grounded (dark) and floating (bright) ice. Lower row: late winter coherence image (13–24 April 2013) which shows the difference in coherence for grounded (bright—higher coherence) and floating (dark—lower coherence) ice.

In general, well pronounced increases in coherence were observed for all grounded locations in the 2012–2013 season, and for most of the grounded locations in the 2014–2015 seasons (Fig. 24). The 2013–2014 season did not feature a well pronounced coherence increase for all grounded locations, but rather variable and generally low coherence. Table 7 presents the periods of the first coherence increase and corresponding coherence values for all grounded locations for the three winter seasons.

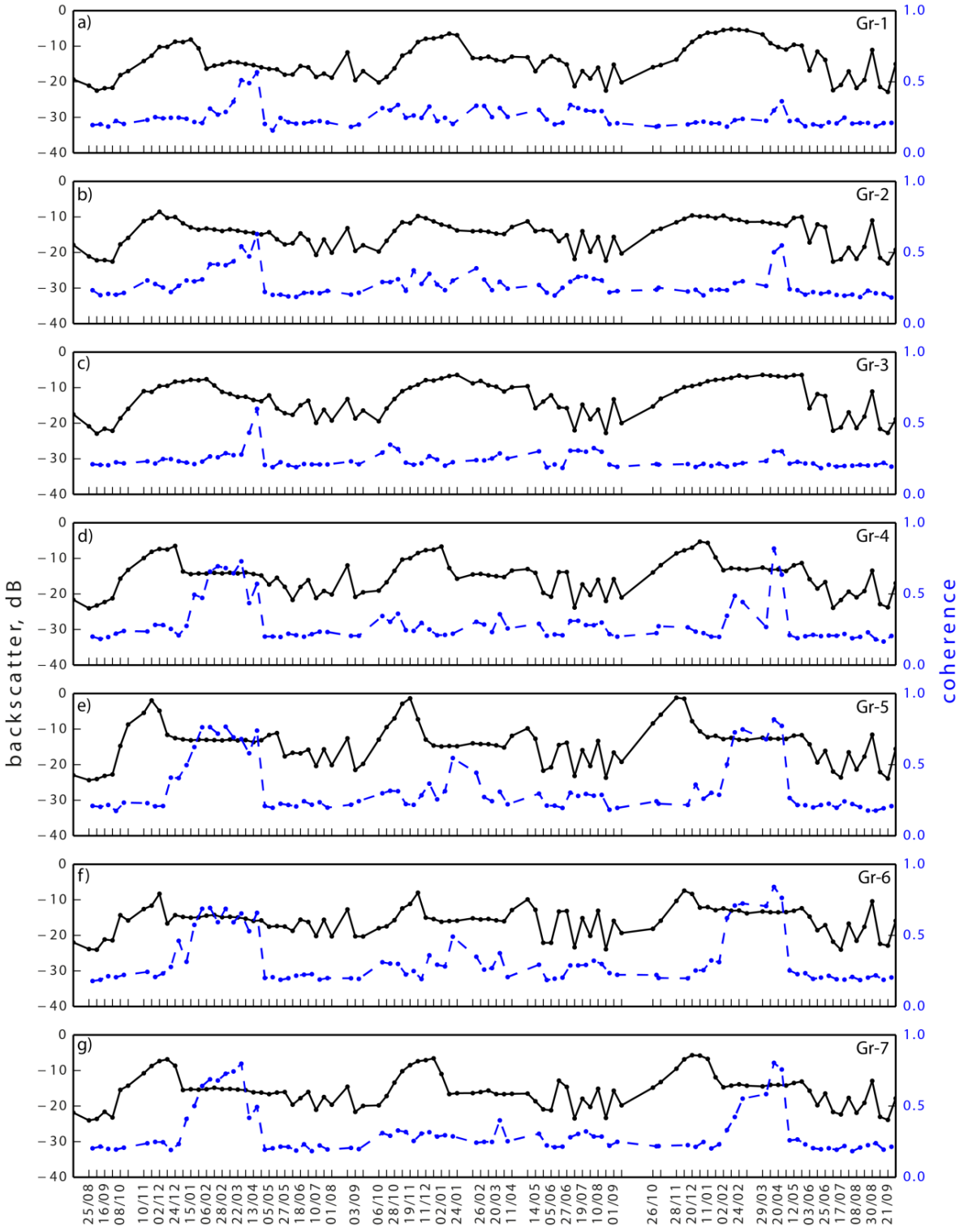

Figure 24. Backscatter intensity (black solid line) and coherence (blue dashed line) time series for all grounded locations over three years (2012–2015): (a) Gr-1; (b) Gr-2; (c) Gr-3; (d) Gr-4; (e) Gr-5; (f) Gr-6; (g) Gr-7. Ticks on x-axis are dates of TSX acquisitions (every second tick is labelled). Date format is DD/MM.

Table 7. Periods of the first increase of coherence for three seasons and corresponding coherence values. Locations are ordered from the deepest to the shallowest.

Location	2012–2013		2013–2014		2014–2015	
	Period of the First Coherence Increase	Coherence	Period of the First Coherence Increase	Coherence	Period of the First Coherence Increase	Coherence
Gr-1, 180 cm	6–17 February	0.3	-	-	20 April–1 May	0.36
Gr-7, 170 cm	4–15 January	0.41	20-31 March	0.4	13–24 February	0.42
Gr-2, 160 cm	6–17 February	0.42	-	-	9–20 April	0.5
Gr-4, 158 cm	15–26 January	0.5	-	-	13–24 February	0.49
Gr-3, 154 cm	2–13 April	0.43	-	-	-	-
Gr-6, 110 cm	24 December-4 January	0.46	13-24 January	0.5	2–13 February	0.62
Gr-5, 105 cm	13–24 December	0.4	13-24 January	0.55	2–13 February	0.5

In general, pronounced coherence peaks appeared for the grounded ice locations and the seasons which also featured well pronounced backscatter drops (except for the season 2013–2014 when coherence increase did not occur in most cases). There were some exceptions: location Gr-2 did not demonstrate a well pronounced backscatter drop in the 2014–2015 season, but coherence featured a clear increase for this season (Fig. 24b). For most cases, the first increase in coherence occurred later than the first drop of backscatter. The maximum coherence values were observed before spring melt, which was characterized by an abrupt drop in coherence down to values of ~0.2 for all the grounded ice locations.

3.5.2 Ice Phenology

3.5.2.1 Freeze Up and Ice Growth

In the fall of 2012, air temperatures fell below 0 °C between the TSX acquisitions of 27 September and 8 October (Figure 19c). The mean backscatter for all locations on 27 September was −22 ± 0.6 dB. On 8 October, the mean backscatter was −20.8 ± 1.1 dB for the deep locations and −16.4 ± 1.6 dB for the shallow locations. Thus, shallow locations showed a clear increase in backscatter between these dates (3.5–8 dB). Detection of the initial freeze-up for the deep locations was hampered by the low

contrast between young thin ice cover and calm open water. Shallow locations likely developed a thicker ice cover during this 11-day period than deeper locations, which led to a pronounced backscatter increase for shallow locations. Visual inspection of the image from 8 October revealed that deeper lakes featured bright cracks or ridges whereas the surrounding ice surface appeared dark (Figure 25b), indicating the early stage of freeze-up. After 8 October backscatter began to increase gradually for all lakes. Backscatter from the floating ice locations reached the stable stage around 24 December 2012. The mean backscatter values over the period from 24 December 2012 to 2 April 2013 for the floating ice locations ranged from −9.9 to −5.2 dB (standard deviations between 0.4 and 1.3 dB).

In the fall of 2013, air temperatures fell below 0 °C between 14 September and 6 October TSX acquisitions, but after 25 September (there was no TSX acquisition on 25 September) (Figure 19c). The image of 14 September was slightly affected by wind (Figure 25e), so the mean backscatter for all locations on this date was relatively high (−17.8 ± 1.5 dB) compared to e.g., the previous acquisition. The mean backscatter value calculated from all locations (except of the shallowest location Gr-5) on 6 October was −18.7 ± 1.8 dB. Thus, detection of the initial freeze-up was hampered by the low contrast between wind-affected open water from the previous image and the thin undeveloped ice cover from the latter image. Visual inspection revealed cracks and ridges on the lakes in the image of 6 October, indicative of the presence of ice (Figure 25f). After 6 October, backscatter began to increase gradually for all locations. Backscatter from the floating ice locations reached the stable stage around 30 November 2013. The mean backscatter values over the period from 30 November 2013 to 11 April 2014 for the floating ice locations ranged from −10.2 to −3.6 dB (standard deviations between 0.5 dB and 1.7 dB).

In the fall of 2014, air temperatures fell below 0 °C between 12 September and 26 October of the TSX acquisitions (there were no TSX acquisitions on 23 September as well as on 4 and 15 October) (Figure 19c). The three missing images did not allow us to detect the initiation of freeze-up. However, the mean backscatter intensity for all locations (except of the shallowest location Gr-5) increased during this period from −20 ± 0.6 dB to −15.9 ± 1.6 dB. The mean backscatter values over the period from 31

December 2014 to 1 May 2015 for the floating ice locations ranged from −11.7 to −4.3 dB (standard deviations between 0.6 dB and 1.8 dB).

At the stable stage, deeper floating locations (Fl-1, Fl-2 and Fl-3) showed lower backscatter intensity (by ~4 dB) than shallower floating locations (Fl-4, Fl-5 and Fl-6) for all three winter seasons, with the exception of the rather shallow location Fl-7 featuring lower backscatter in the order of backscatter values from deeper locations (Table 8, Figure 19a).

Table 8. Mean backscatter intensity for the floating ice locations during the stable stage for three seasons.

Location	Depth, m	Ice Thickness, m	Mean Backscatter in 2012–2013 (24 Dec-2 Apr), dB	Mean Backscatter in 2013–2014 (30 Nov-11 Apr), dB	Mean Backscatter in 2014–2015 (31 Dec-1 May), dB
Fl-1	4.55	1.9	−9.8±1.3	−9.7±0.5	−11.7±1.2
Fl-2	6.45	1.98	−9.2±1	−9.7±1	−10.5±1.8
Fl-3	5.0	1.55	−9.9±0.9	−9.7±1	−10.4±1
Fl-4	2.4	1.65	−6±0.4	−6.6±1.3	−5.6±0.6
Fl-5	2.35	1.65	−5.2±0.8	−3.6±0.8	−4.3±0.7
Fl-6	2.55	1.65	−5.9±1.2	−7.2±1.7	−6.3±1.2
Fl-7	2.5	1.7	−9.5±0.2	−10.2±1.1	−8.9±1.6

3.5.2.2 Melt Onset

Melt onset marks the beginning of snow or ice surface melt during the break-up period. In spring 2013, a decrease in backscatter in the range of 2.7–8.1 dB was observed for deep locations between 24 April and 5 May (with the exception of Fl-5 showing a 3.2 dB decrease between 2 and 13 April and Fl-3 showing 4.5 dB decrease between 5 and 16 May) (Fig. 19a). Shallow locations did not demonstrate a clear pattern (Fig. 19b): the time when backscatter intensity began to deviate from its stable stage varied from 5 May to 7 June for different locations, and deviations were both negative and positive. Intermittent positive air temperatures were first detected between 24 April and 5 May 2013 (Fig. 19c). A strong coherence drop occurred between 24 April and 5 May (Fig. 24).

In spring 2014, a prominent backscatter decrease in the range of 5.9–10.4 dB occurred between 3 and 14 May for deep locations (Fig. 19a). For shallow locations, the same period corresponded to a more moderate backscatter decrease of 1.1–3.9

dB (Fig. 19b). Backscatter intensity alterations already began between 31 March and 11 April for some shallow locations. Intermittent positive air temperatures were first detected between 31 March and 11 April (Fig. 19c).

In spring 2015, a significant backscatter decrease in the range of 7.8–13.2 dB occurred between 23 May and 3 June for deep locations (Fig. 19a). For shallow locations, the same time period corresponded to a backscatter decrease in the range of 2.4–9.4 dB (Fig. 19b). Positive air temperatures were reached during this time period as well (Fig. 19c). However, some shallow locations revealed a slight increase in backscatter (up to 2.2 dB) between 1 and 12 May. A strong coherence drop occurred between 1 and 12 May (Fig. 24).

3.5.2.3 Water-Clear-of-Ice

Water-clear-of-ice corresponds to the date when a water body becomes completely ice-free (i.e., it marks the end of the break-up period). In the summer of 2013, water-clear-of-ice was detected on 10 July for all lakes (Fig. 25d), while most of the lakes were covered by ice on the image of 29 June (previous acquisition) (Fig. 25c).

In summer 2014, water-clear-of-ice was detected on 8 July for all lakes (Fig. 25h). The previous image (27 June, Fig. 25g) was affected by wind (wind speed at 08:30 local time was 5.7 m/s). However, comparing this image with the image of 29 June 2013 (Fig. 25c), acquired under similar wind conditions (wind speed of 5.2 m/s), partial ice coverage was apparent on the latter image. Thus, the lakes were likely already ice free on 27 June 2014.

In the summer of 2015, water-clear-of-ice was detected on 17 July (Fig. 25l), while the image from 6 July featured significant ice cover presence on some lakes (Fig. 25k).

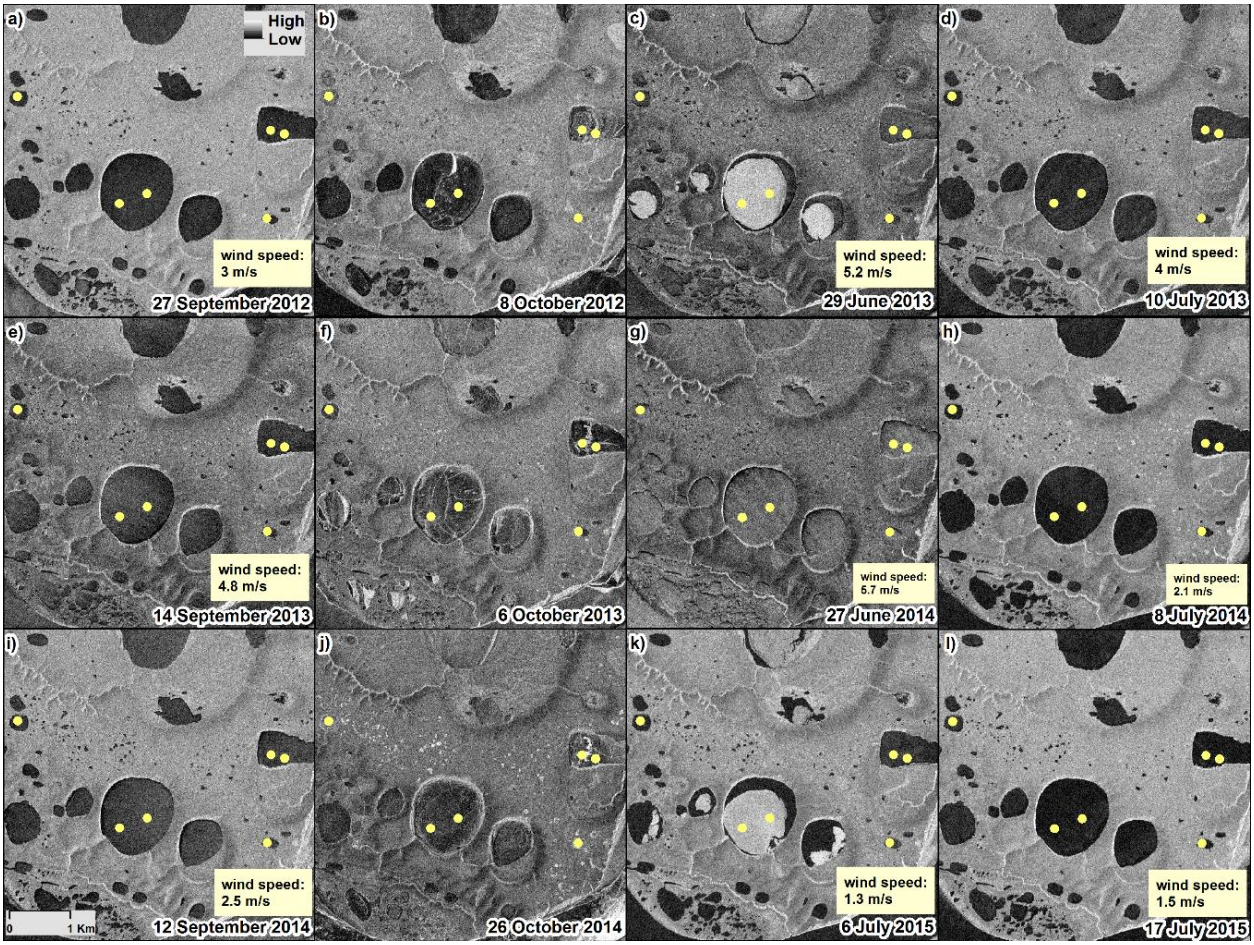

Figure 25. Sub-areas of TSX intensity maps showing events in the ice phenology cycle for three ice seasons: (a–d): 2012–2013; (e–h): 2013–2014; (i–l): 2014–2015. Yellow dots are drilling locations. Wind speed measurements are from automatic weather station on Kurungnakh Island at 08:30 local time of TSX acquisition day (TSX acquisition is at 08:34 local time).

3.6 Discussion

3.6.1 Ice Grounding

3.6.1.1 Backscatter Intensity

Our results demonstrate that TSX backscatter intensity is a viable tool for the monitoring of floating/grounded lake ice regimes. Backscatter intensity signatures mostly confirmed the in situ measurements from April 2015: locations where the ice was found grounded showed a drop in backscatter, whereas floating ice locations exhibited a stable backscatter over the entire winter. Out of 21 cases (seven grounded locations and three years), 14 showed a very well pronounced backscatter drop, and seven exhibited a smooth backscatter decrease over a few months without a distinct drop. We relate the lack of such a manifest in backscatter drop to be associated with the selection of the ROIs (group of pixels) which might include a mixed signal from both floating and grounded ice. The choice of the ROIs was based on drilling locations where the ice thickness was measured in situ. These locations were georeferenced using a simple handheld Garmin GPS device, which has an accuracy of about 10 m. Therefore, to ensure that the ROI includes the drilling point, the size of ROI was chosen to be about 100 m in diameter. Consequently, the lake ice thickness could vary spatially within the ROI with ice being partly grounded or floating. Such non-uniform ice grounding can also be naturally caused by heterogeneous lake bathymetry, especially when a ROI is chosen during a transition between the shallow littoral zone and the deeper pelagic zone. This issue has also been raised by Brown et al. (2010) in the detection of fish overwintering pools under the ice on the Sagavanirktok River, Alaska, using ASAR C-band with 30 m spatial resolution. In particular, they found that backscatter intensity was influenced by both presence of floating and grounded ice at the edge of the pools surveyed in the field.

On the one hand, the TSX time series with its 11-day temporal resolution improves the accuracy of the extraction of the timing of ice grounding, compared to previous studies using RADARSAT (with 24-day repeat cycle) or ERS (35 days) data. On the other hand, the multistep drop in backscatter intensity for a number of cases in our study poses difficulties for precise identification of the timing of ice grounding. We

assume that the first decrease of backscatter larger than the radiometric uncertainty of TSX (~1 dB) indicates ice grounding. One possible reason for a subsequent backscatter decrease, if present, can be the freezing of sediments. Morris et al. (1995) found that ERS-1 backscatter intensity from grounded lake ice was about 3 dB higher for a sub-Arctic site compared to an Arctic site. They hypothesized that the lake sediments might not have been completely frozen but still rather wet at the warmer sub-Arctic site, which could explain why the radar return was higher for this site. This assumption may also apply to our case, but rather in a temporal than a spatial context: after the first backscatter decrease lake sediments were potentially wet and not completely frozen, and the following freezing of sediments caused the backscatter to decrease further. A better understanding of SAR signal response to freezing of lake sediments can help towards more confident extraction of the timing of ice grounding in the future. Another possible explanation for the multistep backscatter decrease is non-uniform grounding of the ice: some zones of the ice bottom within the ROI (or even within resolution cell) could be already attached to the bottom whereas other zones were still not grounded, causing backscatter to continue to decrease. By the time the ice became completely bedfast, backscatter intensity stabilized. The same situation could also be considered at the microscale where ice crystals attach to the lake bottom non-uniformly, leaving some pockets with liquid water. A combination of all of the above described processes could also possibly take place.

Various applications could be developed or improved based on explored TSX data. Detection of the lakes with bedfast ice could be useful for the estimation of fish habitat areas and water availability in winter. Fraction of bedfast ice could be estimated on different scales for the assessment of taliks distribution in permafrost. Transition between the bedfast and floating ice regime of a lake could be used as a proxy for the interannual variations in water level or maximum ice thickness.

3.6.1.2 Model Results

For the first time, Jeffries et al. (1996) used ERS-1-derived timing of ice grounding together with the model CLIMo to retrieve the maximum depth of shallow lakes on the Alaskan North Slope; however, no validation of the results was made. Kozlenko

and Jeffries (2000) used the same approach, data and study area to map the bathymetry of shallow lakes and used existing bathymetric maps for the validation, which showed only moderate agreement. We used the same approach and retrieved ice thicknesses at the grounded locations using TSX time series and the model CLIMo. Among the improvements of our study are the better temporal resolution of the SAR time series (11 days compared to 35 days of ERS) and the in situ measured thicknesses of grounded ice. Comparison of retrieved and in situ ice thicknesses showed a reasonably good agreement in the 2014–2015 season, and a divergence in the previous two years, with in situ ice thicknesses typically larger than simulated. Assuming that the timing of ice grounding was derived correctly, this suggests that the water level could have been higher in fall 2014 prior to ice formation than in previous years, leading to thicker ice in winter of 2014–2015.

3.6.1.3 Spatio-Temporal Variability of Bedfast Ice

The present work mainly focuses on the temporal evolution of TSX parameters for a number of discrete locations where in situ ice thickness measurements were available. However, the spatio-temporal evolution of ice grounding for an entire lake is of high importance, for instance, for the extraction of the bathymetry or for interannual monitoring. Our results show a great potential of TSX imagery with its high spatial and temporal resolution to track the progression of ice grounding on a lake. All three years demonstrated different fractions of grounded ice by the end of the winter, with a maximum in 2012–2013 and a minimum in 2014–2015. Since simulations with CLIMo revealed similar maximum ice thicknesses in 2012–2013 (2.34 m for 0 snow cover and 1.67 m for 100% snow cover) and 2014–2015 (2.25 m for 0% snow cover and 1.73 m for 100% snow cover), we assume that variations in water levels could result in such significant differences in the grounded ice patterns between the two years.

3.6.1.4 Coherence

The increase of coherence at grounded locations served as an additional indicator of ice grounding. This increase often occurred later than the drop in backscatter by 2–5 TSX repeat cycles, which can possibly be explained by the following: when the freezing front reaches the depth when all the sediments are dry (water content of

sediments likely decreases with depth), the backscatter becomes stable. The coherence is defined by both amplitude and phase components of the signal and is therefore more sensitive to changes in the backscattering interface. Therefore, the coherence can stay low when the freezing front propagates into the wet sediments. We hypothesize that the first increase of coherence can indicate the stage when the wet layer of sediments becomes frozen and dry, and the maximal coherence can indicate the complete freezing of the sediments before melt onset. Therefore, coherence time series appear to be less robust compared to backscatter intensity time series for estimation of the timing of ice grounding. However, an increase of coherence can help with the detection of ice grounding when the backscatter does not show a clear signal, as for instance in the case of location Gr-2 during winter 2014–2015. Additionally, the coherence time series appears to have the potential for monitoring the freezing of the lake sediments.

Generally low and rather variable (compared to other winters) coherence was observed during the winter of 2013–2014. Such low coherence does not necessarily indicate the absence of lake ice grounding, but can be related to environmental factors on the lake ice surface such as changing snow conditions due to snowfall and snow drifting (Rott et al., 2003).

The high coherence observed for the shallow lakes in the ice seasons 2012–2013 and 2014–2015 should theoretically allow performing an interferometric analysis and generate maps of lake bathymetry, which will be the focus of future work.

3.6.2 Ice Phenology

3.6.2.1 Freeze Onset

Our results demonstrate that TSX backscatter intensity time series can generally be used to monitor lake ice phenology. The freeze-up was characterized by a gradual increase in backscatter, but the very initial stage of ice formation (–21 to –19 dB) was often indiscernible from a calm open water surface. This was also reported in previous studies (e.g. Jeffries et al., 1994; Duguay et al., 2002). Cracks and ridges featured high backscatter intensities compared to the surrounding dark young ice cover, supporting the detection of freeze-up, as reported in previous studies (e.g.

Hall et al., 1994). A few missing images (which were not acquired by TSX due to reasons unknown to us) exactly during freeze-up periods of fall 2013 and 2014 prevented us from discerning the time of freeze onset with confidence (at least not in the order of 11 days) and from comparing freeze onset on an interannual basis. However, simulations with CLIMo did provide an independent and useful complementary estimate of ice-on dates for the deep and shallow lakes when TSX images were not available every 11 days (Table 9).

Table 9. Dates of ice-on and ice-off derived from TSX images and simulated with CLIMo.

	Ice-On TSX (deep and shallow)	Ice-On CLIMo (deep)	Ice-On CLIMo (shallow)	Ice-Off TSX	Ice-Off CLIMo
2012–2013	Between 27 September and 8 October	7 October	3 October	Latest by 10 July (29 June shows significant ice coverage)	30 June – 15 July (depending on snow cover scenario)
2013–2014	Between 14 September and 6 October (one missing image in between)	4 October	27 September	By 27 June (based on comparison with previous year because image is affected by wind)	26 June – 6 July (depending on snow cover scenario)
2014–2015	Three missing images	7 October	27 September	Latest by 17 July (6 July shows significant ice coverage for some big lakes)	6 July – 14 July (depending on snow cover scenario)

The mature stage of ice development for the floating locations was characterized by stable backscatter intensity in the range of −12 to −3.5 dB, which is well within the range of previous investigations (e.g. Duguay et al., 2002; Surdu et al., 2015). Floating ice locations mostly exhibited interannual consistency of backscatter values at the stable stage: every location yielded a similar mean backscatter from year to year, which indicates relatively constant ice growth conditions for each location.

3.6.2.2 Melt Onset

Melt onset was detected in most cases by a prominent backscatter decrease (up to 13 dB) from its stable stage; however, some cases also showed an increase in backscatter. Such contrasting backscatter changes have previously been reported by Jeffries et al. (1994) and Morris et al. (1995) (C-band) for snow covered lake ice and by Strozzi et al. (1997) for terrestrial snow cover (C-band and Ka-band). A decrease in backscatter can be explained by the wetting of snow or ice surface leading to a

reduced signal penetration, while backscatter increase can be observed in the case of the formation of ice crusts caused by melt and refreeze cycles.

In the present study, melt onset was well detected by a significant coherence drop in the 2012–2013 and 2014–2015 winter seasons, consistent in time for all grounded locations. Snow melt causes a coherence loss due to a complete change in the nature of the backscattering target (e.g. Strozzi et al., 1999; Antonova et al., 2016). Therefore, such a consistent coherence drop is potentially a better indicator of melt onset, since backscatter intensity exhibited a variability in the timing of its deviations from the stable stage, and, moreover, deviations were both positive and negative. It is also possible that the prominent backscatter intensity drop was rather caused by water ponding on the snow or ice surface than by snow melt. Antonova et al. (2016) showed a minor backscatter increase (max. 3 dB) over terrestrial landscape units for the same TSX dataset for the snow melt period of 2013 and related this increase to the rough crust formation on the snow surface due to melt and refreeze cycles. Since backscatter for deep locations over the same time period showed a significant drop (3–8 dB), we hypothesize that this drop was caused by water ponding on the ice surface and expand this hypothesis to the following years as well. Some studies indicated that meltwater ponding does not affect floating ice as much as grounded ice due to water percolation through the ice column and lateral water drainage off the floating ice (e.g. Arp et al., 2015). Nonetheless, it is reasonable to assume that the observed backscatter drops in our study are too large to be only related to snow melt. In the ice season 2012–2013, the assumed water ponding on the lakes surface coincided with a strong coherence drop (24 April–5 May). In the ice season 2013–2014, a drop in coherence was not observed due to generally low coherence over the entire winter season. In 2014–2015, a strong drop in coherence occurred earlier (1–12 May) than the strong backscatter drop associated with possible water ponding (23 May–3 June). Although coherence appears to be more robust for the detection of melt onset than TSX backscatter, its use is limited to the shallow lakes characterized by bedfast ice.

3.6.2.3 Water-Clear-of-Ice

Water-clear-of-ice was mainly detected by visual inspection of the backscatter intensity images, which featured open water with low backscatter. Estimated ice-off dates with TSX are within the range of those obtained with CLIMo (Table 9). In 2013–2014, ice-off was about two weeks earlier than in 2012–2013, and in 2014–2015 ice-off was about one week later than in 2012–2013 (note the uncertainty in the order of 11 days due to TSX revisit cycle). The ice season 2013–2014 featured the thinnest CLIMo simulated ice of all three seasons which could partly explain the earliest ice-off date in this year.

The temporal resolution of TSX (11 days) is rather coarse for the ice phenology monitoring (Duguay et al., 2002). However, for remote Arctic sites where in situ observations are very sparse and rare, and optical imagery is strongly affected by clouds and limited daylight, the TSX revisit cycle can still be useful. Using TSX images from different orbits can significantly improve temporal coverage, but this complicates the method as one must take into account different acquisition geometries. SAR data from recently launched Sentinel-1 satellites with their revisit cycle of 6 days can significantly improve temporal resolution for the repeat-pass SAR monitoring of lake ice phenology.

3.7 Conclusions

The main goal of this study was to examine the potential of a unique X-band SAR dataset to monitor ice phenology and bedfast ice on a number of thermokarst lakes in the Siberian Arctic. Three-year repeat-pass TSX time series with high temporal (11 days) and spatial (10 m) resolution were used. Two different parameters derived from SAR imagery were employed in the analysis: backscatter intensity and 11-day interferometric coherence. In addition, the evolution of ice thickness and dates of ice-on and ice-off were simulated using the lake ice model CLIMo. Ground-truthing based on field measurements of ice thickness was available from 14 locations during the late winter (13–20 April) of the last year of time series. The following conclusions can be drawn from this study:

- Ice phenology stages, such as (i) the onset of freezing as well as ice thickening, (ii) the onset of surface melt, and (iii) the date of complete ice-off condition

were generally tracked by TSX backscatter intensity time series. Dates of ice-on and ice-off were in range of those simulated by CLIMo. The onset of the surface melt was marked by a strong drop in coherence, which was more time-consistent for different locations than changes in backscatter intensity.

- Lake ice grounding was well detected by a prominent drop in TSX backscatter intensity in winter. Most of the field measurements confirmed the TSX-derived separation between floating and bedfast ice. An increase in interferometric coherence was observed for grounded ice for two of the three ice seasons, confirming the detection of bedfast ice. The gradual increase of coherence occurred typically later than the backscatter drop, probably reflecting the freezing of lake sediments.
- The high temporal resolution of the TSX time series (compared to previous satellite-based SAR studies) generally improved the extraction of the timing of ice grounding. However, we encountered some difficulties in the timing extraction, which are likely related to (i) a mixed signal from both floating and grounded ice within the ROI and (ii) propagation of the freezing front into lake sediments which affects SAR signal return.
- Using the timing of ice grounding and simulated ice thickness we obtained the water depth at grounded ice locations where in situ ice thicknesses were available. Comparison showed a reasonably good agreement in the year of field measurements and a larger difference in the previous two years.
- Both ice phenology and ice grounding revealed interannual variability, most likely due to a difference in climatic conditions and water levels between the years.
- The high spatial and temporal resolution of TSX imagery allows monitoring the progression of the ice grounding for an entire lake which could be used for lake bathymetry extraction in future. Furthermore, the high coherence observed over the shallow lakes indicates that the bathymetry of these lakes could be derived with SAR interferometry in future studies.

Acknowledgments

We thank anonymous reviewers for their valuable comments which helped to improve the manuscript. We thank the German Aerospace Center DLR and Achim Roth for invaluable help with the data access. We also thank Homa Kheyrollah Pour for the running CLIMo, Grant Gunn for valuable discussions and Sina Muster for the critical reading of the manuscript. We are grateful for the assistance in the field from Niko Bornemann and the support of the research station “Samoylov Island”. This research has been conducted partly with the support of the Helmholtz Alliance HA310 ‘Remote Sensing and Earth System Dynamics’ and partly with DAAD (German Academic Exchange Service) scholarship (Kurzstipendien für Doktoranden 2015/16 (57044996)) to S. Antonova. This research was also supported by a Discovery Grant from the Natural Sciences and Engineering Council of Canada (NSERC) to C. Duguay. A. Kääb acknowledges support by the European Research Council under the European Union's Seventh Framework Programme (FP/2007–2013)/ERC grant agreement no. 320816, and A. Kääb and S. Westermann by the ESA DUE GlobPermafrost project (4000116196/15/IN-B).

4

Permafrost thaw subsidence in the Lena River Delta, Siberia, measured in situ and estimated from TerraSAR-X interferometry.

Abstract

Extensive field measurements of ground displacement due to melt and refreeze of ground ice were conducted in the Lena River Delta, Siberian Arctic, in 2013-2015. They showed seasonal subsidence of 1.7±1.5 cm in the cold summer of 2013 and 4.8±2 cm in the warm summer of 2014. Stronger subsidence in summer 2014 led to a pronounced interannual subsidence of 4.4±2.6 cm, measured in spring 2015 relative to the initial measurements in spring 2013. Subsidence was highly variable spatially at the sub-meter scale. Differential Synthetic Aperture Radar interferometry (DInSAR), most often used to measure ground displacement caused by tectonic or volcanic processes, is adapted now for the detection of vertical ground motion related to permafrost thaw. This study tests the viability of TerraSAR-X (TSX) data for the detection of such thaw motion. Of two years of TSX data (2012-2014) only data from summer 2013 (mostly 11-day interferograms) maintained sufficient interferometric phase coherence. Our TSX DInSAR stack generally showed only a slight subsidence, however, in an order of magnitude less than that, measured in situ. High spatial variability of subsidence observed in the field poses a challenge to DInSAR as a method for an accurate representation of thaw subsidence. In this paper we thus also discuss the possible consequences of such local scale variability

on DInSAR results and meaningful measures towards more robust thaw subsidence estimations using space-borne SAR.

4.1 Introduction

Permafrost is one of the elements of the cryosphere, next to ice sheets, glaciers, sea ice and snow cover. In the northern hemisphere, permafrost occupies up to 18% of the land area (Zhang et al. 2000) and its depth reaches up to 1500 m below the land surface in particular areas of Eastern Siberia. In permafrost lands, the active layer is the upper layer of the ground which thaws and freezes seasonally. A fully water-saturated active layer in summer increases in volume during freezing in winter (about 9% for fresh water) due to the decrease in density of ice compared to water (Lide, 2005). Cycles of excess ice formation in winter and loss in summer result in seasonal vertical movements of the ground in both directions, notably frost heave and thaw settlement (or subsidence). The magnitude of these movements depends on the ice/water content and distribution in the active layer. Measuring the magnitudes of these movements can in turn aid in estimation of ice/water content, which is one of the most important ground variables for permafrost modeling (Langer et al., 2013). Active layer thawing typically takes a few months, starting when the surface becomes free of snow in spring surface until the beginning of freezing in the fall.

Shiklomanov et al. (2013) introduce the term isotropic thaw subsidence in order to determine a phenomenon of relatively uniform and irreversible thawing of the ice-rich layer typically found at the upper surface of the permafrost. Isotropic thaw subsidence is, thus, different from rather rapid and confined thermokarst or thaw slump ground subsidence. They show that due to such isotropic subsidence the record of active layer thickness in Alaska does not demonstrate a clear increasing trend, which was expected as a result of the effect of global warming in the Arctic. Accounting for the isotropic subsidence is, therefore, necessary for the accurate representation of the active layer thickness dynamics on the long term.

Reported in situ measurements on subsidence in permafrost areas include repeat differential global positioning system (DGPS) measurements of the ground surface vertical position (e.g. Little et al., 2003; Shiklomanov et al., 2013; Beck et al., 2015),

Linear Variable Differential Transformer (LVDT)-based measurements (e.g. Harris et al., 2007; Akagawa et al., 2012) and thaw-tubes (e.g. Nixon et al., 2003; Short et al., 2014). Field campaigns for installation of the equipment and conducting measurements are expensive and do not provide good spatial coverage. However, such measurements provide the most reliable information on ground subsidence and are important for the remote sensing validation.

Ground motion detection over permafrost regions by using remote sensing methods is advantageous due to large spatial coverage and avoidance of expensive field campaigns. Related methods include differencing of multitemporal Digital Elevation Models (DEM) (e.g. Günther et al., 2015) and repeat-pass differential SAR interferometry (DInSAR). This technique uses the phase difference of two radar signals acquired at two dates over the same area to measure ground displacement. It is applied widely and successfully, for instance, for detecting ground displacement associated with earthquakes and volcanic eruptions (e.g. Massonnet et al., 1993). Recently the method has been used for monitoring permafrost thaw subsidence and frost heave. For instance, Rykhus & Lu (2008) observe seasonal thaw subsidence of about 2-5 cm on the Alaskan North Slope using JERS-1 L-band SAR data. Liu et al. (2010) use ERS-1/2 SAR data and report about 1-4 cm of both seasonal and decadal subsidence on the North Slope. Short et al. (2011) identify seasonal subsidence up to 15 cm at an instable and eroding coastal part of Herschel Island, Canada using TSX data, supported by RADARSAT-2 data. They also detected long-term subsidence of 10-20 cm per year using RADARSAT-2 and ALOS-PALSAR data. Strozzi et al. (2012) report seasonal subsidence on the order of 4 cm using TSX data over the North Slope of Alaska. Ground-truth measurements were typically absent for these InSAR studies.

The applicability of InSAR over permafrost regions is limited, however. The interferometric phase decorrelates for surfaces that change through time, which causes a loss of interferometric signal. This phase decorrelation generally increases with shorter radar wavelength and with increasing time period spanned by the interferograms. For instance, Beck et al. (2015) test TSX data (X-band, wavelength 3.1 cm) to measure vertical ground movements in the Canadian subarctic and report very low phase coherence over the areas of interest. Short et al. (2011) compare TSX,

RADARSAT-2 and ALOS-PALSAR interferograms over Herschel Island, Canada and show the suitability of C- and L-band to form one- and multiyear interval interferograms, whereas X-band could be used only for the seasonal subsidence detection.

An explorative study of 11-day sequential coherence time series of TSX data in the Lena River Delta, Siberia demonstrated the large spatial and temporal variability of coherence during the year 2012-2013 (Antonova et al., 2016). However, some single interferograms showed sufficient coherence to test their potential for ground displacement detection. Here we perform differential interferometry on these TSX data in order to assess its viability for the thaw subsidence detection on a yedoma upland of the Lena River Delta. Results are compared to field measurements made between 2013 and 2015.

4.2 Study area

The Siberian Lena River Delta (73 °N; 126 °E) is comprised of more than 1500 islands of various sizes and has an area of about 30 000 km² (Fig. 26a and 26b). It is located in the zone of continuous permafrost, with permafrost depth reaching up to 600 m (Grigoriev, 1960). The climate of the region is generally characterized by long and extremely cold winters and short, cool summers, with mean February temperatures of -33.1 °C and mean July temperatures of 10.1 °C over the last decade (Boike et al., 2013). The absence of glaciation during the Pleistocene as well as cold air temperatures in the past and present result in low permafrost temperatures compared, for instance, to Svalbard or Alaska, with temperatures of about -9 °C at the depth of zero annual amplitude (Boike et al., 2012). Snow accumulation typically begins in September and snow melt begins in May and takes less than a month to melt completely. Snow depth is highly variable due to microtopography and wind redistribution, but usually does not exceed a few decimetres. The active layer usually begins to thaw in the first half of June, reaching a thickness of about 50 cm on average. Freezing of the active layer commences with the onset of negative air temperatures and is usually already completed in November (Boike et al., 2013).

We focused in particular on Kurungnakh-Sise Island (translated to “an island of an old dry bone”, from the Yakut language) in the southern part of the Delta, which

represents largely the remnants of late Pleistocene accumulation plain (Fig. 26b and 26c). Stratigraphically, the island consists of 15-20 m thick fluvial silty sands overlain by up to 40 m thick ice-rich peaty and silty deposits, also known as yedoma or Ice Complex. The ground ice in these deposits is represented in forms of small ice veins and lenses as well as giant ice wedges, which can reach up to 20 m height and several meters wide. The Holocene layer on the very top can be as thin as 0.5-1 m and features peaty soils interbedded with silty sands (e.g. Grigoriev, 1993; Schirrmeister et al. 2003; Wetterich et al., 2008).

The relief of the island is largely a result of permafrost degradation processes that started in mid-Holocene, and characterized by thermo-erosional valleys and thermokarst basins, which occupy about 40% of the island area. The upland is characterized by polygonal tundra with small ponds and thermokarst lakes. The maximum relief height of the island is 55 m a.s.l. and the mean elevation gradually decreases from southeast to northwest, which has led to the development of a drainage network (Morgenstern et al., 2011). Relict bedrock islands with elevations of about 50 m are present in the area as well (Fig. 26c). The region is characterized by typical tundra vegetation, which includes sedges, grasses, dwarf shrubs and well-developed moss layer.

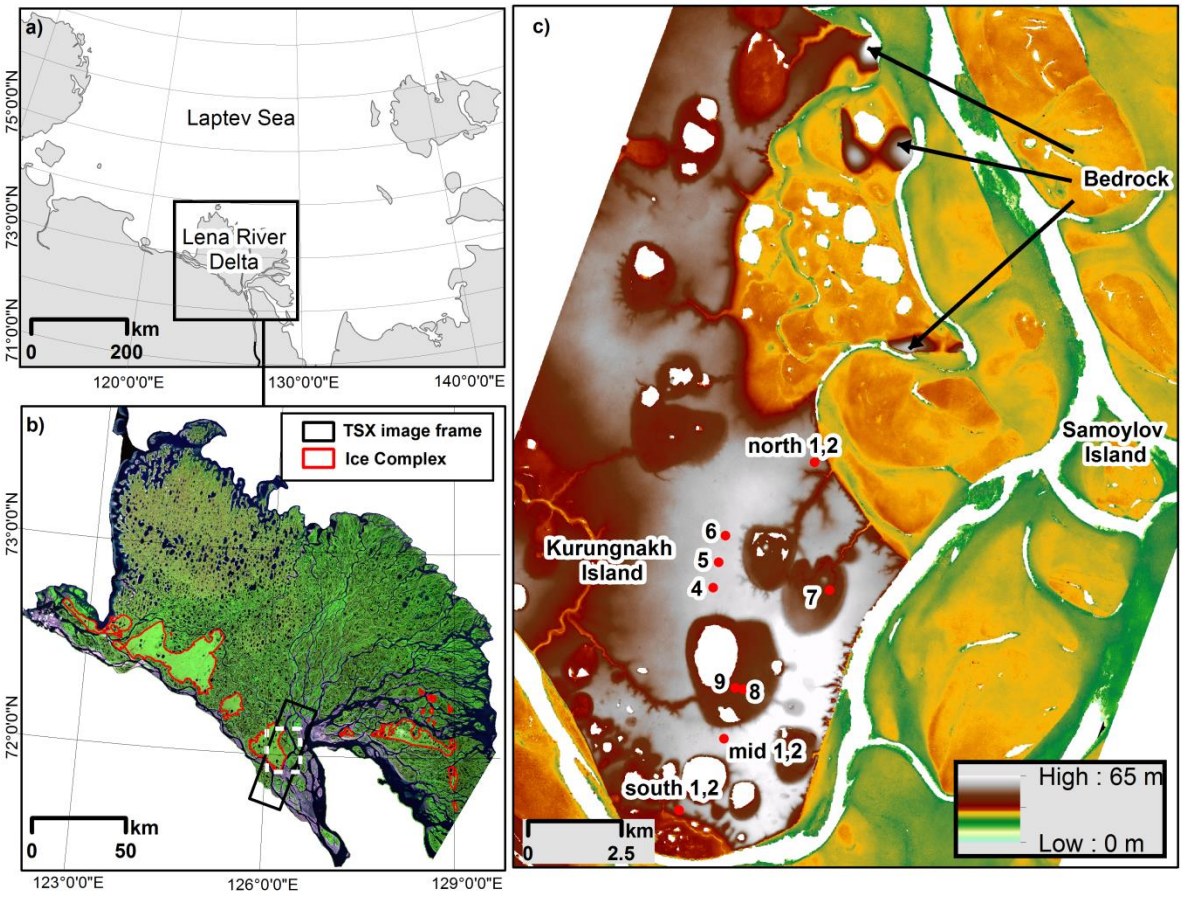

Figure 26. Study area: a) Laptev Sea region and the Lena River Delta with the black square delineating the area shown in b); b) Lena River Delta on Landsat 7 ETM image (RGB 6-4-2) with Ice Complex delineated in red (Morgenstern et al., 2011), TSX image frame delineated in black and the area shown in c) delineated in dashed white; c) TSX DEM, derived in this study with locations of in situ measurements on Kurungnakh Island depicted by red dots. Locations where bedrock exists on the surface are also indicated.

4.3 Data and Methods

4.3.1 Field measurements of surface displacement

4.3.1.1 Metal pipes (2013-2015)

Surface displacement was determined by repeated measurement of the distance between the top of a steel pipe and a plexiglas plate resting on the ground surface (Fig. 27a). The pipe is 2 m long and 3 cm in diameter and anchored at least 1 m below the active layer. We assume that the pipe is motionless relative to the permafrost. The plexiglas plate is fixed in its horizontal position by the metal pipe,

but can move freely with the surface vertically along the pipe. Several distance measurements around the pipe were taken at each visit and averaged. Altogether 12 pipes were installed on Kurungnakh Island in April 2013 (Fig. 26c). Measurements were conducted during field campaigns in spring 2013 (April, 25-30), summer 2013 (July, 14-19 and August, 24-28), spring 2014 (April, 22), summer 2014 (August, 5-7 and August, 22-23) and spring 2015 (April, 11).

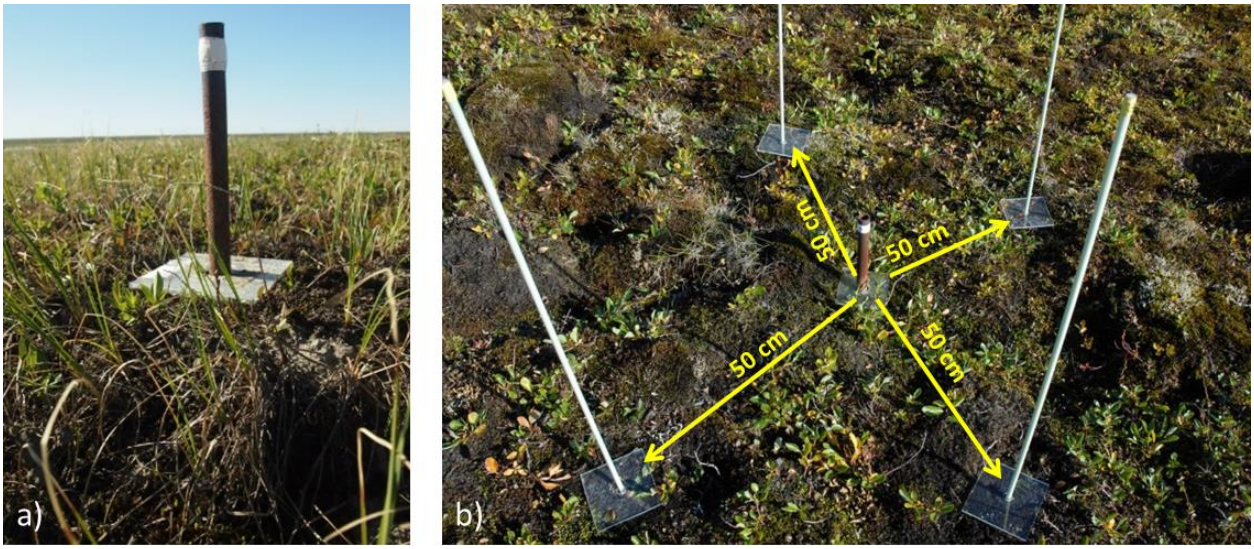

Figure 27. a) Example of a measurement site with a metal pipe set-up; b) example of a measurement site with fiberglass rods arranged around a metal station (station 9, August 2014). Distance from each fiberglass station to the metal station is about 50 cm.

4.3.1.2 Fiberglass rods (2014-2015)

19 fiberglass rods, which are 2 m long and 1 cm in diameter, were installed in spring 2014. Following the method for the metal pipes, they were drilled at least 70 cm below active layer, and outfitted with plexiglas plates. To detect the small-scale spatial variability of displacements and to compare the effect of two different materials, these stations were installed nearby the locations of metal pipes. Four fiberglass poles were added around each of the metal stations 7, 8 and 9 (Fig. 27b). The radius between metal station 7 and fiberglass rods was 1 m, and the radius between stations 8 and 9 and their fiberglass rods was 50 cm. In addition, a transect of seven fiberglass stations was installed between metal stations 8 and 9 with approximately 25 m intervals between stations. Measurements were conducted

during field campaigns in spring 2014 (April, 22), summer 2014 (August, 5-7 and August, 22-23) and spring 2015 (April, 11).

4.3.1.3 Sources of potential errors in field measurements

Installation of metal pipes and fiberglass poles via deep drilling could have affected the state of permafrost and active layer to some extent. Moreover, the high thermal conductivity of metal could potentially induce additional warming and cooling of the ground. However, visual inspection of the stations conditions during three summer seasons did not reveal any drastic changes (e.g. water ponding) of the tundra surface around the pipes. Therefore, we assume no significant and systematic error source in the station setup. No difference between the steel pipe and fiberglass sites were observed, although they differ significantly in thermal conductivity (40 and 0.04 W/mK, respectively).

Other potential uncertainties are inherent in the method to obtain manual distance measurements. For example, the plexiglas plate can be pushed down into vegetation and moss layer with different pressure, which is hard to control. Moreover, the presence of vegetation under the plate is itself an additional source of error, especially in case of vascular plants, which can grow under the plate, lifting it up seasonally to some extent. Overall, we assume ±1 cm as a reasonable measurement uncertainty.

4.3.2 SAR data and processing

TSX is a SAR satellite launched in 2007, operating with the X-band (wavelength 3.1 cm, frequency 9.6 GHz). The SAR time series acquired for this study includes 65 Single-Look Slant Range Complex (SSC) images taken between August 2012 and September 2014 in StripMap imaging mode. The time span between the used acquisitions was 11 days, with a few exceptions when the time span was 22 days. The local time of acquisition was 08:34 (22:34 UTC). The chosen orbit was in descending overpass and the radar was right-looking. The acquisition incidence angle was approximately 31^0 and the polarization was HH for all images. The slant range and azimuth pixel spacing were approximately 0.9 and 2.4 m, respectively. The scene size covered an area of approximately 18 x 56 km (Fig. 26b).

The data was processed using the Gamma radar software (Werner, 2000). The SSC data was converted to Gamma Single Look Complex (SLC) format and the SLC data were then consecutively co-registered with subpixel accuracy (typically better than 0.2 pixels) in such a way that the co-registered slave image became the master for the next image. The co-registered SLC data was multi-looked by factors of 4 and 3 in range and azimuth directions, respectively to reduce phase noise and obtain roughly square ground range pixels. Subsequently, 11-day (or 22-day in case of a gap) interferograms were computed with common band filtering and removal of the curved Earth interferometric phase trend (flattening).

The interferometric phase includes geometric phase terms due to surface topography and non-zero baselines between image acquisitions, noise terms due to atmosphere and surface changes on the ground, and a phase term introduced by surface displacements. To remove the geometric phase term and generate differential interferograms, a DEM is needed. A high quality DEM for our study area was not available (i.e. SRTM is not available for high latitudes and the TanDEM-X DEM was not yet available during the time of this study). Instead, we estimated the local elevation from one interferogram included in the used data set (4-pass DInSAR method). This chosen topographic interferogram should not include surface displacement and should have a large orbital baseline to increase sensitivity to the topographical phase. Acquisitions from February 6 and February 17 in 2013 were chosen to satisfy the requirements. This data was taken during winter, and thus any dynamic ground displacement was excluded. A perpendicular baseline was about 117 m. For the DEM generation the flattened topographic interferogram was filtered and unwrapped using a branch-cut region growing algorithm, with supervised bridging of the phase values to cross decorrelated areas over river arms. A refinement of the baseline was done using ground control points obtained from a DEM based on optical ALOS PRISM data (Günther, 2009).

A requirement for ground displacement measurements by using DInSAR is a certain stability of ground conditions, meaning that closely-spaced scatterers contributing to the return signal do not move significantly with respect to each other. The back-scattered signal of a pixel is the vector sum of the amplitude and phase contributions of all scatterers within a pixel (here, about 35 m by 35 m after multi-looking). For a

consistent move of the scatterers, the interferometric phase changes in the line-of-sight (LOS) of the radar as shown in (7), where R is the distance to the satellite and λ is the wavelength of the radar signal.

$$\varphi = \frac{4\pi R}{\lambda}, \qquad (7)$$

Due to the periodicity of the phase, only small LOS changes less than λ/4 (here, ±0.78 cm of vertical motion), can unambiguously be inferred from the interferometric phase. This limit is a phase smoothness requirement such that the combined average phase change for the pixel is a meaningful average phase change to be related to displacement.

The more similar or smooth the phase changes are, the more stable the interferometric phase in time and space, which is commonly quantified by the interferometric coherence. Interferometric coherence, γ, is defined as the cross-correlation coefficient between two SAR images s_1 and s_2 as shown in (8).

$$\gamma = \frac{\langle s_1 s_2^* \rangle}{\sqrt{\langle |s_1|^2 \rangle \langle |s_2|^2 \rangle}} \qquad (8)$$

It is a measure of phase stability over time; however, there is an assumption on ergodicity for the coherence, and therefore the averaging is performed over a spatial window (3 x 3 pixels in this study). High phase coherence means that neighbouring pixels show small phase variations, and therefore maintain stable ground conditions. Thus, phase coherence is an important measure of data quality.

In a precursory study, Antonova et al. (2016) demonstrated large temporal and spatial variability of 11-day interferometric coherence for a part of the TSX dataset used in the present study (2012-2013). Poor coherence was found for many of the pairs; however, eight sequential interferograms from June to September 2013 demonstrated coherence levels, acceptable for interferometry. Also, based on the long-term observations in the study area, it was assumed that this time period captured the exact period of thawing and possible subsidence. Therefore, further analyses with the aforementioned eight interferograms were carried out. Interferograms for the summer period of 2014 were also produced. However, the

coherence was too low for half of the interferograms, making further analyses difficult.

Hence, eight differential interferograms for the summer of 2013 were produced using the derived interferometric DEM. To reduce the noise further, an additional multi-looking step with a factor of 5 in both range and azimuth directions was applied to the interferograms. The differential interferograms were then filtered to enable unwrapping with an adaptive filter based on local fringe spectrum (Goldstein and Werner, 1998).

Assuming a range change smoothness for neighboring pixels in the interferogram (i.e. relative movement of less than $\lambda/4$), the smoothness requirement outlined above for scatterers within the pixels can be somewhat relaxed. As a result, the average range change of scatterers within the pixel can be much more than $\lambda/4$, if the phase changes within the pixel do not vary by more than $\lambda/4$. In this way, spatially smooth increasing displacements is inferred in so-called spatial phase unwrapping. Phase unwrapping was performed using a branch-cut algorithm and a seed point was chosen on a stable bedrock surface. Unwrapping was done only on the Kurungnakh Island, which features a relatively homogeneous upland, without further unwrapping across the river arms. The unwrapped phase was then converted to displacement. Displacement is assumed to be purely vertical, and therefore the LOS displacement (d_{LOS}) was converted to vertical displacement (d_{vert}), based on the incidence angle (θ) as shown in (9).

$$d_{vert} = \frac{d_{LOS}}{\cos(\theta)}, \qquad (9)$$

The individual interferograms were affected by atmospheric noise (see Appendix, Fig. A6). In order to enhance the displacement signal and reduce atmospheric noise, all eight single interferograms were summed up in a time-continuous stack.

4.4 Results

4.4.1 Field measurements of ground displacement

4.4.1.1 Seasonal subsidence

Measurements in April 2013 and 2014 provided the reference winter surface positions and we compared the summer measurements from the end of August 2013 and 2014 with these references to calculate the seasonal subsidence (Fig. 28a). Metal stations in late August 2013 showed variable displacement relative to the winter reference with an average value of 1.7±1.5 cm. In August 2014, the same stations showed stronger subsidence relative to the winter reference with an average value of 4.6±1.6 cm. In August 2014, 19 fiberglass rod measurements were available in addition to the measurements from metal pipes (Fig. 28b). A well pronounced subsidence relative to the winter reference with an average value of 4.9±2.2 cm was observed, which is very similar to the measurements from metal pipes for the same time period.

It should be noted that observed subsidence by the end of August is not maximal, because additional subsidence could take place by the end of the thawing period, which typically occurs in the middle or the end of September.

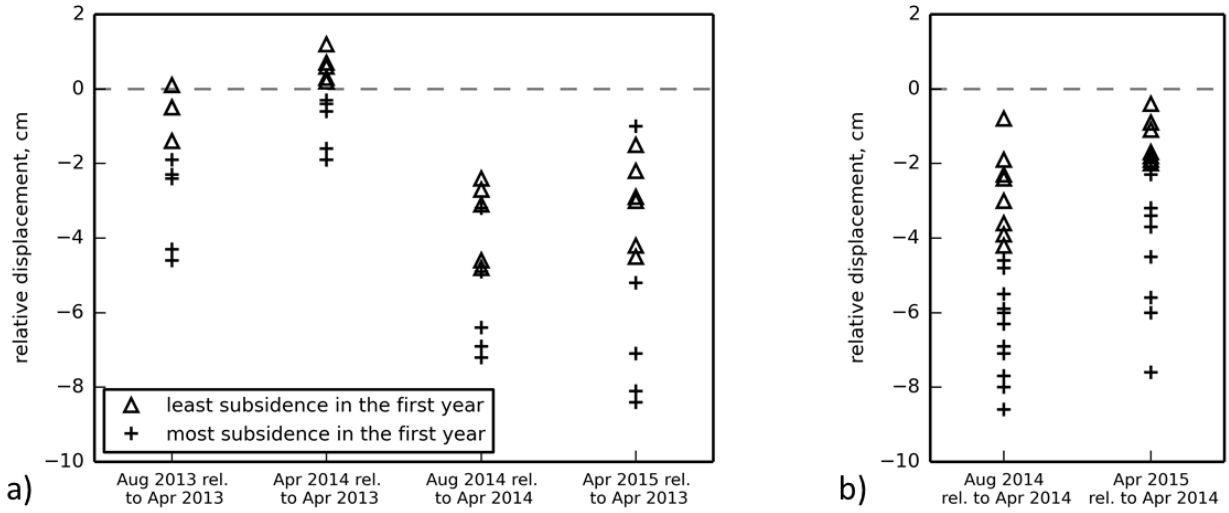

Figure 28. a) Seasonal and interannual displacement measured from 2013 to 2015 with metal pipes (each symbol marks a station). Measurements are grouped (triangles and crosses) based on the subsidence magnitude in 2013; b) seasonal and interannual subsidence measured in 2014 and 2015

with fiberglass rods. Measurements are grouped (triangles and crosses) based on the subsidence magnitude in 2014.

4.4.1.2 Interannual displacement

One-year and two-year displacements were derived from metal station measurements in April 2014 and 2015 relative to the initial measurements carried out in April 2013 (Fig. 28a). In April 2014, approximately half of the stations demonstrated relative heave (up to 1.2 cm) and another half demonstrated relative subsidence (up to 1.9 cm). Measurements in April 2015 revealed a pronounced subsidence relative to April 2013 for all stations characterized by an average value of 4.4±2.6 cm. Additional measurements from fiberglass rods in April 2015 showed a well pronounced one-year subsidence relative to April 2014, characterized by an average value of 2.9±1.9 cm (Fig. 28b).

The grouping of measurements demonstrated a consistent tendency for displacement. More specifically, stations showing the least amount of subsidence at the start of the measurements maintained weaker subsidence (or stronger heave) in the following years, whereas stations showing stronger subsidence at the start of the measurements maintained stronger subsidence in the following years.

4.4.1.3 Spatial variability

The spatial variability of subsidence on different scales was investigated using sets of stations with different spacings between them (see Data and Methods). Figure 29a shows the variability of subsidence measured at each of the station sets (7, 8, 9) and along the transect in late August 2014 (relative to April 2014). Station sets 7 and 9 demonstrated the most consistent subsidence magnitude with average values of 7.3±0.9 cm and 5.3±1.2 cm, respectively. Station set 8, however, showed a wider range of subsidence values, with the average being 4.9±2.4 cm. The transect showed a range of subsidence values, characterized by an average value being 2.9±1.3 cm.

Besides, measurements from metal stations showed subsidence values similar to those from fiberglass stations. Although fiberglass stations are characterized by a much lower thermal conductivity and are thinner in diameter than steel pipes, there appears to be no difference between metal and fiberglass materials in terms of performance for displacement measurements.

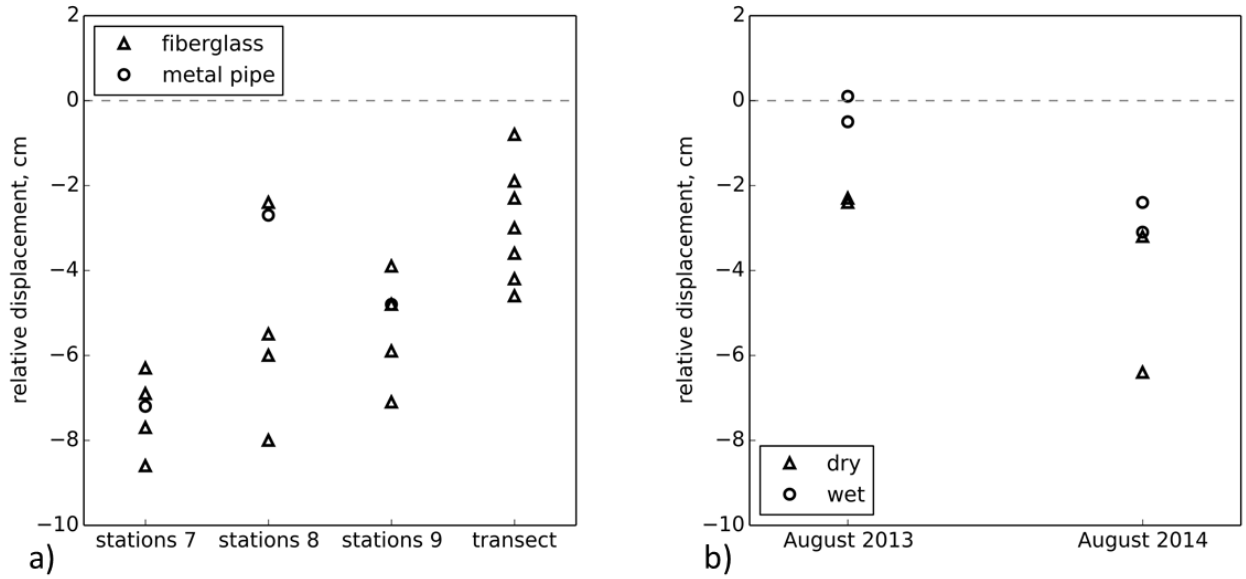

Figure 29. a) Spatial variability of seasonal subsidence measured in late August 2014 (relative to April 2014) on different scales: station sets 7, 8 and 9 are spaced 1 m or 0.5 m within each group and the transect consists of seven stations spaced about 25 m from each other; b) seasonal subsidence measured in August 2013 and August 2014 at four sites, two of which were dry and another two were wet.

Additionally, two pairs of metal stations (mid 1 and mid 2; south 1 and south 2, see Fig. 26c) were installed in the vicinity of each other in 2013, with an approximate spacing of 5 m within each pair. Local topography and surface conditions were distinctly different for each station within a pair. More specifically, mid 1 and south 1 were located on a relatively dry surface with little vegetation, whereas mid 2 and south 2 were located in wet depressions with more grass. Figure 29b shows relative seasonal displacement for these four stations in 2013 and 2014. In late August 2013, stations mid 1 and south 1 showed subsidence of 2.3 and 2.4 cm respectively, whereas stations mid 2 and south 2 showed almost no displacement. In mid-August 2014, all four stations showed a pronounced subsidence. However, one of the dry sites showed approximately 3 cm more subsidence than wet sites.

4.4.2 DInSAR

Figure 30a shows the sum of eight summer interferograms from June to September 2013. Generally, only minor displacements are detected for most of the island. A slight downward motion was present in some of the thermokarst basins.

Furthermore, a slight upward motion was present in the northernmost area of the island. To better understand the distribution of displacement values, we generated a histogram (Fig. 31). Most of the displacement values had a negative sign, which indicates a downward motion (i.e. subsidence), expected over the thawing season in summer. However, the subsidence mostly did not exceed 1 cm.

To compare DInSAR results with field measurements, we plotted the 2013 field measurements on top of the TSX displacement maps. The first graphic (Fig. 30b) is the sum of four interferograms (June 6 to July 21) with in situ measurements made between July 14-19. The second graphic (Fig. 30c) is the sum of six interferograms (June 6 to August 23) with in situ measurements made between August 24-28. Apparent is the significant underestimation of DInSAR-derived subsidence compared to the measured in situ subsidence. Table 10 shows the difference between DInSAR-derived and in situ measured displacement in summer 2013.

Table 10. DInSAR-derived and in situ measured displacement in summer 2013 (two periods) (negative values represent subsidence, positive values represent heave).

station	DInSAR (6 Jun-21 Jul), cm	In situ (14-19 Jul), cm	DInSAR (6 Jun-23 Aug), cm	In situ (24-28 Aug), cm
north 1	0.3	-1.4	-	-
north 2	0.3	-0.1	-	-
6	0.3	-0.8	-0.1	-1.9
5	0.3	-2.2	-0.1	-4.6
4	0.2	-1.5	-	-
7	0.2	-4.3	-	-
8	0.1	0.4	-0.3	-0.5
9	0.3	-0.5	0	-1.4
mid 1	0.4	-0.2	0.2	-1.8
mid 2	0.4	0.1	0.2	-0.4
south 1	-	-1.4	-	-2.4
south 2	-	0.4	-	0.1

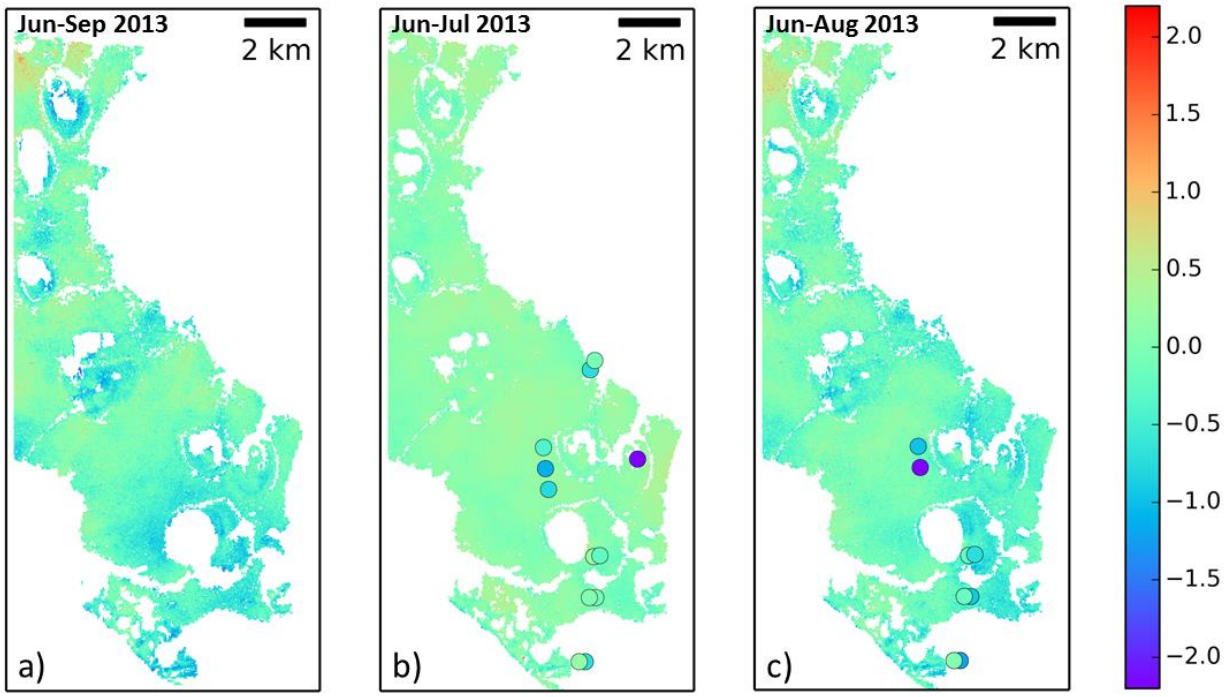

Figure 30. Summer displacement maps (in cm) from DInSAR stacks over the Kurungnakh Island of a) all summer interferograms from June to September; b) interferograms from June to July with April-July field measurements (colored circles); c) interferograms from June to August with April-August field measurements (colored circles).

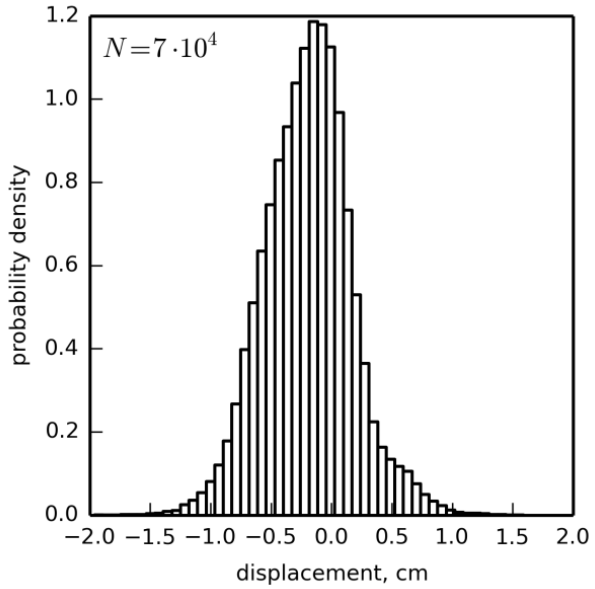

Figure 31. Histogram of TSX DInSAR cumulative displacement values for summer 2013 (June-September).

4.5 Discussion

4.5.1 Field measurements

Two summer seasons (2013 and 2014) clearly demonstrated different seasonal subsidence magnitudes with average values of 1.7±1.5 cm in 2013 and 4.8±2 cm in 2014. This difference can logically be attributed to the difference in climatic conditions of these two summer seasons. Based on air temperatures measurements from a meteorological station nearby (http://rp5.ru/Weather_archive_on_Stolb_Island), we calculated the square root of thawing degree days index (TDD) for the last decade (Fig. 32). This index is the sum of daily air temperatures of each day of a year with temperatures > 0 °C. Clearly, 2013 was the coldest year of the last ten years, which explains the weaker seasonal subsidence than in 2014. These different summer preconditions also led to different patterns of interannual displacement. More specifically, winter 2014 (after the cold summer of 2013) demonstrated both uplift and subsidence relative to the winter 2013 reference and winter 2015 (after the warm summer of 2014) showed clearly defined subsidence relative to the winter 2013 reference.

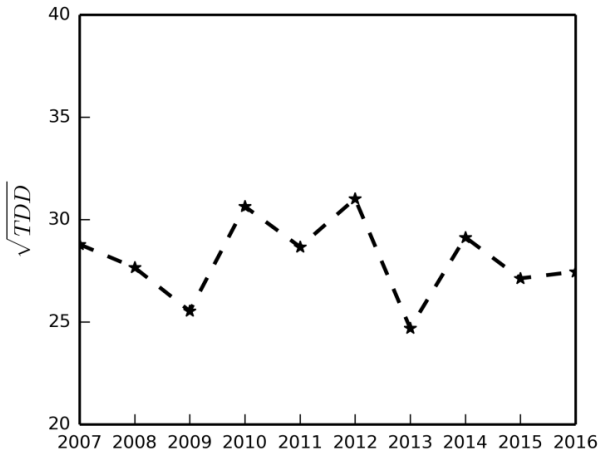

Figure 32. Square root of thawing degree days index (TDD) calculated from daily averaged air temperatures from a nearby meteorological station (http://rp5.ru/Weather_archive_on_Stolb_Island) for the last decade.

In general, stations which showed uplift between winters 2013 and 2014 had less potential to subside deeper during the following summer season compared to the stations that showed net subsidence between winters 2013 and 2014. This was reflected in weaker net subsidence for the first group of the stations between winters 2013 and 2015 compared to the second group. However, the warm summer of 2014 induced enough thaw to provoke a subsidence strong enough such that subsequent frost heave could not exceed the subsidence of the previous year. Considering that only two years of the past decade were relatively cold (2009 and 2013), it is likely that the net subsidence accumulates from year to year, because there have been insufficient cold years to reverse or significantly slow down subsidence.

Studies from Alaska over longer time periods confirm our observations. Streletskiy et al. (2016) continued repeat DGPS measurements from Shiklomanov et al. (2013) and reported a net average subsidence of up to 15 cm for the period 2003 to 2015 in Barrow. They associated the observed net subsidence with increasing air temperatures and consequent thawing of the ice-rich layer at the permafrost table. Günther et al. (2015) used the difference between DEMs from 1951 and 2013 to estimate the long-term ground subsidence on Muostakh Island (southern Laptev Sea). The Ice Complex deposits on Muostakh Island have the same origin as the Ice Complex deposits in our study area. Günther et al. (2015) found an average net

subsidence of 3.6±1.8 m over 62 years, providing undeniable evidence of irreversible long-term ground ice melt. Particularly, they indicated that the subsidence was not uniform over the island, but varied depending on geomorphology. For example, areas close to eroding coastlines subsided twice as fast as the rest of the island.

In our study, subsidence measurements also demonstrated high variability on different spatial scales. In 2013, seasonal subsidence (spring to fall) varied from 0 to 4.6 cm for sites separated by a few kilometers. Smaller site separation distances on the order of a few meters showed that the subsidence depended on the local microtopography and thus a location's relative wetness. More specifically, two dry sites showed greater subsidence when compared to two wet sites, which featured almost no displacement. A possible explanation is that there is a larger energy loss for evapotranspiration at wet sites, whereas at dry sites energy is primarily used for thaw deepening. However, the difference between wet and dry sites was only partly sustained in summer 2014. During this season, both wet sites experienced the same amount of subsidence as one of the dry sites, while the other dry site subsided twice as deep. It is possible that higher air temperatures recorded in summer 2014 allowed for deeper thawing, thus, dominating over relative surface wetness effects.

The installation of a number of additional stations in 2014 allowed us to detect spatial variability on a small scale. Within a 0.7-1.4 m spacing, seasonal subsidence in 2014 varied as little as by 2.3 cm (station set 7) and as much as by 5.6 cm (station set 8). Shiklomanov et al. (2013) investigated the scale of maximum variability of subsidence as well. They observed the maximum variability at separation distances of 30 m and greater on the Alaska Coastal Plain, which was attributed to differences between thermokarst basins and upland tundra. The maximum variability at separation distances of 1-3 m at the Alaskan Foothills, whereby this variability was governed by vegetation and frost boils. Overduin and Kane (2006) measured displacement specifically at the frost boils in the Brooks Range, Alaska, between 2001 and 2005. They found higher net subsidence rates at a frost boil centers (5-7.5 cm a^{-1}) compared to the surrounding tundra (2-5 cm a^{-1}) over four years of measurements. The deeper thaw penetration in the boils can be explained by the absence of an insulating organic layer.

4.5.2 DInSAR

The displacement map obtained from a TSX DInSAR interferogram stack for the summer 2013 generally shows minor subsidence and clearly underestimates subsidence by one order of magnitude when compared to in situ measurements. DInSAR displacements were in the range of -1 to +0.5 cm (by mid-September), and the in situ measured displacements were in range of -4.6 to 0 cm (by the end of August). Furthermore, the measurement in summer 2014 showed large variations of subsidence values. The variations were up to 5.6 cm on a meter-scale (Fig. 29a), which is well within the spatial range of a DInSAR pixel (~35 m by 35 m). The in situ field measurements are regarded as the correct representation of subsidence. The latter is not reproduced by DInSAR, and thus the validity of phase smoothness assumptions in time and space made for interferometry needs to be carefully checked.

A possible reason for the discrepancy between field and remotely sensed measurements is that in basic interferometry we measure strictly a LOS wrapped phase change between $-\pi$ to π. From these phase changes, displacement is then inferred based on phase smoothness in time and space (see the SAR data and processing subsection), as well as the assumption that vertical motion needs to be less than 0.78 cm. The high spatial variability in subsidence observed in the field for closely located sites in 2014 could pose a problem with respect to these stability requirements for interferometry.

In 2013, the largest in situ measured subsidence was 4.6 cm between April and the end of August. Assuming the subsidence is linear (although this is most likely not the case in reality) and started at the beginning of June, we obtain a rate of subsidence of approximately 0.7 cm per 11 days of satellite revisit time, which fulfills the phase smoothness requirement in time at this very point. Pixels with a spatial average of subsidence larger than 0.78 cm conflict with the smoothness criterion and create an uplift measurement. However, the phase noise or loss of interferometric coherence for interferograms in summer 2013 was not severe, which suggests that for the majority of the pixels the overall subsidence was small and smooth. In situ measurements in summer 2014 showed much stronger subsidence characterized by

a maximum of 8 cm by the end of August (i.e. approximately 1.1 cm per 11 days). This rate exceeds the phase smoothness threshold of 0.78 cm. Five 11-day interferograms in a row from the end of June to the end of August 2014 showed a strong phase decorrelation. We argue that subsidence could occur faster than 0.78 cm per 11 days during the aforementioned period, leading to decorrelation. A similar finding was reported by Beck et al. (2015). In their study, low coherence was found for TSX interferograms in the Canadian subarctic, and this was attributed to intensive displacement, which exceeded the resolving power of X-band wavelength. Considering that during the last decade, warm years occurred more often than cold years (Fig. 32), it is possible that an appropriate coherence level in our study for the summer of 2013 was an exception. The following years of TSX data (>= 2015) can, however, verify this hypothesis. Also weather conditions should be checked closer in the future to eliminate any possible coherence loss due to environmental / meteorological factors.

Spatial phase unwrapping may be less useful for estimating permafrost subsidence than for the retrieval of long-wavelength continuous surface displacements, such as tectonic movements, where the displacement magnitude is decreasing gradually from an epicenter to margins. There is no evidence of such long-wavelength displacement due to ground ice melt. The melting of ground ice is rather uniform across the area, but with high subpixel variability. To ease spatial unwrapping, we filtered out short-wavelength phase noise, and therefore reduced phase differences between pixels. This might have effectively reduced the relevant small-scale phase signal, while enhancing the strong subsidence underestimation.

It is clear that conventional DInSAR processing might not be suitable for the representation of permafrost thaw subsidence. Instead, a pure phase investigation without high-frequent phase noise filtering and unwrapping could be performed. In this case, atmospheric noise affecting single interferograms can be an obstacle. Possibly, a high-pass phase filtering could overcome this problem. Longer radar wavelengths, such as C-band and L-band, would enable us to unambiguously measure subsidence rates larger than 0.78 cm between two SAR acquisitions (1.4 cm and 5.9 cm, respectively). In addition, shorter revisit times (e.g. 6 days with Sentinel-

1A and Sentinel-1B) would allow us to measure larger subsidence rates for the pixel average.

A number of studies exploited DInSAR to observe thaw subsidence in permafrost landscapes (e.g. Rykhus & Lu, 2008; Liu et al., 2010; Short et al., 2011; Liu et al., 2014; Short et al., 2014). Although these studies reported the successful retrieval of seasonal and interannual subsidence, most of them did not verify their results with in situ measurements. Short et al. (2011) raised the problem of comparison point in situ and areal DInSAR measurements and suggested that the agreement between them might never be achieved. Short et al. (2014) used two thaw-tubes to validate RADARSAT-2 DInSAR results in the Canadian Arctic. Measurements from thaw-tubes represented the spatial variability in subsidence, which was captured by DInSAR qualitatively, but not quantitatively.

For DInSAR, the quality of the DEM used for the removal of the topographic phase is also important. The DEM, obtained from an interferogram from our dataset, is affected by some atmospheric noise which, however, was not visually detected. Therefore, 4-pass interferometry used in our study could potentially be improved by using an independent and high quality DEM. Having the TanDEM-X DEM in the future might verify the DInSAR results of our study. Generally, high spatial resolution of TSX data was neglected in our study due to a need to strongly multi-look interferograms to reduce decorrelation noise. However, field measurements in our study detected variability on a sub-meter scale. Therefore, even single look interferograms (for instance, based on longer wavelength data, and therefore not requiring multilooking) and very high spatial resolution of SAR data (for instance, RADARSAT-2 Spotlight mode with about 1.5 m ground range pixel size) would not solve the problem of spatial inhomogeneity regarding displacement.

4.6 Conclusions

This study contributed to the developing DInSAR estimation of ground displacement related to thawing and freezing processes in permafrost environments. For the first time, numerous field measurements accompanied the permafrost interferometry study. These measurements, performed on the Yedoma uplands in the Siberian Arctic from 2013-2015, detected pronounced seasonal and multi-year net

subsidence. The magnitude of subsidence was related to distinct interannual air temperature variations. An important factor for assessing the viability of DInSAR was the high spatial inhomogeneity of subsidence was observed in situ. Repeat-pass StripMap TSX data was tested for its applicability to detect the in situ observed subsidence. A row of coherent sequential interferograms was available only for the summer 2013. However, interferograms were affected by atmospheric noise. Cumulative displacement generally showed subsidence, but an order of magnitude lower than those measured in situ. We suggest that a possible reason for this inconsistency is the spatial inhomogeneity of subsidence. Thus, conventional DInSAR processing might not be suitable for the accurate representation of permafrost thaw displacement.

Acknowledgements

We would like to thank the German Aerospace Center DLR and Achim Roth for invaluable help with the TSX data access. We also say thank you to Niko Bornemann, Alexander Evdokimov and the research station “Samoylov Island” for field assistance. This research has been conducted with the support of the Helmholtz Alliance HA310 ‘Remote Sensing and Earth System 673 Dynamics’.

Appendix

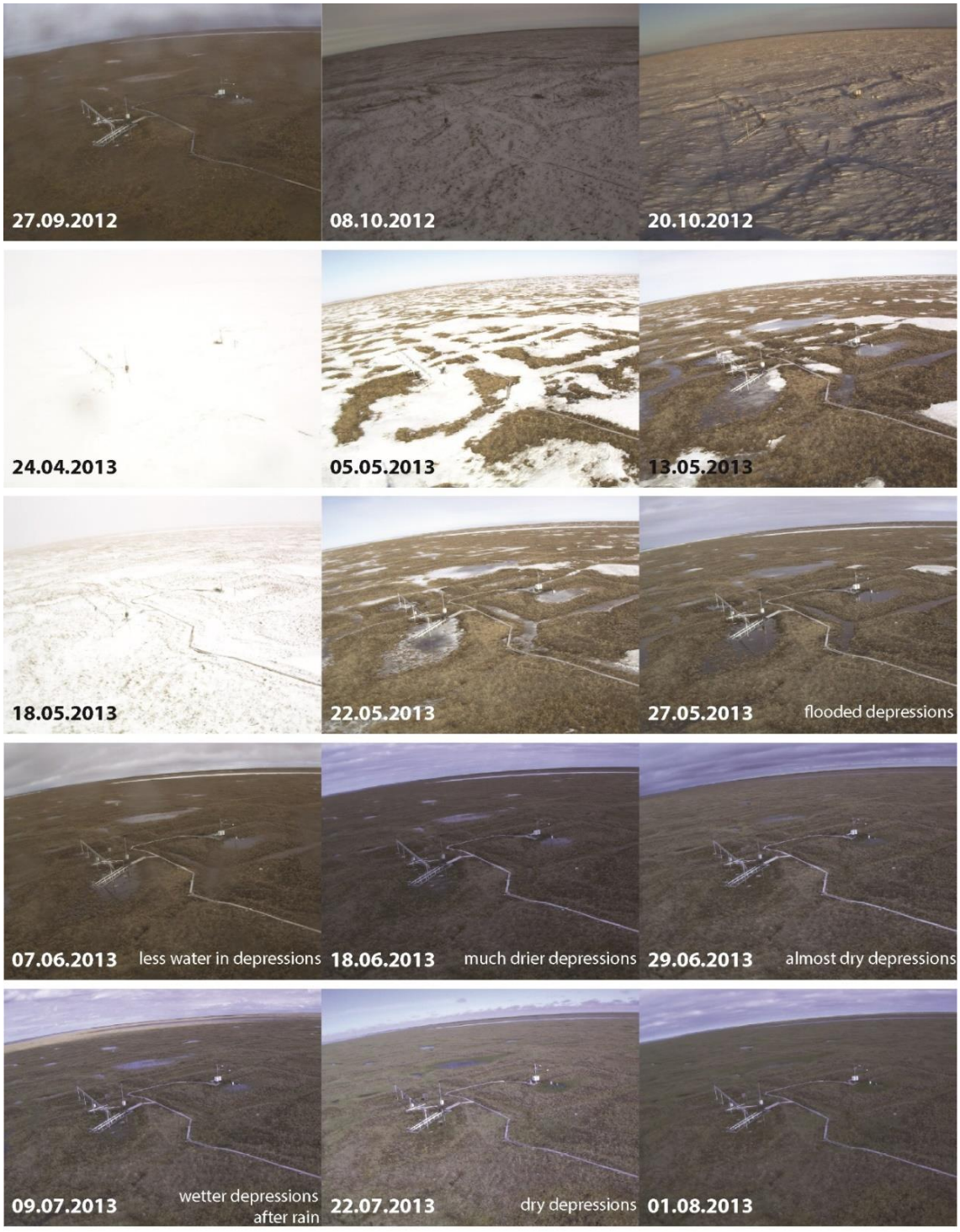

Figure A1. Photographs from time-lapse camera installed on Samoylov Island for various surface conditions. Scale: the horizontal bar to the left of center is at a height of 150 cm above the surface.

Table A1. Meteorological conditions close to the time of TSX acquisitions (08:34 local time). Air temperatures were recorded on Samoylov Island at 08:30 local time. Weather descriptions, surface conditions and snow height are from Khabarova hydrological station at 09:00 local time. Blue fill indicates dates of Events 1, 2 and 3, described in the Results section.

Date	Air temperature	Weather	Surface condition	Snow depth
03.08.2012	5.5 °C	-no precipitation	dry	no snow
25.08.2012	8.5 °C	-no precipitation		no snow
05.09.2012	4.2 °C	-no precipitation -no wind		no snow
16.09.2012	2.3 °C (fluctuating around 0 °C)	-no precipitation		no snow
27.09.2012	3.2 °C (positive during 2 previous days)	-constant non-freezing light rain -also during previous 9 consecutive hours		no snow
08.10.2012	-8.4 °C	-no precipitation	even layer of packed or wet snow covers the surface completely	1 cm
19.10.2012	-15.7 °C	-snowfalls and snowstorms during previous 12 hours -no precipitation at 09:00	even layer of dry, powdery snow covers the surface completely	3 cm
10.11.2012	-20.5 °C	-no wind -no precipitation	uneven layer of dry, powdery snow covers the surface completely	7 cm
21.11.2012	-21.7 °C	-constant light snowfall -constant snowfall during previous 19 hours	uneven layer of dry, powdery snow covers the surface completely	7 cm
02.12.2012	-32.3 °C	-weak/moderate snowdrift, generally low (lower than eye level) -snowfalls during previous 12 hours	uneven layer of dry, powdery snow covers the surface completely	7 cm
13.12.2012	-13.1 °C	-constant weak snowfall -constant snowfall during previous 21 hours, including snow showers	uneven layer of dry, powdery snow covers the surface completely	6 cm
24.12.2012	-33.5 °C	-weak/moderate snowdrift, generally low (lower than eye level) -snowstorms during previous 24 hours	uneven layer of dry, powdery snow covers the surface completely	5 cm

04.01.2013	-27 °C	-no precipitation	uneven layer of dry, powdery snow covers the surface completely	5 cm
15.01.2013	-39.3 °C	-no wind -no precipitation	uneven layer of dry, powdery snow covers the surface completely	5 cm
26.01.2013	-29 °C	-weak/moderate ground blizzard, generally high (higher than eye level) -snowfalls during previous 15 hours -no precipitation at 09:00	uneven layer of dry, powdery snow covers the surface completely	4 cm
06.02.2013	-39.7 °C	-weak/moderate snowdrift, generally low (lower than eye level) -snowstorms during previous 24 hours -no precipitation	uneven layer of dry, powdery snow covers the surface completely	4 cm
17.02.2013	-39.7 °C	-weak/moderate snowdrift, generally low (lower than eye level) -snowstorms during previous 12 hours -no precipitation	uneven layer of dry, powdery snow covers the surface completely	4 cm
28.02.2013	-29.6 °C	-weak/moderate ground blizzard, generally high (higher than eye level) - snowstorms during previous 24 hours -no precipitation	uneven layer of dry, powdery snow covers the surface completely	4 cm
11.03.2013	-39.2 °C	-no wind -no precipitation	uneven layer of dry, powdery snow covers the surface completely	5 cm
22.03.2013	-26.4 °C	-snowstorms during previous 24 hours -no precipitation	uneven layer of dry, powdery snow covers the surface completely	5 cm
02.04.2013	-30.7 °C	-snowfalls during previous 24 hours -no precipitation at 09:00	uneven layer of dry, powdery snow covers the surface completely	5 cm
13.04.2013	-15.8 °C	-snowfalls during previous 6 hours -no precipitation at 09:00	uneven layer of dry, powdery snow covers the surface completely	5 cm
24.04.2013	-20.8 °C	-no wind -no precipitation -daily haze	uneven layer of dry, powdery snow covers the surface completely	4 cm

05.05.2013	-2.1 °C (positive during preceding days and negative during the nights)	-no precipitation	packed or wet snow (with or without ice) covers at least half of the surface	Snow cover is not constant
16.05.2013	-9.4 °C (negative during both day and night)	-no precipitation at 09:00 -snowfalls, including snow showers 12 hours before	even layer of dry, powdery snow covers the surface completely	< 0.5 cm
27.05.2013	3.8 °C	-no wind -no precipitation	packed or wet snow (with or without ice) covers less than half of the surface	snow cover is not constant
07.06.2013	4.9 °C	-no precipitation at 09:00 -snow and rain 18 hours before		
18.06.2013	2.2 °C	-no precipitation		
29.06.2013	7 °C	-no precipitation	soil surface is wet (forming both small and large puddles)	
10.07.2013	10 °C	-no precipitation - continuous rain over the two previous days	soil surface is wet (forming both small and large puddles)	
21.07.2013	4.3 °C	-rain during previous 6 hours -no precipitation at 09:00	soil surface is moist	
01.08.2013	5.4 °C	-no precipitation	soil surface is moist	
23.08.2013	5 °C	-no precipitation	soil surface is moist	
03.09.2013	9.2 °C	-no precipitation	soil surface is moist	
14.09.2013	0.5 °C	- light snow shower at 09:00 and during previous 6 hours	soil surface is moist	

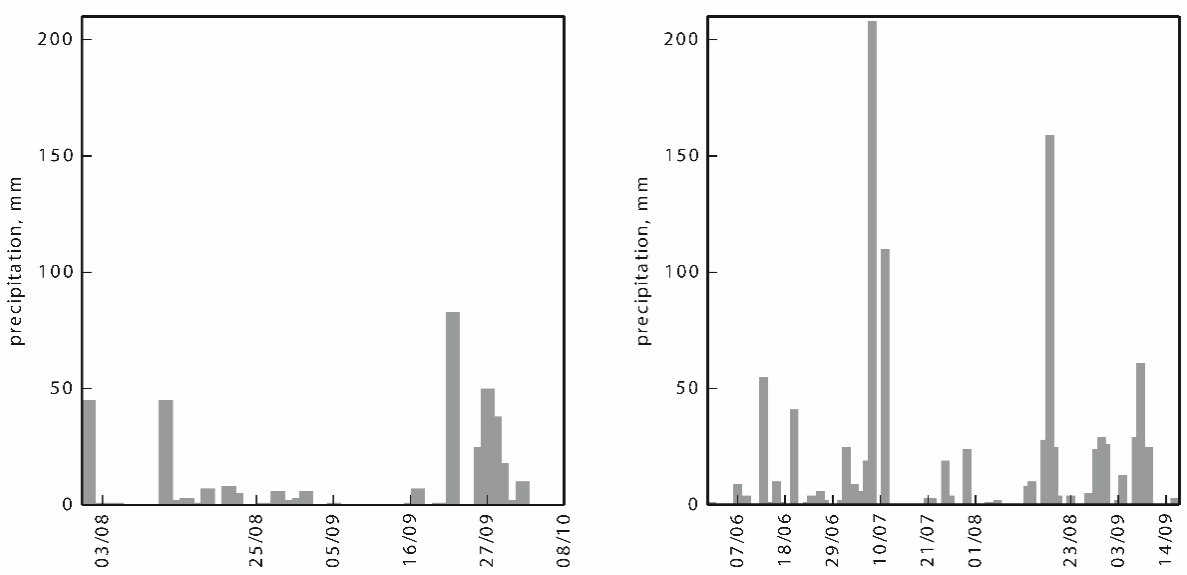

Figure A2. Daily accumulated precipitation data from the automated weather station on Samoylov Island for the periods from August 2012 to October 2012 (left) and June 2012 to September 2013 (right). Dates on the horizontal axis refer to SAR image acquisitions. Date format: DD/MM.

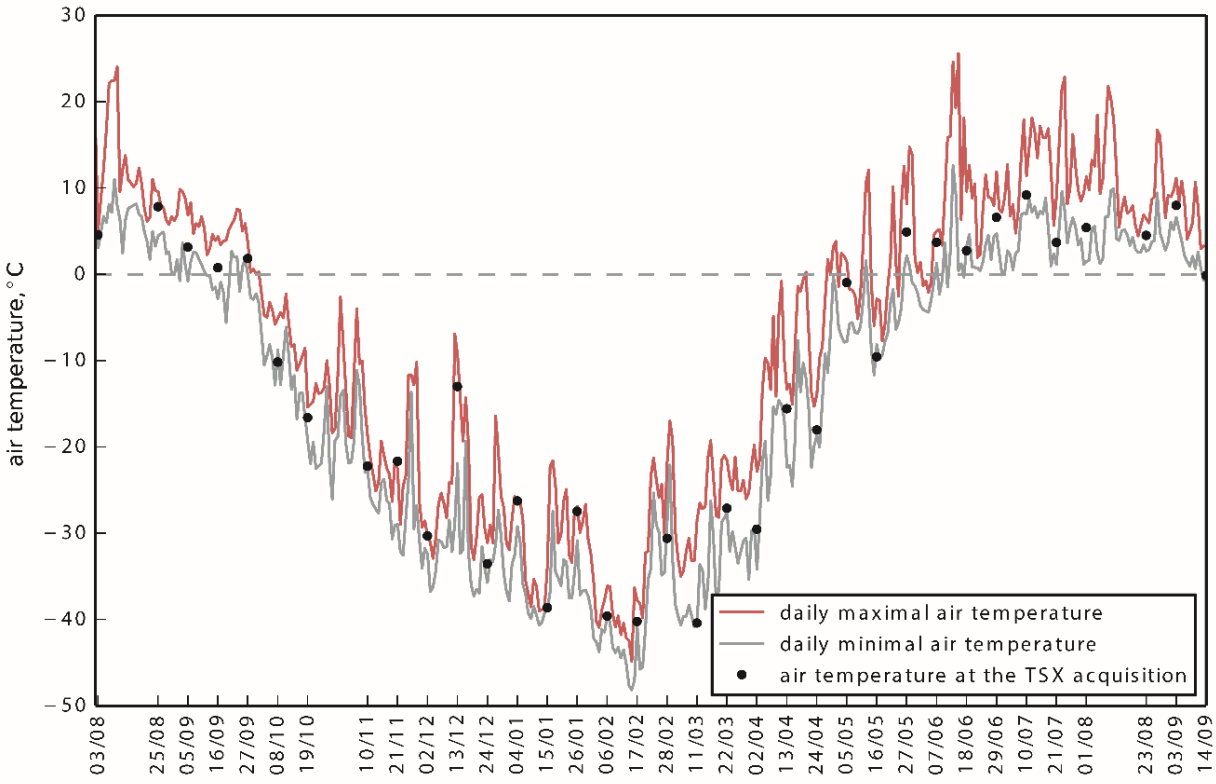

Figure A3. Daily minimum and maximum air temperatures from the automated weather station on Kurungnakh Island for the period from August 2012 to September 2013. Dates on the horizontal axis refer to SAR image acquisitions. Date format: DD/MM.

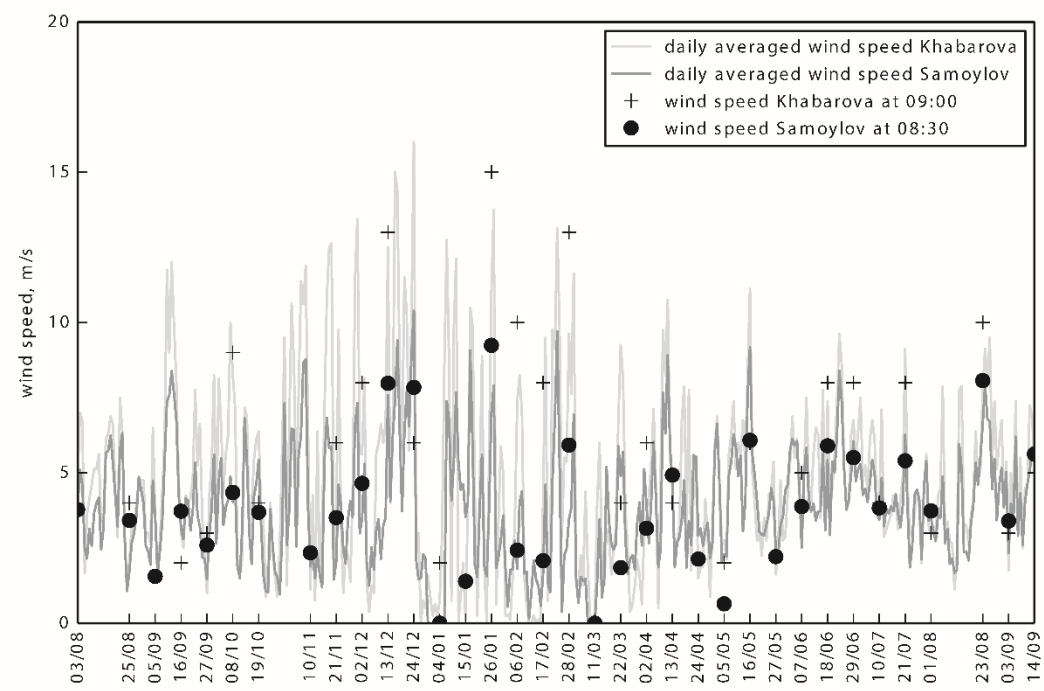

Figure A4. Daily averaged wind speed data for the period from August 2012 to September 2013 from two different sources: the automated weather station on Samoylov Island and the Khabarova hydrological station. Additional wind speed data at 08:30 (Samoylov) and 09:00 (Khabarova) local time is also provided (acquisition time is 08:34 local time). Dates on the horizontal axis refer to SAR image acquisition. (Date format: DD/MM).

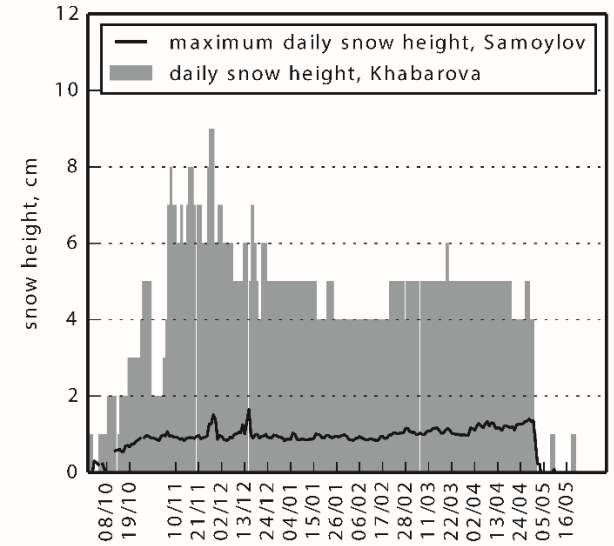

Figure A5. Snow height data from the Khabarova hydrological station and the Samoylov Island automated weather station for the period from October 2012 to May 2013. Dates on the horizontal axis refer to SAR image acquisition dates. (Date format: DD/MM).

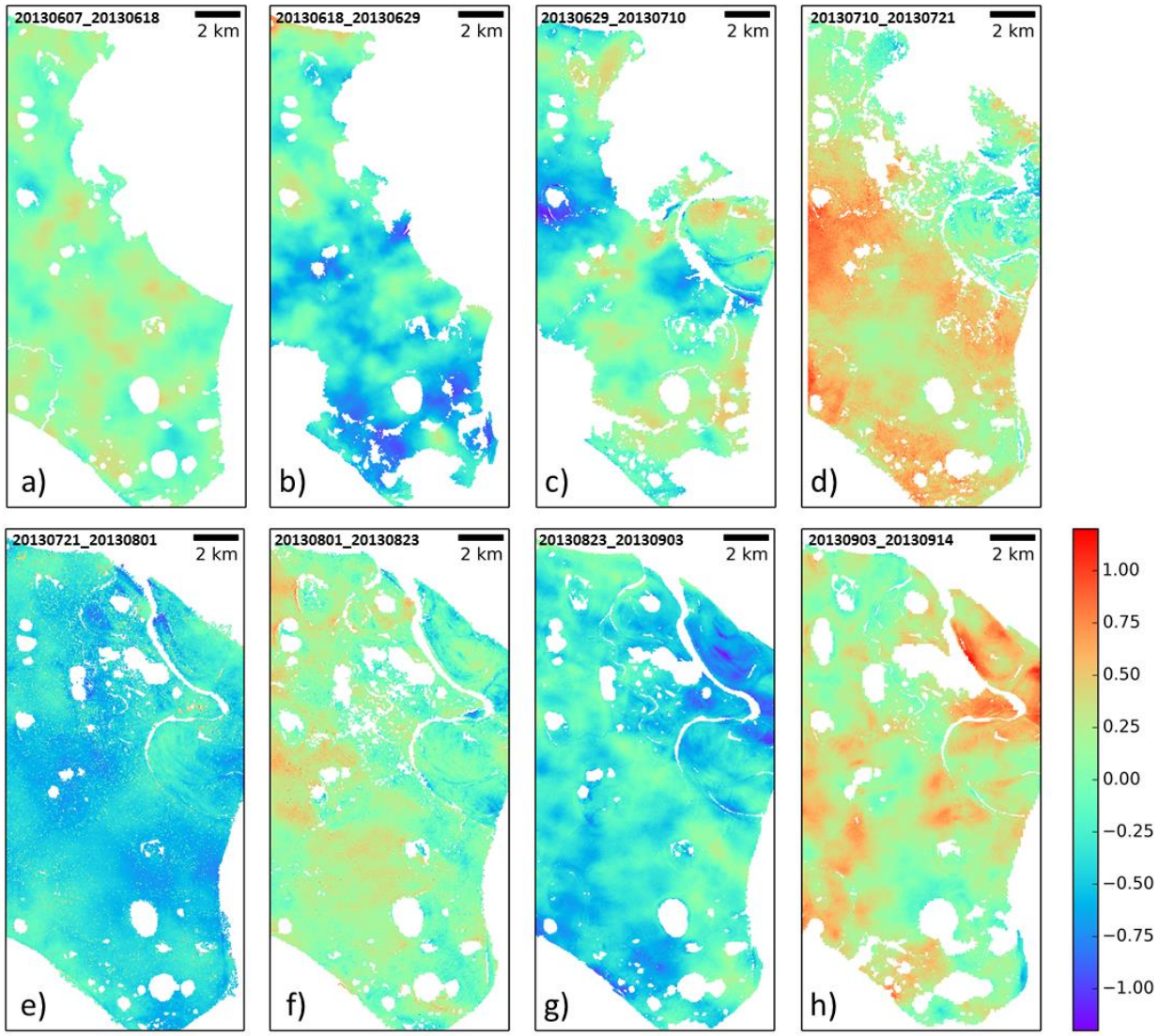

Figure A6. a)-h): individual displacement maps (in cm) from June to September 2013 used for stacking. Apparent is atmospheric noise on most of them.

Bibliography

ACIA, 2005. Arctic Climate Impact Assessment. ACIA Overview report. Cambridge University Press.

Akagawa, S., Huang, S.L., Kanie, S., & Fukuda, M. (2012). Movement due to heave and thaw settlement of a full-scale test chilled gas pipeline constructed in Fairbanks Alaska. In *OTC Arctic Technology Conference,* Houston, Texas, USA, 3-5 December 2012.

Alsdorf, D.E., Melack, J.M., Dunne, T., Mertes, L.A., Hess, L.L., & Smith, L.C. (2000). Interferometric radar measurements of water level changes on the Amazon flood plain. *Nature, 404*, 174-177, doi: 10.1038/35004560.

Antonova, S., Kääb, A., Heim, B., Langer, M., & Boike, J. (2016). Spatio-temporal variability of X-band radar backscatter and coherence over the Lena River Delta, Siberia. *Remote Sensing of Environment, 182*, 169-191, doi: 10.1016/j.rse.2016.05.003.

Arp, C.D., Jones, B.M., Urban, F.E., & Grosse, G. (2011). Hydrogeomorphic processes of thermokarst lakes with grounded-ice and floating-ice regimes on the Arctic coastal plain, Alaska. *Hydrological Processes, 25*(15), 2422-2438, doi: 10.1002/hyp.8019.

Arp, C.D., Jones, B.M., Lu, Z., & Whitman, M.S. (2012). Shifting balance of thermokarst lake ice regimes across the Arctic Coastal Plain of northern Alaska. *Geophysical Research Letters, 39*(16), doi: 10.1029/2012GL052518.

Arp, C.D., Jones, B.M., Liljedahl, A.K., Hinkel, K.M., & Welker, J.A. (2015). Depth, ice thickness, and ice-out timing cause divergent hydrologic responses among Arctic lakes. *Water Resources Research, 51*(12), 9379-9401, doi: 10.1002/2015WR017362.

Atwood, D.K., Meyer, F., & Arendt, A. (2010). Using L-band SAR coherence to delineate glacier extent. *Canadian Journal of Remote Sensing, 36*(sup1), S186-S195, doi: 10.5589/m10-014.

Atwood, D.K., Gunn, G.E., Roussi, C., Wu, J., Duguay, C., & Sarabandi, K. (2015). Microwave backscatter from Arctic lake ice and polarimetric implications. *Geoscience and Remote Sensing, IEEE Transactions on, 53*(11), 5972-5982, doi: 10.1109/TGRS.2015.2429917.

Aubert, M., Baghdadi, N., Zribi, M., Douaoui, A., Loumagne, C., Baup, F., El Hajj, M., & Garrigues, S. (2011). Analysis of TerraSAR-X data sensitivity to bare soil moisture, roughness, composition and soil crust. *Remote Sensing of Environment, 115*(8), 1801-1810, doi: 10.1016/j.rse.2011.02.021.

Baghdadi, N., Aubert, M., Cerdan, O., Franchistéguy, L., Viel, C., Martin, E., Zribi, M., & Desprats, J.F. (2007). Operational mapping of soil moisture using synthetic aperture radar data: application to the Touch basin (France). *Sensors, 7*(10), 2458-2483, doi: 10.3390/s7102458.

Baghdadi, N., Cresson, R., Todoroff, P., & Moinet, S. (2010). Multitemporal observations of sugarcane by TerraSAR-X images. *Sensors, 10*(10), 8899-8919, doi: 10.3390/s101008899.

Barrett, B., Whelan, P., & Dwyer, N. (2012). The use of C-and L-band repeat-pass interferometric SAR coherence for soil moisture change detection in vegetated areas. *Open Remote Sensing Journal, 5*(1), 37-53, doi: 10.2174/1875413901205010037.

Bartsch, A., Kidd, R.A., Wagner, W., & Bartalis, Z. (2007). Temporal and spatial variability of the beginning and end of daily spring freeze/thaw cycles derived from scatterometer data. *Remote Sensing of Environment, 106*(3), 360-374, doi: 10.1016/j.rse.2006.09.004.

Bartsch, A. (2014). Requirements for Monitoring of Permafrost in Polar Regions. *Available at: http://www.wmo.int/pages/prog/sat/meetings/documents/PSTG-4_Doc_08-03_Permafrost-Recommendations-Final.pdf (accessed November 2016).*

Beck, I., Ludwig, R., Bernier, M., Strozzi, T., & Boike, J. (2015). Vertical movements of frost mounds in sub-Arctic permafrost regions analyzed using geodetic survey and satellite interferometry. *Earth Surface Dynamics 3,* 409-421, doi: 10.5194/esurf-3-409-2015.

Bekryaev, R.V., Polyakov, I.V., & Alexeev, V.A. (2010). Role of polar amplification in long-term surface air temperature variations and modern Arctic warming. *Journal of Climate, 23*(14), 3888-3906, doi: 10.1175/2010JCLI3297.1.

Blaes, X. & Defourny, P. (2003). Retrieving crop parameters based on tandem ERS 1/2 interferometric coherence images. *Remote Sensing of Environment, 88*(4), 374-385, doi: 10.1016/j.rse.2003.08.008.

Boike, J., Langer, M., Lantuit, H., Muster, S., Roth, K., Sachs, T., Overduin, P., Westermann, S., & McGuire, A.D. (2012). Permafrost - physical aspects, carbon cycling, databases and uncertainties. In *Recarbonization of the Biosphere* (pp. 159-185). Springer Netherlands.

Boike, J., Kattenstroth, B., Abramova, K., Bornemann, N., Chetverova, A., Fedorova, I., Fröb, K., Grigoriev, M., Grüber, M., Kutzbach, L., Langer, M., Minke, M., Muster, S., Piel, K., Pfeiffer, E.-M., Stoof, G., Westermann, S., Wischnewski, K., Wille, C., & Hubberten, H.-W. (2013). Baseline characteristics of climate, permafrost and land cover from a new permafrost observatory in the Lena River Delta, Siberia (1998-2011). *Biogeosciences, 10,* 2105-2128, doi: 10.5194/bg-10-2105-2013.

Boike, J., Georgi, C., Kirilin, G., Muster, S., Abramova, K., Fedorova, I., Chetverova, A., Grigoriev, M., Bornemann, N., & Langer, M. (2015). Thermal processes of thermokarst lakes in the continuous permafrost zone of northern Siberia – observations and modeling (Lena River Delta, Siberia). *Biogeosciences, 12,* 5941-5965, doi: 10.5194/bg-12-5941-2015.

Borisov, L.A. (1973). Sovremennye vertikalnye dvizheniya poberezhja morya Laptevykh (Modern vertical movements of the Laptev Sea coast). *Okeanologiya (Oceanology), XIII,* 5, 835-841.

Borgeaud, M. & Wegmüller, U. (1996). On the use of ERS SAR interferometry for the retrieval of Geo- and Bio-physical information. In *Proceedings of the ERS SAR Interferometry Workshop FRINGE (Vol. 32).*

Bourgeau-Chavez, L.L., Smith, K.B., Brunzell, S.M., Kasischke, E.S., Romanowicz, E.A., & Richardson, C.J. (2005). Remote monitoring of regional inundation patterns and hydroperiod in the greater everglades using synthetic aperture radar. *Wetlands, 25*(1), 176-191, doi: 10.1672/0277-5212(2005)025[0176:RMORIP]2.0.CO;2.

Brisco, B., & Brown, R.J. (1998). Agricultural Applications with Radar. In *Manual of Remote Sensing: Principles and Applications of Imaging Radar, 3rd ed.*; (eds F. M. Henderson, A.J. Lewis). John Wiley and Sons: Toronto, Canada, 1998; Volume 2, pp. 381–406.

Brown, R.J., Manore, M.J., & Poirier, S. (1992). Correlations between X-, C-, and L-band imagery within an agricultural environment. *International Journal of Remote Sensing, 13*(9), 1645-1661, doi: 10.1080/01431169208904218.

Brown, J., Ferrians Jr., O.J., Heginbottom, J.A., & Melnikov, E.S. (1998, revised February 2001). Circum-arctic map of permafrost and ground ice conditions. Boulder, CO: National Snow and Ice Data Center/World Data Center for Glaciology. Digital media.

Brown, L.C. & Duguay, C.R. (2010). The response and role of ice cover in lake-climate interactions. *Progress in Physical Geography, 34*(5), 671-704, doi: 10.1177/0309133310375653.

Brown, R.S., Duguay, C.R., Mueller, R.P., Moulton, L.L., Doucette, P.J., & Tagestad, J.D. (2010). Use of Synthetic Aperture Radar (SAR) to identify and characterize overwintering areas of fish in ice-covered arctic rivers: a demonstration with Broad Whitefish and their habitats in the Sagavanirktok River, Alaska. *Transactions of the American Fisheries Society, 139*(6), 1711-1722, doi: 10.1577/T09-176.1.

Brown, L.C. & Duguay, C. R. (2011). A comparison of simulated and measured lake ice thickness using a Shallow Water Ice Profiler. *Hydrological Processes, 25*(19), 2932-2941, doi: 10.1002/hyp.8087.

Cook, T.L. & Bradley, R.S. (2010). An analysis of past and future changes in the ice cover of two High-Arctic lakes based on synthetic aperture radar (SAR) and Landsat imagery. *Arctic, Antarctic, and Alpine Research, 42*(1), 9-18, doi: 10.1657/1938-4246-42.1.9.

Deeb, E.J., Forster, R.R., & Kane, D.L. (2011). Monitoring snowpack evolution using interferometric synthetic aperture radar on the North Slope of Alaska, USA. *International journal of remote sensing, 32*(14), 3985-4003, doi: 10.1080/01431161003801351.

Dellepiane, S., Bo, G., Monni, S., & Buck, C. (2000). SAR images and interferometric coherence for flood monitoring. In *Geoscience and Remote Sensing Symposium, 2000. Proceedings. IGARSS 2000. IEEE 2000 International*, Vol. 6, pp. 2608-2610, doi: 10.1109/IGARSS.2000.859656.

Dobson, M.C. & Ulaby, F.T. (1986). Active microwave soil moisture research. *Geoscience and Remote Sensing, IEEE Transactions on, GE-24*(1), 23-36, doi: 10.1109/TGRS.1986.289585.

Du, J., Shi, J., & Rott, H. (2010). Comparison between a multi-scattering and multi-layer snow scattering model and its parameterized snow backscattering model. *Remote Sensing of Environment, 114*(5), 1089-1098, doi: 10.1016/j.rse.2009.12.020.

Duguay, C.R., Rouse, W.R., Lafleur, P.M., Boudreau, L.D., Crevier, Y., & Pultz, T.J. (1999). Analysis of multi-temporal ERS-1 SAR data of subarctic tundra and forest in the northern Hudson Bay Lowland and implications for climate studies. *Canadian journal of remote sensing, 25*(1), 21-33, doi: 10.1080/07038992.1999.10855260.

Duguay, C.R., Pultz, T.J., Lafleur, P.M., & Drai, D. (2002). RADARSAT backscatter characteristics of ice growing on shallow sub-Arctic lakes, Churchill, Manitoba, Canada. *Hydrological Processes, 16*(8), 1631-1644, doi: 10.1002/hyp.1026.

Duguay, C.R., Flato, G.M., Jeffries, M.O., Ménard, P., Morris, K., & Rouse, W.R. (2003). Ice-cover variability on shallow lakes at high latitudes: model simulations and observations. *Hydrological Processes, 17*(17), 3465-3483, doi: 10.1002/hyp.1394.

Duguay, C.R. & Lafleur, P.M. (2003). Determining depth and ice thickness of shallow sub-Arctic lakes using space-borne optical and SAR data. *International Journal of Remote Sensing, 24*(3), 475-489, doi: 10.1080/01431160210144507.

Duguay, C.R., Zhang, T., Leverington, D.W. & Romanovsky, V.E. (2005). Satellite remote sensing of permafrost and seasonally frozen ground. In *Remote Sensing in Northern Hydrology: Measuring Environmental Change* (eds C.R. Duguay and A. Pietroniro). Geophysical Monograph 163, American Geophysical Union, Washington, DC, 160, pp. 91-118, doi: 10.1029/163GM06.

Duguay, C.R., Prowse, T.D., Bonsal, B.R., Brown, R.D., Lacroix, M.P., & Menard, P. (2006). Recent trends in Canadian lake ice cover. *Hydrological Processes, 20*, 781–801, doi: 10.1002/hyp.6131.

Duguay, Y., Bernier, M., Lévesque, E., & Tremblay, B. (2015). Potential of C and X Band SAR for Shrub Growth Monitoring in Sub-Arctic Environments. *Remote Sensing, 7*(7), 9410-9430, doi: 10.3390/rs70709410.

Elachi, C., Bryan, M.L., & Weeks, W.F. (1976). Imaging radar observations of frozen Arctic lakes. *Remote Sensing of Environment, 5*, 169-175.

Engdahl, M.E., Borgeaud, M., & Rast, M. (2001). The use of ERS-1/2 tandem interferometric coherence in the estimation of agricultural crop heights. *Geoscience and Remote Sensing, IEEE Transactions on, 39*(8), 1799-1806, doi: 10.1109/36.942558.

Engram, M., Walter-Anthony, K., Meyer, F.J., & Grosse, G. (2013). Characterization of L-band synthetic aperture radar (SAR) backscatter from floating and grounded thermokarst lake ice in Arctic Alaska. *The Cryosphere, 7*(6), 1741-1752, doi: 10.5194/tc-7-1741-2013.

Fedorova, I., Chetverova, A., Bolshiyanov, D., Makarov, A., Boike, J., Heim, B., Morgenstern, A., Overduin, P. P., Wegner, C., Kashina, V., Eulenburg, A., Dobrotina, E., & Sidorina, I. (2015). Lena Delta hydrology and geochemistry: long-term hydrological data and recent field observations. *Biogeosciences, 12*, 345-363, doi: 10.5194/bg-12-345-2015.

Fraser, R.H., Olthof, I., Kokelj, S.V., Lantz, T.C., Lacelle, D., Brooker, A., Wolfe, S., & Schwarz, S. (2014). Detecting landscape changes in high latitude environments using Landsat trend analysis: 1. Visualization. *Remote Sensing, 6*(11), 11533-11557, doi: 10.3390/rs61111533.

Frey, H., Paul, F., & Strozzi, T. (2012). Compilation of a glacier inventory for the western Himalayas from satellite data: methods, challenges, and results. *Remote Sensing of Environment, 124*, 832-843, doi: 10.1016/j.rse.2012.06.020.

Frolking, S., McDonald, K.C., Kimball, J.S., Way, J.B., Zimmermann, R., & Running, S.W. (1999). Using the space-borne NASA scatterometer (NSCAT) to determine the frozen and thawed seasons. *Journal of Geophysical Research: Atmospheres (1984–2012), 104(*D22*)*, 27895-27907, doi: 10.1029/1998JD200093.

Gangodagamage, C., Rowland, J.C., Hubbard, S.S., Brumby, S.P., Liljedahl, A.K., Wainwright, H., Wilson, C.J., Altmann, G.L., Dafflon, B., Peterson, J., Ulrich, C., Tweedie, C.E., & Wullschleger, C.D. (2014). Extrapolating active layer thickness measurements across Arctic polygonal terrain using LiDAR and NDVI data sets. *Water resources research, 50*(8), 6339-6357, doi: 10.1002/2013WR014283.

Geldsetzer, T., van der Sanden, J., & Brisco, B. (2010). Monitoring lake ice during spring melt using RADARSAT-2 SAR. *Canadian journal of remote sensing, 36*(sup2), S391-S400, doi: 10.5589/m11-001.

Goldstein, R.M. & Werner, C.L. (1998). Radar interferogram filtering for geophysical applications. *Geophysical Research Letters, 25*(21), 4035-4038.

Gonzalez, R.C. & Woods, R.E. (2002). Digital Image Processing, 2nd ed., Prentice Hall, Upper Saddle River, NJ.

Grigoriev, N.F. (1960). Temperatura mnogoletnemyerzlykh porod v basseyne del'ty r.Leny (The temperature of permafrost in the Lena Delta basin). In *Usloviya zaleganiya i svoystva mnogoletnemyerzlykh porod na territorii Yakutskoy ASSR (Conditions of depositing and properties of the permafrost in Yakutia)*. Yakutsk, 2, 97–101 (in Russian).

Grigoriev, M.N. (1993). Kryomorfogenez ust'evoj oblasti r.Leny (Cryomorphogenesis of the Lena River mouth area). Siberian Branch, USSR Academy of Sciences, Yakutsk, 174 pp. (in Russian).

Grosse G., Jones B., & Arp C. (2013) Thermokarst lakes, drainage, and drained basins. In: John F. Shroder (Editor-in-chief), Giardino, R., and Harbor, J. (Volume Editors). *Treatise on Geomorphology, Vol 8*, Glacial and Periglacial Geomorphology, San Diego: Academic Press; p. 325-353, doi: 10.1016/B978-0-12-374739-6.00216-5.

Gunn, G.E., Duguay, C.R, Brown, L., Atwood, D., King, J., & Kasurak, A. (2015a). Freshwater lake ice thickness derived using X- and Ku-band FMCW scatterometers. *Cold Regions Science and Technology, 120*, 115-126, doi: 10.1016/j.coldregions.2015.09.012.

Gunn, G.E., Brogioni, M., Duguay, C., Macelloni, G., Kasurak, A., & King, J. (2015b). Observation and modeling of X-and Ku-band backscatter of snow-covered freshwater lake ice. *Selected Topics in Applied Earth Observations and Remote Sensing, IEEE Journal of, 8*(7), 3629-3642, doi: 10.1109/JSTARS.2015.2420411.

Günther, F., 2009. Untersuchung der Thermokarstentwicklung im südlichen Lena Delta anhand multitemporaler Fernerkundungs- und Felddaten (Investigation of thermokarst evolution in the southern Lena Delta using multitemporal remote sensing and field data). (Diploma Thesis) Technichal University of Dresden, Dresden, Germany (in German).

Günther, F., Overduin, P.P., Sandakov, A.V., Grosse, G., & Grigoriev, M.N. (2013). Short-and long-term thermo-erosion of ice-rich permafrost coasts in the Laptev Sea region. *Biogeosciences, 10*, 4297-4318, doi: 10.5194/bg-10-4297-2013.

Günther, F., Overduin, P.P., Yakshina, I.A., Opel, T., Baranskaya, A.V., & Grigoriev, M.N. (2015). Observing Muostakh disappear: permafrost thaw subsidence and erosion of a ground-ice-rich island in response to arctic summer warming and sea ice reduction. *The Cryosphere, 9*(1), 151-178.

Guneriussen, T., Høgda, K.A., Johnsen, H., & Lauknes, I. (2001). InSAR for estimation of changes in snow water equivalent of dry snow. *Geoscience and Remote Sensing, IEEE Transactions on, 39*(10), 2101-2108, doi: 10.1109/36.957273.

Hall, D.K., Fagre, D.B., Klasner, F., Linebaugh, G., & Liston, G.E. (1994). Analysis of ERS-1 synthetic aperture radar data of frozen lakes in northern Montana and implications for climate studies. *Journal of Geophysical Research: Oceans, 99*(C11), 22473-22482.

Hall, D.K., Frei, A., & Déry, S.J. (2015) Remote sensing of snow extent, in *Remote Sensing of the Cryosphere* (ed. M. Tedesco), John Wiley & Sons, Ltd, Chichester, UK, doi: 10.1002/9781118368909.ch3.

Hall-Atkinson, C. & Smith, L.C. (2001). Delineation of delta ecozones using interferometric SAR phase coherence: Mackenzie River Delta, NWT, Canada. *Remote sensing of environment*, *78*(3), 229-238, doi: 10.1016/S0034-4257(01)00221-8.

Harris, C., Luetschg, M., Davies, M.C.R., Smith, F.W., Christiansen, H.H. & Isaksen, K. (2007). Field Instrumentation for Real-time Monitoring of Periglacial Solifluction. *Permafrost and Periglacial Processes, 18*, 105–114.

Hirose, T., Kapfer, M., Bennett, J., Cott, P., Manson, G., & Solomon, S. (2008). Bottomfast ice mapping and the measurement of ice thickness on tundra lakes using C-Band Synthetic Aperture Radar remote sensing. *Journal of the American Water Resources Association, 44*(2), 285-292, doi: 10.1111/j.1752-1688.2007.00161.x.

Hoekstra, P. & Delaney, A. (1974). Dielectric properties of soils at UHF and microwave frequencies. Journal of geophysical research, 79(11), 1699-1708.

Hong, S.H., Wdowinski, S., Kim, S.W., & Won, J.S. (2010). Multi-temporal monitoring of wetland water levels in the Florida Everglades using interferometric synthetic aperture radar (InSAR). *Remote Sensing of Environment, 114*(11), 2436-2447, doi: 10.1016/j.rse.2010.05.019.

Howell, S.E., Brown, L.C., Kang, K.K., & Duguay, C.R. (2009). Variability in ice phenology on Great Bear Lake and Great Slave Lake, Northwest Territories, Canada, from SeaWinds/QuikSCAT: 2000–2006. *Remote Sensing of Environment, 113*(4), 816-834, doi: 10.1016/j.rse.2008.12.007.

Hugelius, G., Strauss, J., Zubrzycki, S., Harden, J.W., Schuur, E.A.G., Ping, C.-L., Schirrmeister, L., Grosse, G., Michaelson, G.J., Koven, C.D., O'Donnell, J.A., Elberling, B., Mishra, U., Camill, P., Yu, Z., Palmtag, J., & Kuhry, P. (2014). Estimated stocks of circumpolar permafrost carbon with quantified uncertainty ranges and identified data gaps. *Biogeosciences, 11*, 6573-6593, doi: 10.5194/bg-11-6573-2014.

IPCC, 2013: Climate Change 2013: The Physical Science Basis. Contribution of Working Group I to the Fifth Assessment Report of the Intergovernmental Panel on Climate Change [Stocker, T.F., D. Qin, G.-K. Plattner, M. Tignor, S.K. Allen, J. Boschung, A. Nauels, Y. Xia, V. Bex and P.M. Midgley (eds.)]. Cambridge University Press, Cambridge, United Kingdom and New York, NY, USA, 1535 pp.

Jeffries, M.O., Morris, K., Weeks, W.F., & Wakabayashi, H. (1994). Structural-stratigraphic features and ERS-1 SAR backscatter characteristics of ice growing on shallow lakes in NW Alaska, winter 1991–92. *Journal of Geophysical Research, 99*(C11), 22459-22471.

Jeffries, M.O., Morris, K., & Liston, G.E. (1996). A method to determine lake depth and water availability on the North Slope of Alaska with spaceborne imaging radar and numerical ice growth modelling. *Arctic,* 367-374.

Jeffries, M.O., Zhang, T., Frey, K., & Kozlenko, N. (1999). Estimating late-winter heat flow to the atmosphere from the lake-dominated Alaskan North Slope. *Journal of Glaciology, 45*(150), 315-324.

Jeffries, M.O., Morris, K., & Duguay, C.R. (2005). Lake ice growth and decay in central Alaska, USA: observations and computer simulations compared. *Annals of Glaciology, 40*(1), 195-199, doi: 10.3189/172756405781813807.

Jones, B.M., Grosse, G., Arp, C.D., Jones, M.C., Walter-Anthony, K.M., & Romanovsky, V.E. (2011). Modern thermokarst lake dynamics in the continuous permafrost zone, northern Seward Peninsula, Alaska. *Journal of Geophysical Research: Biogeosciences, 116*(G2), doi: 10.1029/2011JG001666.

Jones, B.M., Gusmeroli, A., Arp, C.D., Strozzi, T., Grosse, G., Gaglioti, B.V., & Whitman, M.S. (2013). Classification of freshwater ice conditions on the Alaskan Arctic Coastal Plain using ground penetrating radar and TerraSAR-X satellite data. International *Journal of Remote Sensing, 34*(23), 8267-8279, doi: 10.1080/2150704X.2013.834392.

Jorgenson, M.T., Harden, J., Kanevskiy, M., O'Donnell, J., Wickland, K., Ewing, S., Manies, K., Zhuang, Q., Shur, Y., Striegl, R., & Koch, J. (2013). Reorganization of vegetation, hydrology and soil carbon after permafrost degradation across heterogeneous boreal landscapes. *Environmental Research Letters*, *8 035017*, doi: 10.1088/1748-9326/8/3/035017.

Kaatze, U. & Uhlendorf, V. (1981). The dielectric properties of water at microwave frequencies. *Zeitschrift für Physikalische Chemie, 126* (2), 151-165.

Kääb, A. (2008). Remote sensing of permafrost-related problems and hazards. *Permafrost and Periglacial Processes*, *19*(2), 107-136, doi: 10.1002/ppp.619.

Kane, D.L., Hinzman, L.D., Haofang, Y., & Goering, D.J. (1996). The use of SAR satellite imagery to measure active layer moisture contents in Arctic Alaska. *Nordic Hydrology, 27*(1-2), 25-38.

Kasischke, E.S., Smith, K.B., Bourgeau-Chavez, L.L., Romanowicz, E.A., Brunzell, S., & Richardson, C.J. (2003). Effects of seasonal hydrologic patterns in south Florida wetlands on radar backscatter measured from ERS-2 SAR imagery. *Remote sensing of environment, 88*(4), 423-441, doi: 10.1016/j.rse.2003.08.016.

Kasischke, E.S., Bourgeau-Chavez, L.L., Rober, A.R., Wyatt, K.H., Waddington, J.M., & Turetsky, M.R. (2009). Effects of soil moisture and water depth on ERS SAR backscatter measurements from an Alaskan wetland complex. *Remote Sensing of Environment, 113*(9), 1868-1873, doi: 10.1016/j.rse.2009.04.006.

Kimball, J., McDonald, K., Keyser, A., Frolking, S. & Running, S. (2001). Application of the NASA scatterometer (NSCAT) for determining the daily frozen and nonfrozen landscape of Alaska. *Remote Sensing of Environment, 75(1)*, 113–126, doi: 10.1016/S0034-4257(00)00160-7.

Kong, X. & Dorling, S.R. (2008). Near-surface soil moisture retrieval from ASAR Wide Swath imagery using a Principal Component Analysis. *International Journal of Remote Sensing, 29*(10), 2925-2942, doi: 10.1080/01431160701442088.

Kozlenko, N. & Jeffries, M.O. (2000). Bathymetric mapping of shallow water in thaw lakes on the North Slope of Alaska with spaceborne imaging radar. *Arctic*, 306-316, doi: 10.14430/arctic860.

Kumar, V. & Venkataraman, G. (2011). SAR interferometric coherence analysis for snow cover mapping in the western Himalayan region. *International Journal of Digital Earth, 4*(1), 78-90, doi: 10.1080/17538940903521591.

Lafleur, P.M., Wurtele, B., & Duguay, C.R. (1997). Spatial and temporal variations in surface albedo of a subarctic landscape using surface-based measurements and remote sensing. *Arctic and Alpine Research, 29*, 261–269, doi: 10.2307/1552140.

Langer, M., Westermann, S., Muster, S., Piel, K., & Boike, J. (2011a). The surface energy balance of a polygonal tundra site in northern Siberia. Part 1: Spring to fall. *The Cryosphere, 5*, 151-171, doi: 10.5194/tc-5-151-2011.

Langer, M., Westermann, S., Muster, S., Piel, K., & Boike, J. (2011b). The surface energy balance of a polygonal tundra site in northern Siberia. Part 2: Winter. *The Cryosphere, 5*, 509-524, doi: 10.5194/tc-5-509-2011.

Langer, M., Westermann, S., Heikenfeld, M., Dorn, W., & Boike, J. (2013). Satellite-based modeling of permafrost temperatures in a tundra lowland landscape. *Remote Sensing of Environment, 135,* 12-24, doi: 10.1016/j.rse.2013.03.011.

Langer, M., Westermann, S., Walter-Anthony, K., Wischnewski, K., & Boike, J. (2015). Frozen ponds: production and storage of methane during the Arctic winter in a lowland tundra landscape in northern Siberia, Lena River delta. *Biogeosciences, 12*, 977-990, doi: 10.5194/bg-12-977-2015.

Lantuit, H. & Pollard, W.H. (2005). Temporal stereophotogrammetric analysis of retrogressive thaw slumps on Herschel Island, Yukon Territory. *Natural Hazards and Earth System Science, 5*(3), 413-423.

Lantuit, H. & Pollard, W.H. (2008). Fifty years of coastal erosion and retrogressive thaw slump activity on Herschel Island, southern Beaufort Sea, Yukon Territory, Canada. *Geomorphology, 95(1-2),* 84-102, doi: 10.1016/j.geomorph.2006.07.040.

Latifovic, R. & Pouliot, D. (2007). Analysis of climate change impacts on lake ice phenology in Canada using the historical satellite data record. *Remote Sensing of Environment, 106*(4), 492-507, doi: 10.1016/j.rse.2006.09.015.

Lenormand, F., Duguay, C.R., & Gauthier, R. (2002). Development of a historical database for the study of climate change in Canada. *Hydrological Processes, 16*, 3707–3722, doi: 10.1002/hyp.1235.

Le Toan, T., Laur, H., Mougin, E., & Lopes, A. (1989). Multitemporal and dual-polarization observations of agricultural vegetation covers by X-band SAR images. *Geoscience and Remote Sensing, IEEE Transactions on, 27*(6), 709-718, doi: 10.1109/TGRS.1989.1398243.

Li, Z., Guo, H., Li, X., & Wang, C. (2001). SAR Interferometry coherence analysis for snow mapping. In *Geoscience and Remote Sensing Symposium, 2001. IGARSS'01. IEEE 2001 International* (Vol. 6), pp. 2905-2907, doi: 10.1109/IGARSS.2001.978201.

Li, Z., Zhao, R., Hu, J., Wen, L., Feng, G., Zhang, Z., & Wang, Q. (2015). InSAR analysis of surface deformation over permafrost to estimate active layer thickness based on one-dimensional heat transfer model of soils. *Scientific reports, 5*, doi: 10.1038/srep15542.

Lide, D.R., ed. (2005). *CRC Handbook of Chemistry and Physics* (86th ed.). Boca Raton (FL): CRC Press. ISBN 0-8493-0486-5.

Little, J.D., Sandall, H., Walegur, M.T., & Nelson, F.E. (2003). Application of differential global positioning systems to monitor frost heave and thaw settlement in tundra environments. *Permafrost and Periglacial Processes, 14*, 349–357.

Liu, L., Zhang, T., & Wahr, J. (2010). InSAR measurements of surface deformation over permafrost on the North Slope of Alaska. *Journal of Geophysical Research: Earth Surface*, *115*(F3), doi: 10.1029/2009JF001547.

Liu, L., Schaefer, K., Zhang, T., & Wahr, J. (2012). Estimating 1992–2000 average active layer thickness on the Alaskan North Slope from remotely sensed surface subsidence. *Journal of Geophysical Research: Earth Surface, 117*(F1), doi: 10.1029/2011JF002041.

Liu, L., Schaefer, K., Gusmeroli, A., Grosse, G., Jones, B.M., Zhang, T., Parsekian, A.D., & Zebker, H.A. (2014). Seasonal thaw settlement at drained thermokarst lake basins, Arctic Alaska. *The Cryosphere, 8*, 815-826, doi: 10.5194/tc-8-815-2014.

Liu, L., Schaefer, K.M., Chen, A.C., Gusmeroli, A., Zebker, H.A., & Zhang, T. (2015). Remote sensing measurements of thermokarst subsidence using InSAR. *Journal of Geophysical Research: Earth Surface, 120*(9), 1935-1948, doi: 10.1002/2015JF003599.

Lu, Z. & Meyer, D.J. (2002). Study of high SAR backscattering caused by an increase of soil moisture over a sparsely vegetated area: implications for characteristics of backscattering. *International Journal of Remote Sensing, 23*(6), 1063-1074, doi: 10.1080/01431160110040035.

Luo, X., Askne, J., Smith, G., & Dammert, P. (2001). Coherence Characteristics of Radar Signals From Rough Soil. *Progress In Electromagnetics Research, PIER 31,* 69–88.

Macelloni, G., Malnes, E., Nagler, T., Pulliainen, J., Rebhan, H., & Thompson A. (2010). Cold regions hydrology high-resolution observatory for snow and cold land processes. *Proceedings of the IEEE, 98*(5), 752-765, doi: 10.1109/JPROC.2009.2038947.

Mätzler, C. & Schanda, E. (1984). Snow mapping with active microwave sensors. *International Journal of Remote Sensing, 5*(2), 409-422, doi: 10.1080/01431168408948816.

Mars, J.C. & Houseknecht, D.W. (2007). Quantitative remote sensing study indicates doubling of coastal erosion rate in past 50 yr along a segment of the Arctic coast of Alaska. *Geology, 35*(7), 583-586, doi: 10.1130/G23672A.1.

Massonnet, D., Rossi, M., Carmona, C., Adragna, F., Peltzer, G., Feigl, K., & Rabaute, T. (1993). The displacement field of the Landers earthquake mapped by radar interferometry. *Nature, 364*, 138-142, doi: 10.1038/364138a0.

Meier, W.N. & Markus, T. (2015) Remote sensing of sea ice, in *Remote Sensing of the Cryosphere* (ed. M. Tedesco), John Wiley & Sons, Ltd, Chichester, UK, doi: 10.1002/9781118368909.ch11.

Melnikov, P.I. (1967). Vliyanie podzemnykh vod na glubokoe okhlazhdenie verkhnej zony zemnoj kory (Influence of ground waters on the deep cooling of upper Earth crust).

*Merzlotno-gidrogeologicheskie i gidrogeotermicheskie issledovaniya na vostoke SSSR (Cryo-hydrogeological and hydrogeothermal investigations in the East of USSR).*Nauka, p.24-29.

Millward, A.A., Piwowar, J.M., & Howarth, P.J. (2006). Time-series analysis of medium-resolution, multisensor satellite data for identifying landscape change. *Photogrammetric Engineering & Remote Sensing, 72*(6), 653-663.

Moeremans, B. & Dautrebande, S. (2000). Soil moisture evaluation by means of multi-temporal ERS SAR PRI images and interferometric coherence. *Journal of Hydrology, 234*(3), 162-169, doi: 10.1016/S0022-1694(00)00251-1.

Morgenstern, A., Grosse, G., Günther, F., Fedorova, I., & Schirrmeister, L. (2011). Spatial analyses of thermokarst lakes and basins in Yedoma landscapes of the Lena Delta. *The Cryosphere, 5*, 849-867, doi: 10.5194/tc-5-849-2011.

Morgenstern, A., Ulrich, M., Günther, F., Roessler, S., Fedorova, I.V., Rudaya, N.A., Wetterich, S., Boike, J., & Schirrmeister, L. (2013). Evolution of thermokarst in East Siberian ice-rich permafrost: A case study. *Geomorphology*, *201*, 363-379, doi: 10.1016/j.geomorph.2013.07.011.

Morris, K., Jeffries, M.O., & Weeks, W.F. (1995). Ice processes and growth history on Arctic and sub-Arctic lakes using ERS-1 SAR data. *Polar Record, 31*(177), 115-128.

Morrissey, L.A., Durden, S.L., Livingston, G.P., Steam, J.A., & Guild, L. S. (1996). Differentiating methane source areas in arctic environments with multitemporal ERS-1 SAR data. *Geoscience and Remote Sensing, IEEE Transactions on, 34*(3), 667-673, doi: 10.1109/36.499746.

Muskett, R.R., Romanovsky, V.E., Cable, W.L., & Kholodov, A.L. (2015). Active-Layer Soil Moisture Content Regional Variations in Alaska and Russia by Ground-Based and Satellite-Based Methods, 2002 through 2014. *International Journal of Geosciences, 6*, 12-41, doi: 10.4236/ijg.2015.61002.

Muster, S., Langer, M., Heim, B., Westermann, S., & Boike, J. (2012). Subpixel heterogeneity of ice-wedge polygonal tundra: a multi-scale analysis of land cover and evapotranspiration in the Lena River Delta, Siberia. *Tellus B*, *64* 17301, doi: 10.3402/tellusb.v64i0.17301.

Muster, S., Heim, B., Abnizova, A., & Boike, J. (2013). Water Body Distributions Across Scales: A Remote Sensing Based Comparison of Three Arctic Tundra Wetlands. *Remote Sensing, 5*(4), 1498-1523, doi: 10.3390/rs5041498.

Naeimi, V., Paulik, C., Bartsch, A., Wagner, W., Kidd, R., Park, S.E., Elger, K., & Boike, J. (2012). ASCAT Surface State Flag (SSF): Extracting information on surface freeze/thaw conditions from backscatter data using an empirical threshold-analysis algorithm. *Geoscience and Remote Sensing, IEEE Transactions on, 50*(7), 2566-2582, doi: 10.1109/TGRS.2011.2177667.

Nagler, T. & Rott, H. (2000). Retrieval of wet snow by means of multitemporal SAR data. *Geoscience and Remote Sensing, IEEE Transactions on, 38*(2), 754-765, doi: 10.1109/36.842004.

National Research Council. Opportunities to Use Remote Sensing in Understanding Permafrost and Related Ecological Characteristics: Report of a Workshop. Washington, DC: The National Academies Press, 2014, doi:10.17226/18711.

Nelson, F.E., Shiklomanov, N.I., Mueller, G.R., Hinkel, K.M., Walker, D.A., & Bockheim, J.G. (1997). Estimating active-layer thickness over a large region: Kuparuk River basin, Alaska, USA. *Arctic and Alpine Research, 29*(4), 367-378, doi: 10.2307/1551985.

Nelson, F.E., Anisimov, O.A., & Shiklomanov, N.I. (2001). Subsidence risk from thawing permafrost. *Nature, 410*, 889-890, doi: 10.1038/35073746.

Nesti, G., Tarchi, D., & Rudant, J.P. (1995). Decorrelation of backscattered signal due to soil moisture changes. In *Geoscience and Remote Sensing Symposium, 1995. IGARSS'95. 'Quantitative Remote Sensing for Science and Applications', International* (Vol. 3), pp. 2026-2028, doi: 10.1109/IGARSS.1995.524098.

Nico, G., Pappalepore, M., Pasquariello, G., Refice, A., & Samarelli, S. (2000). Comparison of SAR amplitude vs. coherence flood detection methods-a GIS application. *International Journal of Remote Sensing, 21*(8), 1619-1631, doi: 10.1080/014311600209931.

Nitze, I. & Grosse, G. (2016). Detection of landscape dynamics in the Arctic Lena Delta with temporally dense Landsat time-series stacks. *Remote Sensing of Environment, 181*, 27-41, doi: 10.1016/j.rse.2016.03.038.

Nixon, M., Tarnocai, C., & Kutny, L. (2003). Long-term active layer monitoring: Mackenzie Valley, northwest Canada. In *Proceedings of the 8th International Conference on Permafrost* (Vol. 2, pp. 821-826).

NOAA National Centers for Environmental Information, State of the Climate: Global Analysis for December 2015, published online January 2016, http://www.ncdc.noaa.gov/sotc/global/201512.

Osterkamp, T.E., Jorgenson, M.T., Schuur, E.A.G., Shur, Y.L., Kanevskiy, M.Z., Vogel, J.G., & Tumskoy, V.E. (2009). Physical and ecological changes associated with warming permafrost and thermokarst in interior Alaska. *Permafrost and Periglacial Processes*, *20*(3), 235-256, doi: 10.1002/ppp.656.

Overduin, P.P. & Kane, D.L. (2006). Frost boils and soil ice content: Field observations. *Permafrost and Periglacial Processes, 17*(4), 291-307, doi: 10.1002/ppp.567.

Park, S.-E., Bartsch, A., Sabel, D., Wagner, W., Naeimi, V., & Yamaguchi, Y. (2011). Monitoring freeze/thaw cycles using ENVISAT ASAR Global Mode. *Remote Sensing of Environment*, *115*(12), 3457-3467, doi: 10.1016/j.rse.2011.08.009.

Pienitz, R., Doran, P.T., & Lamoureux, S.F. (2008). Origin and geomorphology of lakes in the polar regions. In: Warwick F. Vincent and Johanna Laybourn-Parry. *Polar lakes and rivers: limnology of Arctic and Antarctic aquatic ecosystems*, Oxford University Press; 2008. p. 25-41, doi: 10.1093/acprof:oso/9780199213887.003.0002.

Pierdicca, N., Pulvirenti, L., Chini, M., Boni, G., Squicciarino, G., & Candela, L. (2014). Flood mapping by SAR: Possible approaches to mitigate errors due to ambiguous radar signatures. In *Geoscience and Remote Sensing Symposium (IGARSS), 2014 IEEE International* (pp. 3850-3853). IEEE, doi: 10.1109/IGARSS.2014.6947324.

Pivot, F.C. (2012). C-band SAR imagery for snow-cover monitoring at Treeline, Churchill, Manitoba, Canada. *Remote Sensing, 4*(7), 2133-2155, doi: 10.3390/rs4072133.

Ramsey III, E.W. (1995). Monitoring flooding in coastal wetlands by using radar imagery and ground-based measurements. *International Journal of Remote Sensing, 16*(13), 2495-2502, doi: 10.1080/01431169508954571.

Raup, B.H., Andreassen, L.M., Bolch, T., & Bevan, S. (2015) Remote sensing of glaciers, in *Remote Sensing of the Cryosphere* (ed. M. Tedesco), John Wiley & Sons, Ltd, Chichester, UK. doi: 10.1002/9781118368909.ch7

Regmi, P., Grosse, G., Jones, M.C., Jones, B.M., & Walter-Anthony, K. (2012). Characterizing post-drainage succession in thermokarst lake basins on the Seward Peninsula, Alaska with TerraSAR-X backscatter and Landsat-based NDVI data. *Remote Sensing, 4*(12), 3741-3765, doi: 10.3390/rs4123741.

Rignot, E.J., & van Zyl, J.J. (1993). Change detection techniques for ERS-1 SAR data. *Geoscience and Remote Sensing, IEEE Transactions on, 31*(4), 896-906, doi: 10.1109/36.239913.

Rignot, E. & Way, J.B. (1994). Monitoring freeze—thaw cycles along North—South Alaskan transects using ERS-1 SAR. *Remote Sensing of Environment*, *49*(2), 131-137, doi: 10.1016/0034-4257(94)90049-3.

Riordan, B., Verbyla, D., & McGuire, A.D. (2006). Shrinking ponds in subarctic Alaska based on 1950–2002 remotely sensed images. *Journal of Geophysical Research: Biogeosciences, 111*(G4), doi: 10.1029/2005JG000150.

Romanovsky, V.E., Drozdov, D.S., Oberman, N.G., Malkova, G.V., Kholodov, A.L., Marchenko, S.S., Moskalenko, N.G., Sergeev, D.O., Ukraintseva, N.G., Abramov, A.A., Gilichinsky, D.A., & Vasiliev, A.A. (2010). Thermal state of permafrost in Russia. *Permafrost and Periglacial Processes, 21*(2), 136-155, doi: 10.1002/ppp.683.

Rott, H., Nagler, T., & Scheiber, R. (2003). Snow mass retrieval by means of SAR interferometry. In *3rd FRINGE Workshop, European Space Agency, Earth Observation*.

Rott, H., Yueh, S. H., Cline, D. W., Duguay, C., Essery, R., Haas, C., Heliere, F., Kern, M., Macelloni, G., Malnes, E., Nagler, T., Pulliainen, J., Rebhan, H., & Thompson A. (2010). Cold regions hydrology high-resolution observatory for snow and cold land processes. *Proceedings of the IEEE, 98*(5), 752-765, doi: 10.1109/JPROC.2009.2038947.

Rouse, W.R., Oswald, C.J., Binyamin, J., Spence, C., Schertzer, W.M., Blanken, P.D., Bussières, N., & Duguay, C.R. (2005). Role of northern lakes in a regional energy balance. *Journal of Hydrometeorology, 6*(3), 291-305, doi: 10.1175/JHM421.1.

Rykhus, R.P. & Lu, Z. (2008). InSAR detects possible thaw settlement in the Alaskan Arctic Coastal Plain. *Canadian Journal of Remote Sensing*, *34*(1-2), 100-112, doi: 10.5589/m08-018.

Schirrmeister, L., Grosse, G., Schwamborn, G., Andreev, A.A., Meyer, H., Kunitsky, V.V., Kuznetsova, T.V., Dorozkina, M.V., Pavlova, E.Y., Bobrov, A.A., & Oezen, D. (2003). Late Quaternary history of the accumulation plain north of the Chekanovsky Ridge (Lena Delta, Russia): a multidisciplinary approach. *Polar Geography, 27*(4), 277-319.

Schwamborn, G., Rachold, V., & Grigoriev, M.N. (2002). Late Quaternary sedimentation history of the Lena Delta. *Quaternary International, 89*(1), 119-134, doi: 10.1016/S1040-6182(01)00084-2.

Shi, J., Hensley, S., & Dozier, J. (1997). Mapping snow cover with repeat pass synthetic aperture radar. In *Geoscience and Remote Sensing, IGARSS'97. Remote Sensing-A Scientific Vision for Sustainable Development*, IEEE International (Vol. 2), pp. 628-630, doi: 10.1109/IGARSS.1997.615205.

Shiklomanov, N., Streletskiy, D., Little, J., & Nelson, F. (2013). Isotropic thaw subsidence in undisturbed permafrost landscapes. *Geophysical Research Letters, 40*, 6356–6361.

Short, N., Brisco, B., Couture, N., Pollard, W., Murnaghan, K., & Budkewitsch, P. (2011). A comparison of TerraSAR-X, RADARSAT-2 and ALOS-PALSAR interferometry for monitoring permafrost environments, case study from Herschel Island, Canada. *Remote Sensing of Environment*, *115*(12), 3491-3506, doi:10.1016/j.rse.2011.08.012.

Short, N., Le Blanc, A.-M., Sladen, W., Oldenborger, G., Mathon-Dufour, V., & Brisco, B. (2014). RADARSAT-2 D-InSAR for ground displacement in permafrost terrain, validation from Iqaluit Airport, Baffin Island, Canada. *Remote Sensing of Environment, 141*, 40-51, doi: 10.1016/j.rse.2013.10.016.

Sobiech, J., Dierking, W., Bartsch, A., Boike, J., & Heim, B. (2011). Deviation of soil moisture in an arctic tundra landscape with SAR - suitability of different wavelengths and spatial resolutions. *Geophysical Research Abstracts, Vol. 13*, EGU2011-607-1, EGU General Assembly 2011, 04-08 April, Vienna, Austria.

Sobiech, J. (2012). Derivation of Environmental Parameters of Arctic Tundra Landscapes with SAR (Doctoral dissertation, Westfälische Wilhelms-Universität Münster).

Sobiech, J., Boike, J., & Dierking, W. (2012). Observation of melt onset in an arctic tundra landscape using high resolution TerraSAR-X and RADARSAT-2 data. In *Proceedings of. IGARSS, 2012, pp.*3552-3555.

Sobiech, J. & Dierking, W. (2013). Observing lake-and river-ice decay with SAR: advantages and limitations of the unsupervised k-means classification approach. *Annals of Glaciology, 54*(62), 65-72, doi: 10.3189/2013AoG62A037.

Sofronov, Yu. N. (2001). Pozvonochnye zhivotnye Ust-Lenskogo zapovednika: ryby, ptitsy, mlekopitayuschie (Vertebrates of Lena Delta Wildlife Reserve: fish, birds and mammals). *Flora i fauna zapovednikov (Flora and Fauna of Reserves), 94*, 1-44.

Schuur, E. A.G., McGuire, A.D., Schädel, C., Grosse, G., Harden, J.W., Hayes, D.J., Hugelius, G., Koven, C.D., Kuhry, P., Lawrence, D.M., Natali, S.M., Olefeldt, D., Romanovsky, V.E., Schaefer, K., Turetsky, M.R., Treat, C.C., & Vonk, J.E. (2015). Climate change and the permafrost carbon feedback. *Nature, 520*(7546), 171-179, doi: 10.1038/nature14338.

Streletskiy, D.A., Shiklomanov, N.I., Little, J.D., Nelson, F.E., Brown, J., Nyland, K.E., & Klene, A.E. (2016). Thaw subsidence in undisturbed tundra landscapes, Barrow, Alaska, 1962–2015. *Permafrost and Periglacial Processes*, doi: 10.1002/ppp.1918.

Strozzi, T., Wiesmann, A., & Mätzler, C. (1997). Active microwave signatures of snow covers at 5.3 and 35 GHz. *Radio Science*, *32*(2), 479-495, doi: 10.1029/96RS03777.

Strozzi, T., Wegmüller, U., & Mätzler, C. (1999). Mapping wet snowcovers with SAR interferometry. *International Journal of Remote Sensing, 20*(12), 2395-2403, doi: 10.1080/014311699212083.

Strozzi, T., Wegmuller, U., Werner, C., & Kos, A. (2012). TerraSAR-X interferometry for surface deformation monitoring on periglacial area. In *IEEE International Geoscience and Remote Sensing Symposium* (pp. 5214-5217).

Sturm, M. & Liston, G. E. (2003). The snow cover on lakes of the Arctic Coastal Plain of Alaska, USA. *Journal of Glaciology, 49*(166), 370-380.

Surdu, C.M., Duguay, C.R., Brown, L.C., & Fernández Prieto, D. (2014). Response of ice cover on shallow lakes of the North Slope of Alaska to contemporary climate conditions (1950–2011): radar remote-sensing and numerical modeling data analysis. *The Cryosphere, 8*(1), 167-180, doi: 10.5194/tc-8-167-2014.

Surdu, C.M., Duguay, C.R., Kheyrollah Pour, H., & Brown, L.C. (2015). Ice freeze-up and break-up detection of shallow lakes in Northern Alaska with spaceborne SAR. *Remote Sensing, 7*(5), 6133-6159, doi: 10.3390/rs70506133.

Svoray, T., Shoshany, M., Curran, P.J., Foody, G.M., & Perevolotsky, A. (2001). Relationship between green leaf biomass volumetric density and ERS-2 SAR backscatter of four vegetation formations in the semi-arid zone of Israel. *International Journal of Remote Sensing, 22*(8), 1601-1607, doi: 10.1080/01431160116869.

Townshend, J.R., Goff, T.E., & Tucker, C.J. (1985). Multitemporal dimensionality of images of normalized difference vegetation index at continental scales. *Geoscience and Remote Sensing, IEEE Transactions on*, (6), 888-895, doi: 10.1109/TGRS.1985.289474.

Ulaby, F.T., Cihlar, J., & Moore, R.K. (1974). Active microwave measurement of soil water content. *Remote sensing of Environment, 3*(3), 185-203, doi: 10.1016/0034-4257(74)90004-2.

Ulaby, F.T., Stiles, W.H., Dellwig, L.F., & Hanson, B.C. (1977). Experiments on the radar backscatter of snow. *Geoscience Electronics, IEEE Transactions on, 15*(4), 185-189, doi: 10.1109/TGE.1977.294490.

Ulaby, F.T., Batlivala, P.P., & Dobson, M.C. (1978). Microwave backscatter dependence on surface roughness, soil moisture, and soil texture: Part I-Bare soil. *Geoscience Electronics, IEEE Transactions on, 16*(4), 286-295, doi: 10.1109/TGE.1978.294586.

Ulaby, F.T., Bradley, G., & Dobson, M.C. (1979). Microwave backscatter dependence on surface roughness, soil moisture, and soil texture: Part II-vegetation-covered soil. *Geoscience Electronics, IEEE Transactions on, 17*(2), 33-40, doi: 10.1109/TGE.1978.294586.

Ulaby, F.T., Aslam, A., & Dobson, M.C. (1982). Effects of vegetation cover on the radar sensitivity to soil moisture. *Geoscience and Remote Sensing, IEEE Transactions on*, (4), 476-481, doi: 10.1109/TGRS.1982.350413.

Ullmann, T., Schmitt, A., Roth, A., Duffe, J., Dech, S., Hubberten, H.-W., & Baumhauer, R. (2014). Land Cover Characterization and Classification of Arctic Tundra Environments by Means of Polarized Synthetic Aperture X-and C-Band Radar (PolSAR) and Landsat 8 Multispectral Imagery—Richards Island, Canada. *Remote Sensing, 6*(9), 8565-8593, doi: 10.3390/rs6098565.

Vant, M.R., Gray, R.B., Ramseier, R.O., & Makios, V. (1974). Dielectric properties of fresh and sea ice at 10 and 35 GHz. *Journal of Applied Physics, 45*(11), 4712-4717.

Verhoest, N.E., Troch, P.A., Paniconi, C., & De Troch, F.P. (1998). Mapping basin scale variable source areas from multitemporal remotely sensed observations of soil moisture behavior. *Water Resources Research, 34*(12), 3235-3244, doi: 10.1029/98WR02046.

Wall, J., Collingwood, A., & Treitz, P. (2010). Monitoring surface moisture state in the Canadian High Arctic using synthetic aperture radar (SAR). *Canadian Journal of Remote Sensing, 36*(sup1), S124-S134, doi: 10.5589/m10-017.

Wang, Y., Wang, L., Li, H., Yang, Y., & Yang, T. (2015). Assessment of Snow Status Changes Using L-HH Temporal-Coherence Components at Mt. Dagu, China. *Remote Sensing, 7*(9), 11602-11620, doi: 10.3390/rs70911602.

Weber, H., Riffler, M., Nõges, T., & Wunderle, S. (2016). Lake ice phenology from AVHRR data for European lakes: An automated two-step extraction method. *Remote Sensing of Environment, 174*, 329-340, doi: 10.1016/j.rse.2015.12.014.

Weeks, W.F., Sellmann, P., & Campbell, W.J. (1977). Interesting features of radar imagery of ice-covered North Slope lakes. *Journal of Glaciology, 18*, 129-136.

Weeks, W.F., Fountain, A.G., Bryan, M.L., & Elachi, C. (1978). Differences in radar return from ice-covered North Slope Lakes. *Journal of Geophysical Research: Oceans, 83*(C8), 4069-4073.

Wegmüller, U. (1990). The effect of freezing and thawing on the microwave signatures of bare soil. *Remote Sensing of Environment*, *33*(2), 123-135, doi: 10.1016/0034-4257(90)90038-N.

Wegmüller U. & Werner C. L. (1996). Land applications using ERS-1/2 Tandem data. *FRINGE 96: ESA Workshop on Applications of ERS SAR Interferometry*.

Wegmüller, U. & Werner, C. (1997). Retrieval of vegetation parameters with SAR interferometry. *Geoscience and Remote Sensing, IEEE Transactions on, 35*(1), 18-24, doi: 10.1109/36.551930.

Werner, C., Wegmüller, U., Strozzi, T., & Wiesmann, A. (2000). Gamma SAR and interferometric processing software. In *Proc. ERS-Envisat Symposium,* Gothenburg, Sweden.

Wetterich, S., Kuzmina, S., Andreev, A.A., Kienast, F., Meyer, H., Schirrmeister, L., Kuznetsova, T., & Sierralta, M. (2008). Palaeoenvironmental dynamics inferred from late Quaternary permafrost deposits on Kurungnakh Island, Lena Delta, northeast Siberia, Russia. *Quaternary Science Reviews, 27*(15), 1523-1540.

Westermann, S., Duguay, C.R., Grosse, G., & Kääb, A. (2015a). Remote sensing of permafrost and frozen ground. In *Remote Sensing of the Cryosphere*, (ed. M. Tedesco), John Wiley & Sons, Ltd, Chichester, UK, 307-344, doi: 10.1002/9781118368909.ch13.

Westermann, S., Østby, T., Gisnås, K., Schuler, T.V., & Etzelmüller, B. (2015b). A ground temperature map of the North Atlantic permafrost region based on remote sensing and reanalysis data. *The Cryosphere, 9*, 1303-1319, doi: 10.5194/tc-9-1303-2015.

Weydahl, D.J. (2001a). Analysis of ERS tandem SAR coherence from glaciers, valleys, and fjord ice on Svalbard. *Geoscience and Remote Sensing, IEEE Transactions on*, *39*(9), 2029-2039, doi: 10.1109/36.951093.

Weydahl, D.J. (2001b). Analysis of ERS SAR coherence images acquired over vegetated areas and urban features. *International Journal of Remote Sensing, 22*(14), 2811-2830, doi: 10.1080/01431160010006412.

Wickramanayake, A., Henschel, M.D., Hobbs, S., Buehler, S.A., Ekman, J., & Lehrbass, B. (2016). Seasonal variation of coherence in SAR interferograms in Kiruna, Northern Sweden.

International Journal of Remote Sensing, 37(2), 370-387, doi: 10.1080/01431161.2014.915435.

WMO (2010). GCOS: Global Climate Observing System, http://gcos.wmo.int.

Woodhouse, I. H. (2005). Introduction to microwave remote sensing. CRC press.

Xie, C., Shao, Y., Xu, J., Wan, Z., & Fang, L. (2013). Analysis of ALOS PALSAR InSAR data for mapping water level changes in Yellow River Delta wetlands. *International journal of remote sensing, 34*(6), 2047-2056, doi: 10.1080/01431161.2012.731541.

Zebker, H. & Villasenor, J. (1992). Decorrelation in interferometric radar echoes. *Geoscience and Remote Sensing, IEEE Transactions on, 30*(5), 950-959, doi: 10.1109/36.175330.

Zhang, T., Barry, R.G., Knowles, K., Heginbottom, J.A., & Brown, J. (1999). Statistics and characteristics of permafrost and ground-ice distribution in the Northern Hemisphere. *Polar Geography, Polar Geography, 23*(2), pp. 132-154, doi: 10.1080/10889370802175895.

Zhang, T., Heginbottom, J.A., Barry, R.G., & Brown, J. (2000). Further statistics on the distribution of permafrost and ground ice in the Northern Hemisphere, *Polar Geography, 24*, 126-131, doi: 10.1080/10889370009377692.

Zhang, T., Zeng, Q., Li, Y., & Xiang, Y. (2008). Study on relation between InSAR coherence and soil moisture. In *Proceedings of the ISPRS Congress* (Vol. 37, pp. 131-134).

Zimov, S.A., Voropaev, Y.V., Semiletov, I.P., Davidov, S.P., Prosiannikov, S.F., Chapin, F.S., Trumbore, S., & Tyler, S. (1997). North Siberian lakes: a methane source fueled by Pleistocene carbon. *Science, 277*(5327), 800-802, doi: 10.1126/science.277.5327.800.

Zimov, S.A., Schuur, E.A., & Chapin III, F.S. (2006). Permafrost and the global carbon budget. *Science, 312*(5780), 1612-1613, doi: 10.1126/science.1128908.

Zubrzycki, S., Kutzbach, L., Grosse, G., Desyatkin, A., & Pfeiffer, E.M. (2013). Organic carbon and total nitrogen stocks in soils of the Lena River Delta. *Biogeosciences, 10*(6), 3507-3524, doi: 10.5194/bg-10-3507-2013.

Acknowledgements

First and foremost, I would like to thank my supervisor, Julia Boike, for all the confidence she placed in me from the moment she decided to give me this PhD position to this very moment writing my acknowledgements. I thank her for all her support and readiness to help. My second supervisor, Birgit Heim, always supported and protected me and my work at all the official levels. Her incredibly broad knowledge concerning up-to-date state of the art remote sensing, as well as all formal and informal related information is impressive and very helpful. I also thank Moritz Langer and Sina Muster for the valuable suggestions and proofreading during my work. Moritz tried his best to explain to me what it is to be a scientist and I hope I learned something. Many thanks also go out to the SPARC group for the pleasant working atmosphere (especially Stephan Lange), fun days and dinners together.

I had an opportunity to spend a few weeks each year at the University of Oslo, where I was lucky to work with Andreas Kääb. I have never met such a smart and professional, but at the same time relaxing and kind person. Without him, this thesis simply could not be done. I also extend my gratitude to the entire Cryosphere working group of the University of Oslo for all the discussions, as well as Chris D'Amboise for the couch and all the fun.

It was Julia who encouraged me to apply for a scholarship to be granted a temporary research position at the University of Waterloo, Canada. All the credit for this important part of my PhD go first to her and I thank the DAAD (German Academic Exchange Service) for the scholarship. I also thank the working group at the University of Waterloo and especially the group leader, Claude Duguay for my second paper, shared knowledge and all the nights out and the farewell at Claude's house. I extend a special thank you to the inspiring Homa, with whom I shared many moments of pure joy. I was also lucky enough to get to know the unique family of the Overduins, including Margaret, Jan and Simon, who made my stay in a foreign

country a thousand miles away from home as comfortable and as pleasant as possible.

The challenge of InSAR, the most difficult part of my work, was shared with Henriette Sudhaus. I am so grateful for her deep interest in the topic, as well as all the urgent and routine help she provided with a high degree of competence.

My three field seasons in the Lena River Delta were incredible experiences. I thank my beloved Bornemann family, including Anne, Antje, Niko, Samuel and Sascha for the best and unrepeatable July of 2013. I especially thank Niko, who always knew how to manage every situation in the field and save the world and Anne, who never stopped convincing me that I am worth something.

I thank Waldemar Schneider, as well as all the people in Tiksi and the Lena Delta Reserve. The invaluable help they provide actually makes it possible for us to enjoy our expeditions. I also thank Fyodor Sellyakhov, leader of the Samoylov Station, and his team for all the effort to host and support us.

I thank Michael Angelopoulos for the careful and devoted proofreading at the last moment. Boris Radosavljevic also provided immense support with English and Adobe Illustrator before all important conferences and paper submissions.

My PhD work was financed by the Helmholtz Alliance “Remote Sensing and Earth System Dynamics” and I am very grateful! I also acknowledge the graduate school POLMAR for a conference travel grant, useful courses, and PhD days.

At last, I want to say that AWI is a truly unique place where I have really enjoyed working all these years and where I was lucky to meet so many wonderful and interesting people. I am sincerely grateful for this!

Eidesstattliche Versicherung gemäß § 8 der Promotionsordnung der Naturwissenschaftlich-Mathematischen Gesamtfakultät der Universität Heidelberg

1. Bei der eingereichten Dissertation zu dem Thema „Exploring the potential of high temporal resolution X-band SAR time series for various permafrost applications with ground truth observations in the Lena River Delta, Siberia“ handelt es sich um meine eigenständig erbrachte Leistung.

2. Ich habe nur die angegebenen Quellen und Hilfsmittel benutzt und mich keiner unzulässigen Hilfe Dritter bedient. Insbesondere habe ich wörtlich oder sinngemäß aus anderen Werken übernommene Inhalte als solche kenntlich gemacht.

3. Die Arbeit oder Teile davon habe ich bislang nicht an einer Hochschule des In- oder Auslands als Bestandteil einer Prüfungs- oder Qualifikationsleistung vorgelegt.

4. Die Richtigkeit der vorstehenden Erklärungen bestätige ich.

5. Die Bedeutung der eidesstattlichen Versicherung und die strafrechtlichen Folgen einer unrichtigen oder unvollständigen eidesstattlichen Versicherung sind mir bekannt. Ich versichere an Eides statt, dass ich nach bestem Wissen die reine Wahrheit erklärt und nichts verschwiegen habe.

_____ _____

Ort und Datum Unterschrift